Università degli Studi di Ferrara

DOCTORAL COURSE IN PHYSICS

CYCLE XXXIV

DIRECTOR Prof. Eleonora Luppi

Innovative design and optimization of plasma chamber for ECR ion sources

---

Scientific/Disciplinary Sector (SDS) FIS/04

Candidate:

Dott. Gallo Carmelo Sebastiano

Supervisors:

Dott. Galatà Alessio

Prof. Bettoni Diego

Years 2019 – 2021

Contents

Introduction

Electron Cyclotron Resonance Ion Sources (ECRIS) [1] are the most effective devices to produce high intensity beams of medium-high charge states for both applied and fundamental research. In such sources, a plasma is magnetically confined inside a vacuum chamber (the plasma chamber) by an axial magnetic field (generated by two or more coils) and a radial one (generated by a multiple, usually a hexapole). Figure 1 shows an example of the magnetic field of an ECRIS: on the left the axial and on the right the radial magnetic field. The superposition of these two fields, called the "B-minimum" structure, generates a magnetic structure whose intensity increases going from the centre of the plasma chamber to the periphery: it impresses to the plasma the typical "star-shaped" shape.

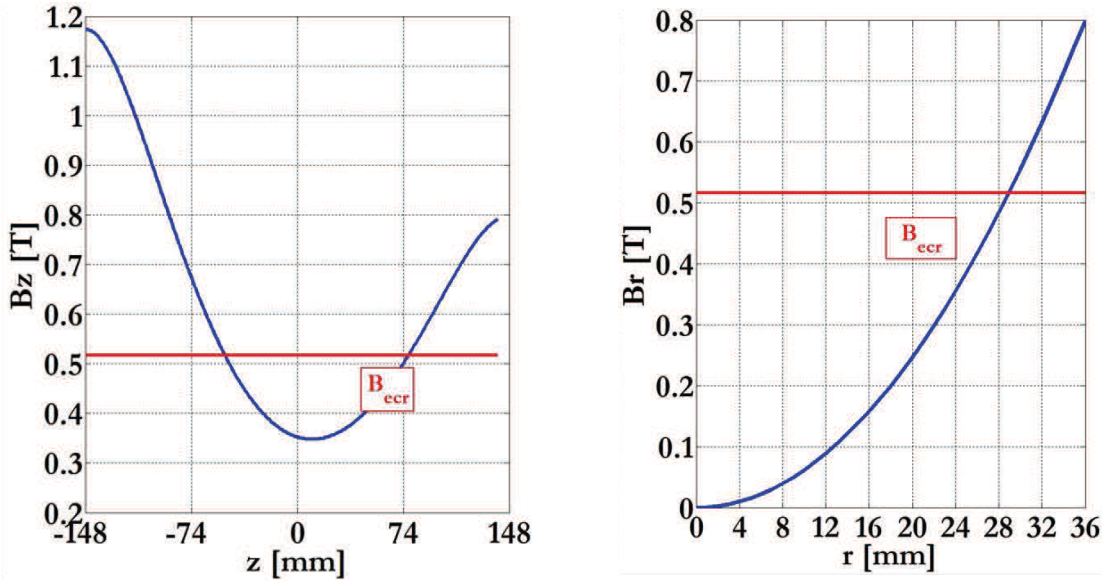

Figure 1: Typical magnetic field profile of an ECRIS: on the left the axial field generated by the coils; on the right the radial one generated by the hexapole.

The mechanism creating and sustaining the plasma is a resonant interaction (the Electron Cyclotron Resonance, ECR) between electromagnetic waves injected into the plasma chamber (working as a resonant cavity) and the electrons' Larmor motion under the influence of the magnetic field: in those points where the microwave frequency equals the Larmor frequency the energy is transferred to plasma electrons that, in turn, can create medium-high charge states through ionizing collisions. Considering the particular topology of the magnetic field, the ECR resonance takes place at specific points, forming an egg-shaped surface called resonance surface. The output of an ECR source, in terms of intensity and charge states produced, strongly depends on the optimization of the energy transfer to plasma electrons. Many techniques have been developed so far to improve the performances of an ECRIS: first of all the use of higher and higher frequencies and magnetic fields, which often implies the development of expensive and technologically complex devices. Another possibility is the optimization of the electromagnetic field inside the plasma chamber, by injecting two close or well-separated frequencies (respectively Two Frequency Heating [2] [3] [4] and Two Close Frequency Heating [5]) [6], as well as the fine-tuning of a single frequency, known as frequency tuning effect [7] [8] [9]. The main aim of those techniques is to increase the electrons

density and energy by optimizing the power absorption by the microwave field following Geller's scaling laws [1] and the ECRIS standard model [10]. This thesis presents an alternative approach to the optimization of the electromagnetic field, consisting of the modification of the plasma chamber geometry and the microwave injection, to produce an intense field in those points where the ECR resonance takes place. The thesis will propose a new geometry, called IRIS (Innovative Resonators for Ion Sources), based and the shape impressed to the plasma by the magnetic field and developed in two versions, IRIS-OLD and IRIS-NEW. The geometry has been characterized electromagnetically using CST Microwave Studios, COMSOL Multiphysics and MatLab to implement the 3D dielectric tensor of the plasma. The physic case used to validate the eventual improvements brought by the new design is the ECR source CAESAR, installed at INFN-LNS [11] [12]: it is a second-generation ECRIS, working at 14.5 GHz and with a plasma chamber of cylindrical shape. The validation will pass through the comparison of the coupling of the electromagnetic field from the injection line to the plasma chamber, the distribution of the electromagnetic field set-up inside the plasma and the power absorbed by the plasma. Finally, an unconventional launching scheme, as an alternative to the classical rectangular waveguide, will be proposed.
This thesis starts with a first general chapter describing briefly its scientific framework. The second chapter is dedicated to the description of ECR ion sources: it starts with a short historical review, followed by some basic plasma definitions. The processes responsible for ions creation and destruction will then be treated, together with the description of diffusion's mechanisms typical of ECR ion sources. Finally, all the physical mechanisms involved in the plasma confinement will be described, ending with an explanation of the techniques used to improve the performances. The third chapter will describe the electromagnetic theory involved in the operation of ECR sources: it will explain the theoretical basis of resonant modes inside the waveguides and in the cylindrical resonant cavities. The fourth chapter describes the core of this thesis: it is dedicated to the simulations of the CAESAR plasma chamber and its comparison with the proposed unconventional geometry. We will see the evolution of the design from the first version to the final one and the effect of an innovative microwave launching system based on slotted antennas. The thesis is closed by conclusions and future perspectives.

Chapter 1

Scientific Framework

The work presented in this thesis has been carried out in the framework of two INFN projects, that involve specific applications of ECR sources and could take benefit from the improvements resulting from this study and described in chapter 4: the PANDORA [13] and SPES Projects [14]. For the sake of completeness, a brief description of both will be given in this chapter.

1.1 PANDORA

PANDORA (Plasmas for Astrophysics, Nuclear Decays Observation and Radiation for Archaeometry) [13] is an INFN project financed by the III National Scientific Committee involving the construction of an innovative plasma trap based on the ECR principle, to carry out fundamental studies in nuclear astrophysics, astrophysics and plasma physics. The aim is to measure the decay rate, as a function of the ionization state, for β radionuclides (like ^{176}Lu) involved in several astrophysical processes and cosmology. Radioactive species will be injected in a plasma produced inside a magnetic trap (reproducing stellar-like conditions in terms of ionization stages), where they will be ionized by energetic electrons (see figure 1.1). PANDORA will be equipped with a multi diagnostic setup able to measure not

only gamma rays following the β decay, but also the plasma self-emission and in turn to deduce its characteristics like density distribution, temperature and charge states produced.

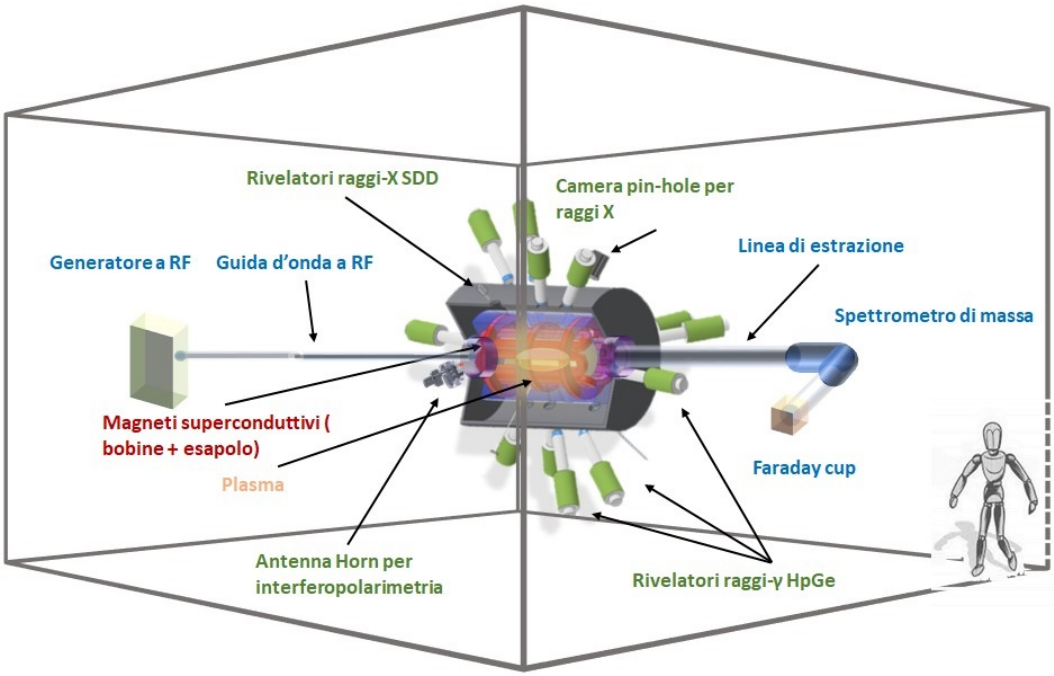

Figure 1.1: The magnetic trap of PANDORA with the diagnostic system consisting of an array of 14 HPGe detectors and a non-invasive multi-diagnostic apparatus.

The scientific context of the project is the study of the production of unstable nuclei by nuclear fusion in massive stars. The nucleosynthesis proceeds by nuclear fusion in massive stars until iron, where it stops because the fusion of heavier nuclei needs energy instead of providing it. Heavier nuclei are the result of the interplay between neutron capture and beta decay, which represent the driving mechanisms allowing to increase nuclear mass and charge up to the limits imposed by nuclear stability [15]. This interplay determines the pathways of stellar nucleosynthesis and, thus, the abundances of atomic nuclei observed in the Universe. However, a major difference exists between terrestrial and stellar conditions: stellar nucleosynthesis proceeds in a hot and dense environment which affects the degree of ionization of the atoms involved in the stellar nucleosynthesis. This raises the question of whether or not the high degree of ionization could

induce any significant differences in the beta-decay properties concerning neutral atoms. Experimental results using highly ionized atoms showed strong variations of their half-life. Bare $^{187}Re^{75+}$ ions decay, due to the bound-state beta decay, by 9 orders of magnitude faster than neutral ^{187}Re atoms with a half-life of 42 Gyr [16]. Bare $^{163}Dy^{66+}$ nuclei, being stable as neutral atoms, become radioactive, thus allowing the s-process, with a half-life of 33 days [17]. The main aim of the PANDORA project is to develop a new and complementary approach to measure, for the first time, nuclear β-decay rates in a plasma simulating stellar-like conditions. The study will be mainly focused on radionuclides involved in nuclear-astrophysics processes. Compact magnetic plasma traps, where plasmas reach electron density values $n_e \sim 10^{11} cm^{-3} - 10^{13} cm^{-3}$ and a wide range of temperatures $kT_e \sim 0.1keV - 30keV$, are suitable for such studies. The main advantage of a plasma trap is that by fine-tuning the electron temperature it is possible to establish an ion charge state distribution that can mimic a specific stellar environment. Plasma parameters can be inferred using dedicated diagnostic tools and the nuclear decay rates can be evaluated as a function of the charge state distribution of in-plasma ions. This new approach will open up the possibility to investigate tens of physics cases, among the others, ^{204}Tl, ^{63}Ni, ^{60}Co, ^{171}Tm, ^{147}Pm, ^{85}Kr, ^{176}Lu and the pairs $^{187}Re - ^{187}Os$ and $^{87}Sr - ^{87}Rb$, which play a crucial role in establishing the time scale of cosmological processes (cosmo-clocks). The project is presently in the design phase and the first experiments on ^{176}Lu are expected in 2025.

1.2 SPES

The SPES (Selective Production of Exotic Species) project [18] is currently under construction at Legnaro National Laboratories of INFN: it aims at developing a facility for exotic beams production. The key feature of SPES will be to provide high intensity and high-quality beams of neutron-rich nuclei to perform forefront research in nuclear structure, reaction dynamics and interdisciplinary fields like medical, biological and material sciences. The exotic isotopes, produced in the so-called Target Ion Source System [19] [20], will be accelerated by a newly designed RFQ [21] coupled to the ALPI Superconducting Linac [22], reaching energies of 11 MeV/amu for masses in the region of $A \sim 130$. Before the injection in the LNL

accelerators complex, it is necessary to increase the charge state of the radioactive species from 1+ to n+, thus allowing its post-acceleration: this task is accomplished using an ECR-based Charge Breeder [23] [24] [25] [26] (see figure 1.2). In particular, it is an updated version of the Phoenix [27] booster, in operation at Laboratoire de Physique Subatomique et de Cosmologie (LPSC) in Grenoble.

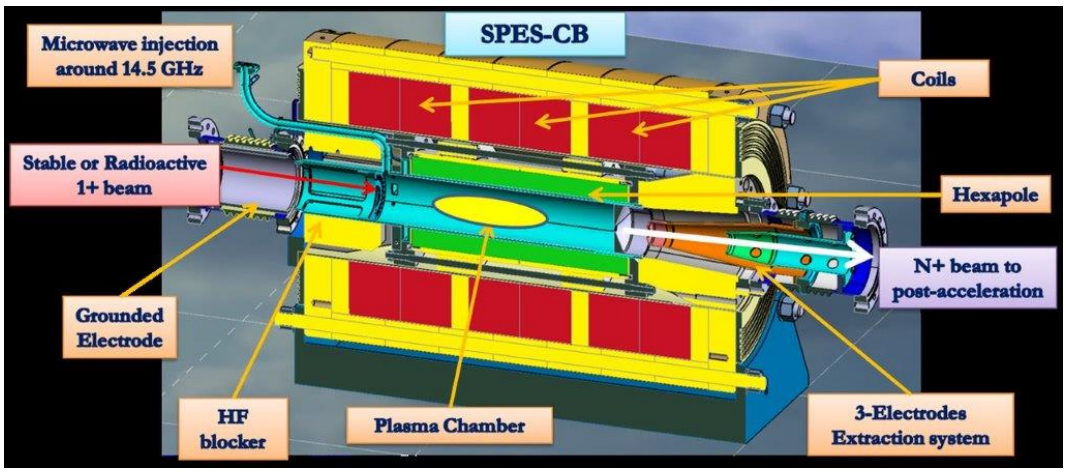

Figure 1.2: Sketch of the SPES Charge Breeder.

The SPES project is divided into four phases:

- α: installation and commissioning of a cyclotron B70, by the BEST Theratronics company [28] [29], capable of accelerating proton beams up to 70 MeV and with high intensity (expected currents up to $750\mu A$);
- β: creation of an infrastructure for research in nuclear physics using post-accelerated radioactive beams. It will apply the ISOL type production system, consisting of the interaction of an intense proton beam with different targets capable of sustaining up to about 10 kW of power. Among the different targets, the one of greatest interest is uranium carbide, with which they can be obtained $10^{13} fissions/s$ [30];
- γ: taking advantage of the peculiarities of the SPES facility, two possible production processes have been developed that are part of the LARAMED [31] [32] and ISOLPHARM projects [33] [34]. They have the purpose of producing radionuclides of interest for diagnostics and therapy (e.g. ^{99}Tc, $^{64,67}Cu$, ^{47}Sc, $^{51,52}Mn$, ^{89}Zr, etc.);

- δ: the SPES cyclotron will also be used to produce intense neutron beams generated by reactions between the proton beam and beryllium, lithium and tungsten targets. The aim will be the study of the effects of neutrons in many fields, from electronics to space missions, passing through fourth-generation nuclear reactors and treatments of radioactive wastes, without neglecting fundamental physics and the study of materials.

Chapter 2

The Physics of ECR Ion Sources

The previous chapter identified the scientific framework of the work described in this thesis. To help in the interpretation and evaluation of the results obtained, this chapter is dedicated to the description of the physical processes involved in the functioning of an ECR source. It will start with a brief introduction, followed by a description of the various mechanisms for plasma generation, sustenance and confinement. Considering the object of this thesis, special attention will be dedicated to the electromagnetic behaviour of the plasma. The chapter will end with a description of the various techniques used to improve the performances.

2.1 Introduction

The Electron Cyclotron Resonance Ion Sources (ECRIS) [1] are the most common devices to deliver stable multiply charged ion beams to particle accelerators. In such sources, a plasma is created inside a vacuum chamber (the plasma chamber) immersed in a particular multi-Tesla magnetic configuration called "B-minimum" structure, created by superimposing the field generated by two or more coils to the one generated by a hexapole. The mechanism responsible for the generation and maintenance of the plasma is a resonant interaction, the Electron Cyclotron

Resonance, between microwaves (typically between 14 GHz and 18 GHz) and the electrons' motion in the external magnetic field: the condition for it to take place is that the microwave frequency ν be equal to the electrons' Larmor frequency $\nu_e = \frac{qB}{2\pi m_e}$. Given the particular magnetic configuration, this condition is usually satisfied on closed egg-shaped surfaces called resonance surfaces: this process creates high energy electrons that can, in turn, produce multiply charged ions through ionizing collisions. The B-minimum structure acts as a magnetic trap, thus ensuring a sufficiently high confinement time for ions and electrons to reach high charge states. The development of ECRIS during the last forty years has been driven by the improvement of the B-minimum magnetic trap, according to the High B mode concept proposed in 1990 [10]. In particular, the need to achieve higher currents of highly charged ions pushed the development of ECRIS towards the use of higher power and higher microwave frequency generators that require higher confining magnetic field, according to Geller's scaling laws [1]. Classification in terms of ECRIS' generation is commonly accepted according to the typical operational frequency: the very first sources operated usually below 10 GHz and were characterized by very high power consumption and a poor vacuum, leading to a low average extracted charge. The second-generation ECRIS, still nowadays used, are operated at 14 GHz - 18 GHz in high vacuum condition, reaching charge states between 8 and 14 for Ar. An example is the source CAESAR object of the study of this thesis, into operation at INFN-LNS since the '90s [12]. The third generation ECRIS works at a frequency of 28 GHz or higher, giving for example charge states between 14 and 18 for Ar: sources of this kind operate in several international laboratories like LBNL [35].

Before going to the description of the main physical processes involved with ECR sources' operation, it is useful to recall some basic definitions in common with any kind of plasma. A plasma, a *quasi-neutral* ionized gas at high temperatures, is considered one of the four states of matter. It exists in a natural state in stars' nuclei and represents most of the visible matter in the universe. On Earth, plasmas are artificially generated for several applications, such as particle accelerators, thermonuclear fusion, material processing and manufacturing, medical and environmental applications, and many others. Contrary to a neutral gas, a plasma contains also charged particles that interact with each other through collisions.

In most types of plasma, quasi-neutrality is not just an ideal equilibrium state,

but it is a state that the plasma actively tries to achieve and maintain by readjusting the local charge distribution in response to a disturbance. It is possible to define a characteristic length-scale, known as the **Debye length** [36] λ_D, defined as the distance after which a plasma can screen itself from external electrostatic disturbance:

$$\lambda_D = \left(\frac{\epsilon_0 k T_e}{e^2 n_e}\right)^{\frac{1}{2}} \left(\frac{n_e}{cm^{-3}}\right)^{-\frac{1}{2}} cm. \tag{2.1}$$

The Debye length is a fundamental property of nearly all plasmas, and depends equally on the plasma's temperature and density. An *ideal* plasma has many particles per Debye sphere, i.e.

$$N_D \equiv n_e \frac{4\pi}{3} \lambda_D^3 \gg 1, \tag{2.2}$$

Besides the screening distance described above, it is interesting to see how a plasma responds to an external disturbance. If we suppose that, at a given moment, an external force acts separating electrons from positive ions, it is possible to demonstrate that the former start oscillating around the fixed positive charge density, to restore quasi-neutrality. This oscillation takes place at a specific frequency, know as **plasma frequency** [37], defined as:

$$\omega_p \equiv \left(\frac{e^2 n_e}{\epsilon_0 m_e}\right)^{\frac{1}{2}} \simeq 5.6 \times 10^4 \left(\frac{n_e}{(cm)^{-3}}\right)^{\frac{1}{2}} s^{-1} \tag{2.3}$$

The plasma frequency depends only on the electron density and is usually very high due to the small value of the electron mass: to a density $n_e = 10^{18}\, m^{-3}$ corresponds, in fact, a plasma frequency of $\nu_e = 9\, GHz$

2.2 Magnetic confinement

In ECR ion sources plasma particles are generated and confined in a magnetic field, so it is important to describe the motion of a single charged particle under the influence of electric and magnetic forces [38]. Generally, the equation of motion of a particle of mass m and charge q moving in a region where a magnetic field $\mathbf{B}$,

an electric field $\mathbf{E}$ and a generic force $\mathbf{F}$ are present can be written:

$$m\frac{d\mathbf{v}}{dt} = q\left(\mathbf{v}\times\mathbf{B}+\mathbf{E}\right)+\mathbf{F} \tag{2.4}$$

It can be demonstrated that under particular conditions of magnetic field geometry and applied external forces, the general solution of this equation, represented by the vector position $\mathbf{r}(t)$, assumes a periodic characteristic. The main types of periodicity that can happen are:

- **Cyclotron motion**: the particle will rotate in a plane perpendicular to the magnetic field.
- **Mirror reflection**: the particle will move back and forth along a magnetic field line.
- **Drift motion**: the particle will move on a closed surface described by some magnetic field lines.

The first motion is the one with the highest frequency; the second is orders of magnitude slower. Each magnetic configuration where this last motion happens is said "magnetic trap" and, as we will see later in this chapter, the process is termed "magnetic trapping". The drift motion is in turns orders of magnitude slower than the reflection. In analyzing the cyclotron motion the guiding centre approximation can be used, where the guiding centre is the centre of the circle described by the particle motion: its radius is called Larmor radius $\mathbf{r}_c$, while the period of the motion is called cyclotron period τ_c. The instantaneous velocity of the guiding centre is defined as the velocity of the Guiding Centre System (GCS): the particle position can then be expressed through the vector position $\mathbf{R}_c$ of the guiding centre, the Larmor radius vector $\mathbf{r}_c$ and a phase ϕ. The instantaneous velocity $\mathbf{V}_G$ of the GCS can be decomposed concerning the magnetic field direction as:

$$\mathbf{V}_G = \mathbf{V}_\parallel + \mathbf{V}_\perp \tag{2.5}$$

The first component coincides with the particle velocity along the magnetic field

$$\mathbf{V}_\parallel = \mathbf{v}_\parallel \tag{2.6}$$

while the second differs from the orthogonal one $\mathbf{v}_\perp$. The component $\mathbf{V}_\perp$ is usually termed "drift velocity" $\mathbf{V}_D$ because represents the motion of the guiding centre across the magnetic field lines. After this general description, the particle motion under specific external forces and different magnetic field geometry will be discussed [39].

2.2.1 Uniform E and B fields

Let's consider initially a uniform magnetic field and no other forces applied ($\mathbf{E} = \mathbf{F} = 0$). A charged particle has, in this case, a simple cyclotron motion and equation 2.4 become:

$$m\frac{d\mathbf{v}}{dt} = q\mathbf{v} \times \mathbf{B} \tag{2.7}$$

Supposing the magnetic field $\mathbf{B}$ to be in z direction ($\mathbf{B} = B\hat{\mathbf{z}}$) we obtain the equations:

$$\begin{aligned} m\dot{v}_x = qBv_y \qquad m\dot{v}_y = -qBv_x \qquad m\dot{v}_z = 0 \\ \ddot{v}_x = \frac{qB}{m}\dot{v}_y = -\left(\frac{qB}{m}^2\right)v_x \\ \ddot{v}_y = \frac{qB}{m}\dot{v}_x = -\left(\frac{qB}{m}^2\right)v_y \end{aligned} \tag{2.8}$$

that describe a simple harmonic oscillator at the cyclotron frequency:

$$\omega_c \equiv \frac{|q|B}{m} \tag{2.9}$$

The solution to equation 2.8 is a circular motion about guiding center in a plane perpendicular to the magnetic field. The radius of this gyromotion, that is the Larmor radius r_c, is given by the relation:

$$r_c \equiv \frac{v_\perp}{\omega_c} = \frac{mv_\perp}{|q|B} \tag{2.10}$$

being $v_\perp$ the component of the particle's velocity perpendicular to the magnetic field. Two handy formulas allow a fast calculation of this parameter for ions with

mass number A and charge q and for electrons [39]:

$$\begin{aligned} r_c^+ &\approx 1.5 * 10^{-4} \frac{\sqrt{W_\perp A}}{qB} \qquad [\text{m}] \\ r_c^- &\approx 3.8 * 10^{-6} \frac{\sqrt{W_\perp}}{B} \qquad [\text{m}] \end{aligned} \tag{2.11}$$

being $W_\perp\,[eV]$ the energy corresponding to the motion perpendicular to B [T]. The direction of gyration is always such that the magnetic field generated by the charged particle is opposite to the externally imposed field. Plasma particles, therefore, tend to reduce the magnetic field and so plasmas can be classified as diamagnetic.

Let's now add to the magnetic field an electric field $\mathbf{E}$ and suppose that the electric field lies in the $x - z$ plane so that $E_y = 0$. Equation 2.4 becomes:

$$m\frac{d\mathbf{v}}{dt} = q\left(\mathbf{E} + \mathbf{v} \times \mathbf{B}\right) \tag{2.12}$$

The z component of this equation will lead to the normal acceleration of the charged particle under the component E_z of the electric field along a magnetic field line. The other two components will lead to the usual gyromotion with angular frequency ω_c about the magnetic field line and, superimposed, a drift motion of the guiding centre with a velocity $\mathbf{v}_{gc}$ (in the negative y direction for $E_x > 0$, see figure 2.1) given by:

$$\mathbf{v}_{gc} = \frac{\mathbf{E} \times \mathbf{B}}{B^2} \equiv \mathbf{v}_E \tag{2.13}$$

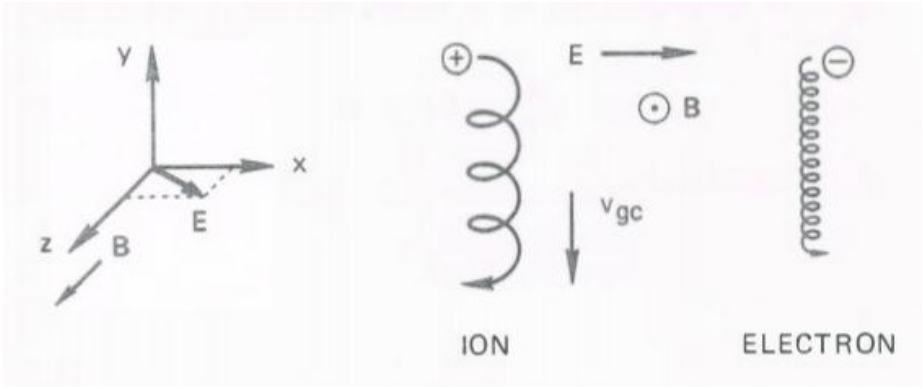

Figure 2.1: Particle drifts in crossed **E** and **B** fields

As we see from the above formula, this drift is perpendicular to both electric and magnetic fields and is independent of q, m, and $v_\perp$. The formula can be generalized to a generic force **F** by replacing **E** with $\mathbf{F}/q$ in the equation of motion. In the case of the gravitational force $\mathbf{F} = m\mathbf{g}$, we obtain the drift velocity:

$$\mathbf{v}_g = \frac{m}{q}\frac{\mathbf{g} \times \mathbf{B}}{B^2} \tag{2.14}$$

It can be noted that in this case ions and electrons drift in opposite directions, so the motion leads to a net current density in the plasma given by:

$$\mathbf{j} = n\,(M_i + m)\,\frac{\mathbf{g} \times \mathbf{B}}{B^2} \tag{2.15}$$

Anyway, the magnitude of this drift is usually negligible [39].

2.2.2 Non uniform B

Now that the motion under a uniform magnetic field and external forces were clarified, we can now skip to the more realistic case of a non-uniform magnetic field. Two important cases will be described in the following:

- **GradB Drift.**
  Consider now only a magnetic field in $\hat{\mathbf{z}}$ direction that increases in intensity in $\hat{\mathbf{y}}$ direction: the gradient in $|B|$ causes the Larmor radius to be larger at the bottom of the orbit than at the top. This leads to drifts, in opposite

direction for ions and electrons, perpendicular to both **B** and gradB. This is shown in figure 2.2.

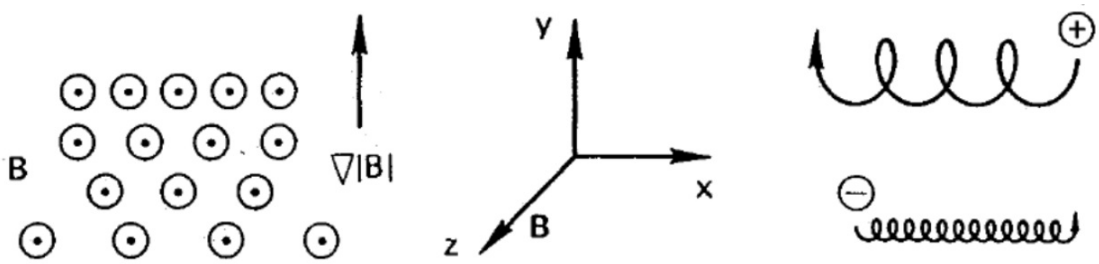

Figure 2.2: Drift of a gyrating particle in a non uniform magnetic field

By supposing that the scale of inhomogeneity of the magnetic field is big compared to the Larmor radius r_c ($|\nabla B/B| \ll 1/r_c$), if we average the Lorentz force $\mathbf{F} = q\mathbf{v} \times \mathbf{B}$ over a gyration we obtain that the average of F_x is zero since the particle spends as much time moving up as down. The average of F_y can be obtained by a Taylor expansion of the field **B** about the point $x_0 = y_0 = 0$:

$$\begin{aligned} \mathbf{B} &= \mathbf{B}_0 + (\mathbf{r} \cdot \boldsymbol{\nabla}) + \dots \\ B_z &= B_0 + y\,(\partial B/\partial y) + \dots \end{aligned} \tag{2.16}$$

The average of F_y then becomes:

$$\bar{F}_y = \mp q v_\perp r_c \frac{1}{2}\left(\frac{\partial B}{\partial y}\right) \tag{2.17}$$

and the guiding centre drift velocity is, generalizing the result:

$$\mathbf{v}_{\boldsymbol{\nabla} B} = \pm \frac{1}{2} v_\perp r_c \frac{\mathbf{B} \times \boldsymbol{\nabla} B}{B^2} \tag{2.18}$$

Note that the sign stands for the sign of the charge so this kind of drift causes a current transverse to B.

- **Curvature Drift**.
  Let us consider a magnetic field with the line of force curved with constant

radius $\mathbf{R}_c$ and take $|B|$ to be constant (figure 2.3). Such a filed does not obey Maxwell's equations in vacuum so in practice the gradB drift will always be added to the effect derived here.

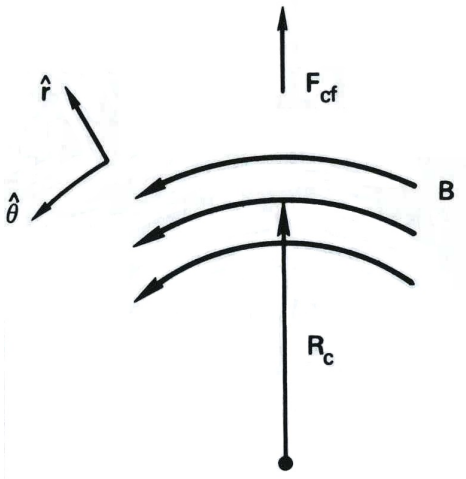

Figure 2.3: A curved magnetic field

A guiding centre drift arises from the centrifugal force felt by the particles as they move along the field lines. If we denote with $v_\parallel^2$ the average square of the component of the random velocity along $\mathbf{B}$ the average centrifugal force is:

$$\mathbf{F}_{cf} = \frac{m v_\parallel^2}{\mathbf{R}_c}\hat{\mathbf{r}} \tag{2.19}$$

This gives rise to a drift, called curvature drift, given by the equation:

$$\mathbf{v}_R = \frac{1}{q}\frac{\mathbf{F}_{cf} \times \mathbf{B}}{R_c} \tag{2.20}$$

We must now compute the gradB drift that accompanies this last one when the decrease of $|B|$ with radius is taken into account. In vacuum we have $\boldsymbol{\nabla} \times \mathbf{B} = 0$: in the cylindrical coordinates shown in figure 2.3, it has only a z component, since $\mathbf{B}$ has only the $\hat{\boldsymbol{\theta}}$ component and $\boldsymbol{\nabla}\mathbf{B}$ has only $\hat{\mathbf{r}}$ component. We then have:

$$(\nabla \times B)_z = \frac{1}{r}\frac{\partial}{\partial r}(rB_\theta) \qquad B_\theta \propto \frac{1}{r} \tag{2.21}$$

By using equation 2.18 we obtain:

$$\mathbf{v}_{\nabla B} = \frac{m}{2q} v_{\perp}^2 \frac{\mathbf{R}_c \times \mathbf{B}}{R_c^2 B^2} \tag{2.22}$$

that summed to the previous drift gives:

$$\mathbf{v}_{\nabla B} + \mathbf{v}_R = \frac{m}{q} \frac{\mathbf{R}_c \times \mathbf{B}}{R_c^2 B^2} \left(v_{\parallel}^2 + \frac{1}{2} v_{\perp}^2 \right) \tag{2.23}$$

As for the previous drifts, this leads to a net current into the plasma. If the particles have a Maxwellian velocities distribution with an rms velocity v_{th}, equation 2.23 simplifies as [26]:

$$\bar{\mathbf{v}}_{R+\nabla B} = \pm \frac{v_{th}^2}{\mathbf{R}_c \omega_c} \hat{\mathbf{y}} = \pm \frac{\bar{r_c}}{\mathbf{R}_c} v_{th} \hat{\mathbf{y}} \tag{2.24}$$

2.2.3 The plasma trapping

Let us now consider the motion of a charged particle in a magnetic trap. Assume that a magnetic field is pointed primarily in the z direction and its magnitude varies in the z direction. Moreover, consider that $B_\theta = 0$ and $\partial/\partial\theta = 0$: since the lines of force converge and diverge, there is necessarily a component B_r (figure 2.4). We can derive this component by the Maxwell equation $\boldsymbol{\nabla} \cdot \mathbf{B} = 0$:

$$\frac{1}{r} \frac{\partial}{\partial r} (r B_r) + \frac{\partial B_z}{\partial z} = 0 \tag{2.25}$$

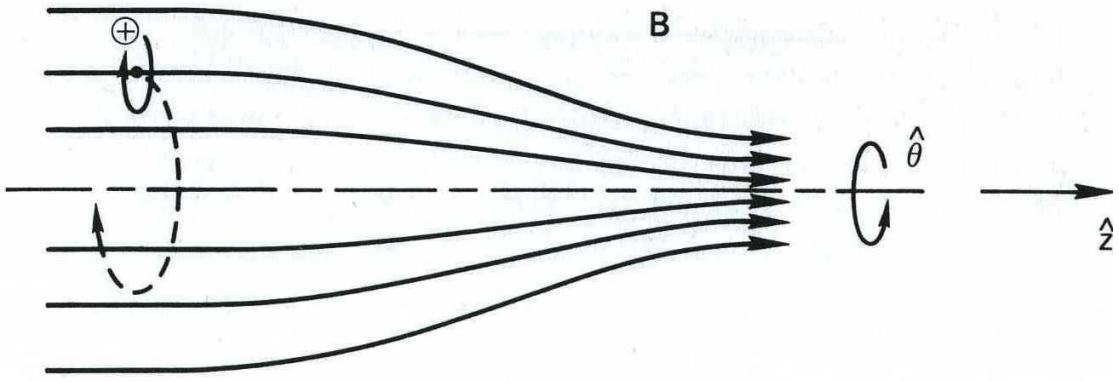

Figure 2.4: Drift of a particle in a magnetic mirror field

If $\partial B_z/\partial z$ is given at $r = 0$ and does not vary much with r, we have approximately:

$$rB_r = -\int_0^r \frac{\partial B_z}{\partial z} dr \simeq -\frac{1}{2} r^2 \left[\frac{\partial B_z}{\partial z}\right]_{r=0} \tag{2.26}$$

The variation of $|B|$ with r causes a gradB drift of the guiding centres about the axis of symmetry, but there is no radial gradB drift because $\partial B/\partial\theta = 0$. The components of the Lorentz force are:

$$\begin{aligned} F_r &= q v_\theta B_z \\ F_\theta &= q\left(-v_r B_z + v_z B_r\right) \\ F_z &= -q v_\theta B_r \end{aligned} \tag{2.27}$$

The first equation and the first term in the second equation give rise to the usual Larmor motion. The second term in the second equation vanishes on axis; when it does not vanish, this azimuthal force causes a drift in the radial direction. This drift merely makes the guiding centers follow the lines of force. By using equation 2.26 the equation for F_z becomes:

$$F_z = \frac{1}{2} q v_\theta r \left(\frac{\partial B_z}{\partial z}\right) \tag{2.28}$$

We must now average over one gyration. For simplicity, consider a particle whose

guiding center lies on the axis. Then v_θ is a constant during the gyration: depending on the sign of q, v_θ is $\mp v_\perp$. Since $r = r_c$, the average force is:

$$\bar{F}_z = -\frac{1}{2}\frac{mv_\perp^2}{B}\frac{\partial B_z}{\partial z} \tag{2.29}$$

We define the **magnetic moment** of the gyrating particle to be:

$$\mu \equiv \frac{1}{2}\frac{mv_\perp^2}{B} \tag{2.30}$$

so that:

$$\bar{F}_z = -\mu\frac{\partial B_z}{\partial z} \tag{2.31}$$

The invariance of μ is the basis for the confinement scheme of the magnetic mirrors. As a particle moves from a weak-field region to a strong-field region it sees an increasing B and, therefore, its $v_\perp$ must increase to keep μ constant. Since the magnetic field cannot change the total energy of the particle, the component $v_\parallel$ must in turn decrease. It can eventually become zero: in this case, the particle is reflected to the weak-field region by the force $\mathbf{F}_\parallel$. An example of such a magnetic configuration is given by a simple pair of coils creating two magnetic mirrors for plasma trapping, as shown in figure 2.5.

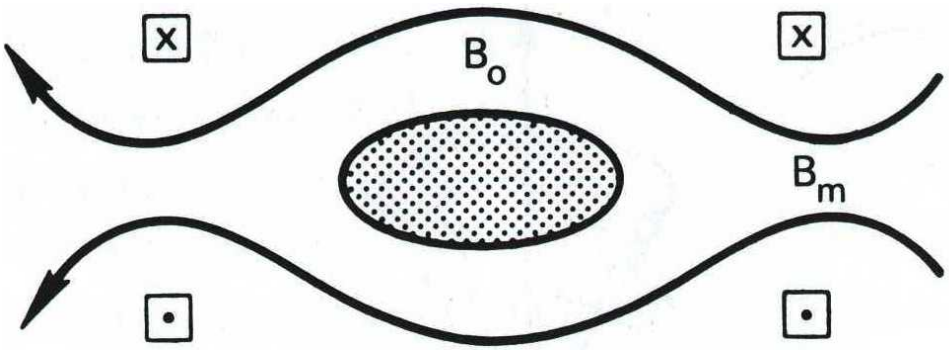

Figure 2.5: A plasma trapped between magnetic mirrors

A trapping is not perfect however. For instance, a particle with $v_\perp = 0$ will have no magnetic moment and will not feel any force along $\mathbf{B}$. A particle with small $v_\perp/v_\parallel$ at the mid-plane ($B = B_0$) will also escape if the maximum field B_m is not large enough, so for given B_0 and B_m it is interesting to know which particles

will escape. A particle with $v_\perp = v_{\perp 0}$ and $v_\parallel = v_{\parallel 0}$ at the mid-plane will have $v_\perp = v'_\perp$ and $v_\parallel = 0$ at its turning point: let the field be B' there. Then, the invariance of μ yields:

$$\frac{1}{2}\frac{mv_{\perp 0}^2}{B_0} = \frac{1}{2}\frac{mv\prime_\perp^2}{B'} \tag{2.32}$$

Conservation of energy requires:

$$v\prime_\perp^2 = v_{\perp 0}^2 + v_{\parallel 0}^2 \equiv v_0^2 \tag{2.33}$$

Combining the last two equations we get:

$$\frac{B_0}{B\prime} = \frac{v_{\perp 0}^2}{v\prime_\perp^2} = \frac{v_{\perp 0}^2}{v_0^2} \equiv \sin^2\theta \tag{2.34}$$

where θ is the pitch angle of the orbit in the weak-field region. Particles with smaller θ will mirror in regions of higher B. If θ is too small, B' exceeds B_m and the particle does not mirror at all. Replacing B' by B_m in equation 2.34 we see that the smallest θ for a confined particle is:

$$\sin^2\theta = B_0/B_m \equiv 1/R_m \tag{2.35}$$

where R_m is called the **mirror ratio**. Equation 2.35 defines the boundary of a region in velocity space in the shape of a cone, called the **loss cone**, as shown in figure 2.6.

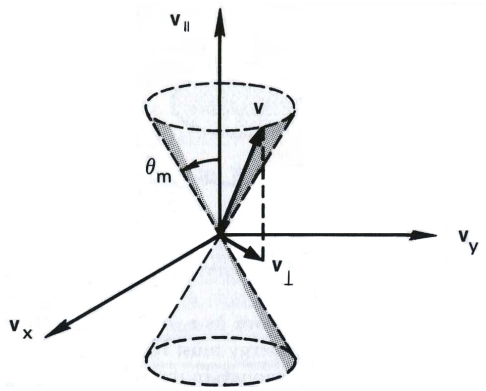

Figure 2.6: The loss cone in velocity space

Particles lying within the loss cone are not confined: consequently, a mirror-confined plasma is never isotropic; note that the loss cone is independent of q and m. Without collisions, both ions and electrons are equally well confined. When collisions occur, particles are lost when they change their pitch angle in a collision and are scattered into the loss cone: generally, electrons are lost more easily because they have a higher collision frequency [39]. It is desirable to have a magnetic configuration whose intensity increases in every direction away from the plasma boundary, without regions where it goes to zero inside the plasma. The **B-minimum** structure typical of ECR ion sources satisfies this condition: its structure is schematically shown in figure 2.7.

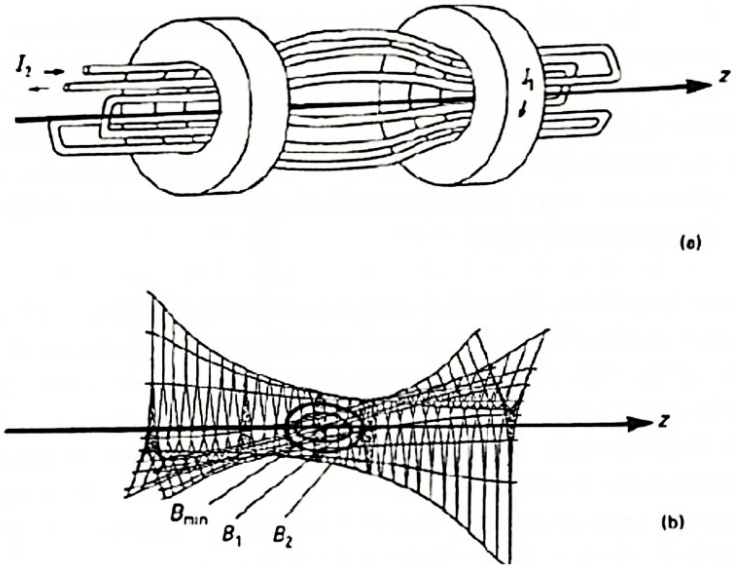

Figure 2.7: Magnetic system (a) and magnetic field structure obtained by the superposition of the field produced by two solenoids and a hexapole (b)

The geometrical locus where B is constant is an egg-shaped surface.

2.3 Spitzer collisions

A very important collective process, responsible for particle losses inside the ECR plasma, is the Spitzer collisions [40]. They represent the interaction of a single particle with many others, with the net effect of obtaining a scattering angle of

90°. In principle, the long-range Coulomb forces between the particles can be extended over the whole plasma. However, to make possible the calculation of the cross-section, it is necessary to choose a distance, the Debye distance, within which the interactions of a charged particle with other charged particles may be supposed to occur. It can be demonstrated that the mean free path for a 90° deflection of a particle of mass M, charge z_1 and velocity v scattered by particles of density n and charge z_2 can be expressed by the relation (in CGS):

$$\lambda_{90^\circ} = [8\pi n(\frac{z_1 z_2 e^2}{Mv^2})^2 ln(\frac{\lambda_D}{b_{min}})]^{-1} \tag{2.36}$$

where λ_D is the *Debye length* and $b_{min} = \frac{2e^2}{Mv^2}$. Now an effective cross section for a 90° deflection by means of multiple collisions can be defined in the usual manner:

$$\begin{aligned} \lambda_{90^\circ} &= \frac{1}{n\sigma 90^\circ} \\ \sigma_{90^\circ} &= 8\pi(\frac{z_1 z_2 e^2}{Mv^2})^2 ln(\frac{\lambda_D}{b_{min}}) \end{aligned} \tag{2.37}$$

Let us now evaluate the characteristic times and frequencies of collective collisions in the center of mass reference frame. The time required for the incident particle to undergo deflection at large angles depends on the relative velocity $v' = v_1 - v_2$ between it and the target and on the reduced mass $M' = \frac{m_1 m_2}{m_1 + m_2}$. Substituting M' and v' in 2.37 we obtain (in MKSA units)

$$\sigma'_{90^\circ} = (\frac{z_1 z_2 e^2}{\epsilon_0 M' v'})^2 \frac{1}{2\pi} ln\Lambda \tag{2.38}$$

from which

$$v_{90^\circ}^{-1} \equiv \tau_{90^\circ} \equiv \frac{\lambda_{90^\circ}}{v'} \tag{2.39}$$

The above expressions give a good estimate for the characteristic times for a deflection of 90° in the laboratory reference system, for both $e-e$ and $e-i$ scattering.

$$\begin{aligned} v_{90^\circ}^{ee} &\approx v_{90^\circ}^{ei} \\ \tau_{90^\circ}^{ee} &\approx \tau_{90^\circ}^{ei} \end{aligned} \tag{2.40}$$

Such characteristic times for Spitzer collisions can be expressed by means of useful formulas:

$$\begin{aligned} v_{90^\circ}^{ee} &= \frac{5x10^{-6}n}{kT_e^{\frac{3}{2}}} ln\Lambda \\ v_{90^\circ}^{ei} &\approx \frac{2x10^{-6}zn}{kT_e^{\frac{3}{2}}} ln\Lambda \\ v_{90^\circ}^{ii} &\approx z^4 (\frac{m_e}{m_i})^{\frac{1}{2}} (\frac{kT_e}{kT_i})^{\frac{3}{2}} v_{90^\circ}^{ee} \end{aligned} \tag{2.41}$$

where n is in cm^{-3} while kT_e and kT_i are the electrons and ions energies (in eV) expressed as a temperature. The energy transferred from particle 1 to particle 2 in a collision can be obtained from the kinematics: for an initial energy E_0 of particle 1, the energy transferred ΔE is given by the relation

$$\frac{\Delta E}{E_0} \approx \frac{m_1 m_2}{(m_1 + m_2)^2} \tag{2.42}$$

From this relationship, it is immediately clear that in the case of like particles the energy transfer is equal to half of the initial energy of the particle 1 while, in the case in which $m_1 << m_2$, the energy transfer is equal to $\frac{m_1}{m_2}$ times the initial energy E_0: consequently, the characteristic time τ_m for the incident particle to transfer, following collisions, all its momentum is correlated to the time necessary for a deflection of 90° from the relations:

$$\begin{aligned} \tau_m^{ee} &\approx \tau_{90^\circ}^{ee} \approx \tau_{90^\circ}^{ei} \\ \tau_m^{ii} &\approx \tau_{90^\circ}^{ii} \approx (\frac{m_i}{m_e})^{\frac{1}{2}} \ \tau_{90^\circ}^{ei} \\ \tau_m^{ei} &\approx \tau_m^{ie} \approx \frac{m_i}{m_e} \ \tau_{90^\circ}^{ei} \end{aligned} \tag{2.43}$$

where $Z = 1$ and $kT_e \approx kT_i$. The time required for an electron to transfer, as a consequence of a collision, the maximum possible energy is less if the other particle involved in the collision is another electron instead of an ion. Consequently, the electrons in an ECRIS plasma exchange energy essentially with each other and can reach thermal equilibrium in a rather short time. Considering the characteristic times in normal ECRIS plasma, we note that ν_{ee} and ν_{ei} are much smaller than ω_c

and the microwave frequency ν. For this reason, they do not impede the electron gyromotion, giving to the ECR plasmas the term *collisionless*. Let's give some numerical examples:

$$n = 10^{11} cm^{-3};\ T_e = 10\, eV \ \Rightarrow\ \nu_{ee} = 10^5 - 10^6 s^{-1} \tag{2.44}$$

from which it is obtained that the electrons reach thermal equilibrium in times of the order of μ_s, while the time required for thermalization by electron-ion collisions is of the order of ms. If the average life of the ions is less than these values, they will never be heated by the e-i collisions and will remain cold.

$$n = 10^{11} cm^{-3};\ T_e = 1\, keV \ \Rightarrow\ \nu_{ee} = 10^2 - 10^3 s^{-1} \tag{2.45}$$

from which it is obtained that for the thermalization of these energetic electrons to occur, times greater than ms would be required. Since their average life is less than these values, it is legitimate to say that they do not have "enough time" to lose such high energy, so it can be assumed that they will keep it throughout their stay inside the chamber (obviously excluding any other type of impact).
The examples above explain why in ECRIS plasma we can find hot electrons mixed with cold ions: the collision frequency of the former particles is so low that their confinement is possible. Finally, the $i - i$ collision rate can become the main scattering agent for these particles because the temperature is very low and $v_{90^\circ}^{ii}$ is proportional to $KT_i^{-3/2}$ and to $z_1 z_2$ [40].

2.4 Binary collisions

Binary collisions are the main mechanism for ions creation and destruction in ECR sources. If v is the relative velocity between interacting particles, the frequency of collisions corresponds to the inverse of the time required to travel a mean free path

$$\tau_c = \frac{\lambda}{v} = \frac{1}{n\sigma v} \tag{2.46}$$

If there is a certain distribution of velocities, such as the Maxwell-Boltzmann distribution, then the collision frequency is obtained by averaging over the distribution:

$$v_c = n < \sigma(v)v > \tag{2.47}$$

The most probable processes occurring in ECR plasmas for the production of multiply charged ions are:

1. Ionizing collisions of energetic electrons on neutral atoms and/or positive ions
2. Charge Exchange Processes between neutral atoms and positive ions.

Both processes will be described in the following subsections.

2.4.1 Ionizing collisions

The ionization cross section has a threshold behaviour to the energy of the electrons E_e. An electron belonging to an atomic subshell can be expelled only if the energy of the incident electron is greater than its binding energy I_k. The single ionization process is schematized by the reaction:

$$e + X^{z+} => X^{(z+1)+} + 2e \tag{2.48}$$

For cross-section calculations of this process, the Lotz's semi-empirical formula is often used [41] [42]:

$$\sigma_k^i = \frac{4.5\,10^{-14}}{E_e} \sum_{k=1}^{m} \frac{n_k}{I_k} log(\frac{E_e}{I_k}) \tag{2.49}$$

where m is the number of atomic subshells of the ion that are occupied, n_k the number of electrons in the considered shell and I_k the binding energy of the shell. The transition by an ion from the charge state z_1 to the charge state z_2, through a given ionization channel x, takes on average a time:

$$\tau_{z_1 z_2}^{(x)} = [n_e \sigma_{z_1 z_2}^{(x)}(v_e) v_e]^{-1} \tag{2.50}$$

which depends directly on the velocity of the electrons. In an ECR source, the electrons have a Maxwellian distribution of velocities: it is, therefore, necessary

to average the time of reaction on the distribution. The averaged time becomes a function of the density and the electron temperature, expressed through the **ionization coefficient** S:

$$S^{(x)}_{z_1 z_2}(T_e) < \sigma^{(x)}_{z_1 z_2}(v_e) v_e >=> \tau^{(x)}_{z_1 z_2} = [n_e \, S^{(x)}_{z_1 z_2}(T_e)]^{-1} \tag{2.51}$$

The transition from state z_1 to state z_2 can occur if the ion confinement time τ_i is greater than or equal to the reaction time, leading to the so-called **criterion for production of multiply charged ions**:

$$n_e \tau_i \geq [S^{(x)}_{z_1 z_2}(T_e)]^{-1} \tag{2.52}$$

Highly charged ions are usually obtained through the **step by step** ionization channel: in this cases the ionization coefficient is expressed by making the substitutions $(x) \rightarrow (i)$, $z_1 \rightarrow z$, $z_2 \rightarrow z+1$. Figure 2.8 shows the graph of the ionization coefficient as a function of the electron temperature in case of oxygen: it is evident the presence of an optimal temperature (T_e^{opt}), which increases as the charge increases z; the ionization coefficient, on the other hand, decreases strongly as z increases. It can be estimated that to optimize the production of a given charge state, the electrons must have a temperature corresponding to 5 times its ionization potential

$$T_e^{opt} \sim 5 \, W_j^{max} \tag{2.53}$$

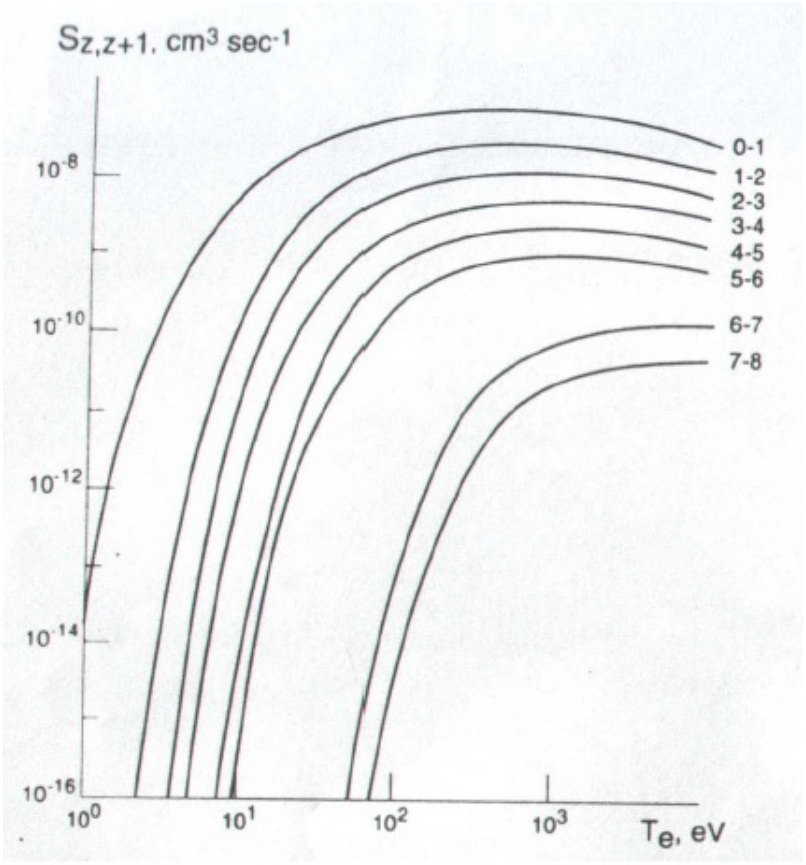

Figure 2.8: Oxygen ionization coefficient as a function of electron temperature.

Starting from this relation and indicating with $\zeta = \sum_{j=1}^{N} q_j$ the total number of electrons in the outermost shell, we obtain a lower limit for $n_e\tau_i$:

$$\zeta n_e \tau_i \leq 5\,10^4 (T_e^{opt})^{\frac{3}{2}} \tag{2.54}$$

The quantity $n_e\tau_i = QF$ is called the **quality factor** and, together with the electron temperature T_e, is a very important parameter that determines the performance of an ECR source. The Figure 2.9 shows the Golovanivsky diagram [43] that correlates the quality factor to the electron temperature: it is a very useful graph for determining the possible performance of a source in terms of charge states obtained, starting from an estimate of the three main parameters (n_e, τ_i, T_e).

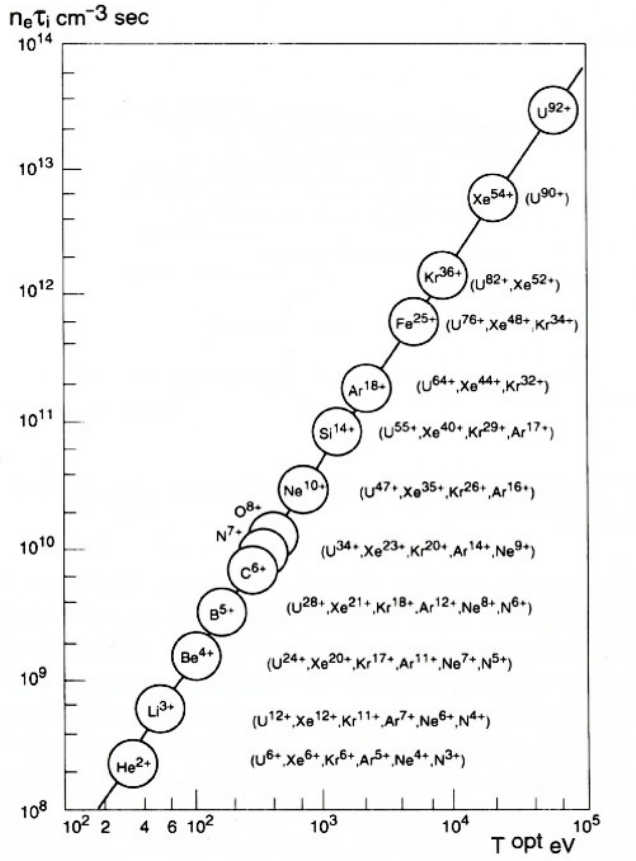

Figure 2.9: Golovanivsky's diagram.

The circles indicate *fully stripped* ions, while the brackets refer to only *partially stripped* ions.

2.4.2 Charge exchange processes

The most important mechanism that lower the average charge state in ECR plasma is the charge exchange process: it consists of a collision between a positive ion and a neutral atom. Both particles form a molecular ion (metastable state) that splits up into two particles following the scheme:

$$A^{z+} + B^0 \Rightarrow (AB)^{z+} \Rightarrow A^{(z-1)+} + B^{1+} \tag{2.55}$$

The charge exchange cross section for the transfer of a single electron is expressed in an approximate way by the Muller-Salzborn formula [44]

$$\sigma_{exc} = 1.43\,10^{-12} z^{1.17} I\, P_0^{-2.76} cm^2 \tag{2.56}$$

This depends on the ionization potential of the neutral atom IP_0 and is valid in the case of interaction between ions of the same species. The charge exchange process limits the average life of an ion in a certain charge state z. In a plasma with neutral particle density n_0 and ions of mass number A, assuming

$$k\,T_i \sim 1\,eV \Rightarrow v_i \sim \frac{10^8}{\sqrt{A}} cm/s \tag{2.57}$$

the estimated average life time is:

$$\tau_{z\to z-1} = [n_0\, v_i\, \sigma_{exc}] \sim 5\,10^8 \frac{\sqrt{A}}{z n_0} \tag{2.58}$$

In order for a certain charge state $z+1$ to form, the charge exchange time $\tau_{z\to z-1}$ must be greater than the ionization time τ_z. By imposing this condition it is possible to obtain an upper limit of the concentration of neutral particles to a given electron density:

$$\frac{n_0}{n_e} \leq 7\,10^3 \zeta (T_e^{opt})^{-\frac{3}{2}} A^{\frac{1}{2}} z^{-1} \tag{2.59}$$

As a numerical example, we calculate the maximum limit to the density of neutral particles to obtain O^{6+}, considering an electron density equal to the critical density at 18 GHz:

$$\left.\begin{aligned} n_e &= 3.24\,10^{12}\, cm^{-3} \\ T_e^{opt} &\sim 400\,eV \\ A &= 18 \\ z &= 6 \\ \zeta &= 2 \end{aligned}\right\} \qquad n_0 \leq 4 \cdot 10^{12}\, cm^{-3} \tag{2.60}$$

2.5 Waves in plasma

This section will deal with the electromagnetic properties of a plasma, considering first the case of a homogeneous and uniform medium and then including a static magnetic field. Finally, the propagation of electromagnetic waves in a magnetized plasma will be described, focusing in particular on the conditions for the ECR resonance to take place and its characteristics [45].

2.5.1 Electromagnetic description of plasmas

When a plasma interacts with an electromagnetic field at high frequency, as in the case of ECR sources, electrons' motion is affected by two forces: the Lorentz force and an impulsive force due to the collisions with all the other plasma particles, that can be indicated as $\mathbf{G} = -m\omega_{eff}\mathbf{v}$. The contribution of the wave's magnetic field, as well as ions' dynamics, are negligible, therefore for non-relativistic electrons the equation of motion is:

$$m\frac{d\mathbf{v}}{dt} = q\mathbf{E} - m\omega_{eff}\mathbf{v} \tag{2.61}$$

For a monochromatic electric field oscillating sinusoidally, the equation admits the particular solution $\mathbf{v} = \mathbf{v}_0 e^{.i\omega t}$. Substituting we obtain:

$$\mathbf{v} = \frac{q\mathbf{E}}{(\omega_{eff} - i\omega)m} \tag{2.62}$$

Knowing the velocity, the current density can be calculated:

$$\mathbf{J} = nq\mathbf{v} = \frac{nq^2\mathbf{E}}{(\omega_{eff} - i\omega)m} = \frac{\epsilon_0\omega_{eff}\omega_p^2}{(\omega^2 + \omega_{eff}^2)}\mathbf{E} + i\omega\frac{\epsilon_0\omega_p^2}{(\omega^2 + \omega_{eff}^2)}\mathbf{E} \tag{2.63}$$

where ω_p is the plasma frequency. From Eq.2.63, it is evident that a plasma can be considered as a *dielectric medium with losses* characterized by the following

parameters:

$$\begin{aligned} \sigma &= \frac{\epsilon_0\,\omega_{eff}\,\omega_p^2}{\omega^2+\omega_{eff}^2} \\ \epsilon &= \epsilon_0(1-\frac{\omega_p^2}{\omega^2+\omega_{eff}^2}) \\ \mu &= \mu_0 \end{aligned} \tag{2.64}$$

They depend on the frequency of the electromagnetic wave: this means that a plasma is a *dispersive medium*. For a transverse electromagnetic wave propagating in a homogeneous and isotropic plasma, it is possible to define a complex wave vector:

$$\begin{aligned} k^2 &= \omega^2\mu_0\epsilon + i\omega\mu_0\sigma \\ k &= \beta + i\alpha \end{aligned} \tag{2.65}$$

where

$$\begin{aligned} \beta &= \omega\sqrt{\frac{\mu_0\epsilon}{2}\left[\sqrt{1+\frac{\sigma^2}{\epsilon^2\omega^2}}+1\right]} \\ \alpha &= \omega\sqrt{\frac{\mu_0\epsilon}{2}\left[\sqrt{1+\frac{\sigma^2}{\epsilon^2\omega^2}}-1\right]} \end{aligned} \tag{2.66}$$

If the plasma doesn't have loss ($\omega_{eff}=0$), one has

$$\epsilon = \epsilon_0\left(1-\frac{\omega_p^2}{\omega^2}\right);\ \sigma = 0 \rightarrow \textit{dielectric medium} \tag{2.67}$$

If $\omega=\omega_p \rightarrow \beta=0;\ \alpha=0;\ n=0$: the wave has the magnetic field uguals to zero and the electric field is irrotational. The frequency satisfying the condition $\omega=\omega_p$ is called the *cut-off frequency*. From it and using equation 2.3 is to possible to define the plasma cut-off density:

$$n_{cut-off} = \frac{\epsilon_0 m}{e^2}(2\pi\nu)^2 = \frac{\epsilon_0 m}{e^2}\omega^2 \tag{2.68}$$

2.5.2 Electromagnetic description of plasmas under a magnetic field

By adding a static magnetic field to the Lorentz force in equation 2.61 it becomes:

$$m_e \frac{d\mathbf{v}}{dt} = q_e\mathbf{E} - m\mathbf{v}\omega_{eff} + q_e\mathbf{v} \times \mathbf{B}_0 \tag{2.69}$$

If the magnetic field is directed along the z axis $\mathbf{B}_0 = B_0\hat{z}$ and considering a steady state solution for the velocity of the form $\mathbf{v} = e^{i\omega t}\mathbf{v}_0$, equation 2.69 can be written as:

$$(-i\omega + \omega_{eff})\mathbf{v} + \omega_g\hat{z}x\mathbf{v} = \frac{q_e\mathbf{E}}{m} \tag{2.70}$$

where ω_g is the electron's cyclotron frequency. The three components of equation 2.70 along the coordinates axes can be written as:

$$\begin{aligned} v_x &= \frac{q_e}{m}\frac{-i\Omega E_x + \omega_g E_y}{\omega_g^2 - \Omega^2} \\ v_y &= \frac{q_e}{m}\frac{-i\Omega E_y - \omega_g E_x}{\omega_g^2 - \Omega^2} \\ v_z &= \frac{q_e}{m}\left(\frac{E_z}{-i\Omega}\right) \end{aligned} \tag{2.71}$$

where $\Omega = \omega + i\omega_{eff}$. From equantion 2.71 the current density vector $\mathbf{J} = nq_e\mathbf{v}$ can be obtained:

$$\begin{aligned} J_x &= \frac{nq_e^2}{m}\frac{-i\Omega}{\omega_g^2 - \Omega^2}E_x + \frac{nq_e^2}{m}\frac{\omega_g}{\omega_g^2 - \Omega^2}E_y \\ J_y &= \frac{nq_e^2}{m}\frac{-\omega_g}{\omega_g^2 - \Omega^2}E_x + \frac{nq_e^2}{m}\frac{-i\Omega}{\omega_g^2 - \Omega^2}E_y \\ J_z &= \frac{nq_e^2}{m}\frac{1}{-i\Omega}E_z \end{aligned} \tag{2.72}$$

A plasma subjected to an external magnetic field $\mathbf{B}_0$ becomes also an anisotropic medium. The current density vector $\mathbf{J}$ is no longer parallel to the electric field $\mathbf{E}$ and the dielectric constant becomes a tensor. The matrix elements of the tensor can be found from Maxwell's equations:

$$\nabla\ x\ \mathbf{H} = \mathbf{J} - i\omega\epsilon_0\mathbf{E} = -i\omega\epsilon' \cdot \mathbf{E} = -i\omega\mathbf{D} \tag{2.73}$$

where $\mathbf{D} = \epsilon_0\mathbf{E} - \mathbf{P}$ is the **electric induction**, P is the **electric polarization**, while $\mathbf{H} = \frac{\mathbf{B}}{\mu_0} - \mathbf{M}$ is the magnetic field in the material which takes into account the magnetic polarization. It is worth noticing that $\mathbf{D}$ and $\mathbf{E}$ are not parallel, because $\mathbf{D} = \frac{J}{-i\omega} + \epsilon_0\mathbf{E}$. By making this last relation explicit, we arrive at the expression of the matrix which represents the complex dielectric tensor:

$$\epsilon' = \begin{pmatrix} \epsilon'_{xx} & \epsilon'_{xy} & 0 \\ \epsilon'_{yx} & \epsilon'_{yy} & 0 \\ 0 & 0 & \epsilon'_{zz} \end{pmatrix} \tag{2.74}$$

The matrix elements are:

$$\begin{aligned} {\epsilon_{xx}}' = {\epsilon_{yy}}' &= \epsilon_0\left(1 - \frac{X(1+iZ)}{(1+iZ)^2 - Y^2}\right) \\ {\epsilon_{xy}}' = -{\epsilon_{yx}}' &= i\epsilon_0\frac{XY}{(1+iZ)^2 - Y^2} \\ {\epsilon_{zz}}' &= \epsilon_0\left(1 - \frac{X}{1+iZ}\right) \end{aligned} \tag{2.75}$$

where $X = (\frac{\omega_p}{\omega})^2$; $Y = -\frac{\omega_g}{\omega}$; $Z = \frac{\omega_{eff}}{\omega}$.
As will be clearer in the next subsection, the allowed polarizations will depend on the direction of propagation with respect to the magnetic field.

2.5.3 Waves' propagation in a plasma in the presence of a magnetic field

Plasma is both inhomogeneous and anisotropic when immersed in a magnetic field: this is exactly what happens for ECR plasmas and this characteristic influences the possible polarization of the electromagnetic field. The wave vector k of an electromagnetic wave propagating in plasma depends on the angle θ formed by the incoming wave with the magnetic field direction. It can be demonstrated that, for a given angle of propagation with respect to the magnetic field, two different

constants of propagation exist for the wave [45]:

$$\begin{aligned} k_\theta^{'} &= \frac{\omega}{c}\sqrt{1-\frac{X(1+iZ-X)}{(1+iZ)(1+iZ-X)-\frac{1}{2}Y_T^2+\sqrt{\frac{1}{4}Y_T^4+Y_L^2}(1+iZ-X)^2}} \\ k_\theta^{''} &= \frac{\omega}{c}\sqrt{1-\frac{X(1+iZ-X)}{(1+iZ)(1+iZ-X)-\frac{1}{2}Y_T^2-\sqrt{\frac{1}{4}Y_T^4+Y_L^2}(1+iZ-X)^2}} \end{aligned} \tag{2.76}$$

In the above formulas $Y_T = Y sin\theta$ and $Y_L = Y cos\theta$. It is interesting to consider the two extreme conditions.

For $\theta = 0°$:

$$k_0^{'} = \frac{\omega}{c}\sqrt{1-\frac{X}{1+Y}} = \frac{\omega}{c}\sqrt{1-\frac{\omega_p^2}{\omega(\omega-\omega_c)}} \tag{2.77}$$

$$k_0^{''} = \frac{\omega}{c}\sqrt{1-\frac{X}{1-Y}} = \frac{\omega}{c}\sqrt{1-\frac{\omega_p^2}{\omega(\omega+\omega_c)}} \tag{2.78}$$

Maxwell's equations admit two circularly polarized waves, respectively right and left-handed, with different propagation constants. In the case of a right-handed circularly polarized, when $\omega = \omega_g$, the electron will absorb energy from the electromagnetic field and will be able to ionize other atoms by impact. This is the base mechanism of the ECR resonance.

For $\theta = 90°$:

$$k_{90}^{'} = \frac{\omega}{c}\sqrt{1-\frac{\omega_p^2}{\omega^2}} \tag{2.79}$$

$$k_{90}^{''} = \frac{\omega}{c}\sqrt{1-\frac{\frac{\omega_p^2}{\omega}}{1-\frac{\omega_g^2}{\omega_g^2-\omega_p^2}}} \tag{2.80}$$

The wave of Eq.2.79 has the electric field vector linearly polarized along the z axis: the electromagnetic wave is therefore of the TEM type. The wave of Eq. 2.80 has the magnetic field vector orthogonal to the direction of propagation and parallel to the magnetostatic field: consequently the wave is of the TM type. The polarization of the electric field vector is elliptical.

From the **Appleton-Hartree equation** it is possible to obtain the *refractive index* for the propagation of an electromagnetic wave in a magnetized plasma:

$$n_\theta^2 = 1 - \frac{2X(1-X)}{2(1-X) - Y^2 \sin\theta^2 \pm \sqrt{Y^4 \sin\theta^4 + 4Y^2(1-X)^2}} \tag{2.81}$$

From the Eq. 2.81 it is possible to define four regions of propagation:

- $n > 0$ **propagation region**: the wave propagates with a phase velocity $\frac{c}{n}$;
- $n < 0$ **rejection region**: the wave cannot be propagated;
- $n = 0$ **cut-off**: the wave is reflected;
- $n \to \infty$ **resonant**: the wave is absorbed.

The resonance depends on the propagation angle and can only takes place in the region where $X < 1$:

$$\omega_p^2 < \omega^2 \ \rightarrow \ n_e < n_{cut-off}$$

The last relation tells us that a wave can be absorbed only by plasmas of moderate density: this is the reason why ECR plasmas are usually termed underdense.
In the two limit cases, we obtain:

- $n^2(0) = 1 - \frac{X}{1-Y}$
- $n^2(\frac{\pi}{2}) = 1 - \frac{X(1-X)}{1-X-Y^2}$

The first relation is an alternative way to express the condition for the ECR resonance to take place, that is $Y = 1$ or equivalently:

$$\omega_g = \omega$$

2.6 ECR HEATING

A simplified way to describe the particle acceleration in presence of the ECR resonance, deeply studied by Jaeger, Lieberman and Lichtenberg [46] [47], is due to Delcroix [48]. The interaction between an electron and the electromagnetic wave can be thought of as an electron moving in a rotational motion on a fixed plane

in space and interacting with a right-handed circularly polarized standing electromagnetic wave. In the case of synchronous motion and phase (ϕ) favourable to acceleration, an increase in velocity orthogonal to the magnetic field $v_\perp$ is obtained. The resulting motion is:

$$\mathbf{v} = \frac{q_e}{m}\mathbf{E}t + \omega \times \mathbf{r}_c + \mathbf{v}_\parallel$$

The first term depends on the electric field, the second on the magnetic field, while the initial velocity determines the modulus of the curvature radius and of the parallel velocity. The perpendicular velocity can be expressed as:

$$\mathbf{v}_\perp(t) = \frac{q_e}{m}\mathbf{E}t_0\sqrt{[1 + \frac{2t}{t_0}\cos\phi + \frac{t^2}{t_0^2}]}$$

with $t_0 = \frac{q_e}{m}\frac{v_\perp(0)}{E}$.

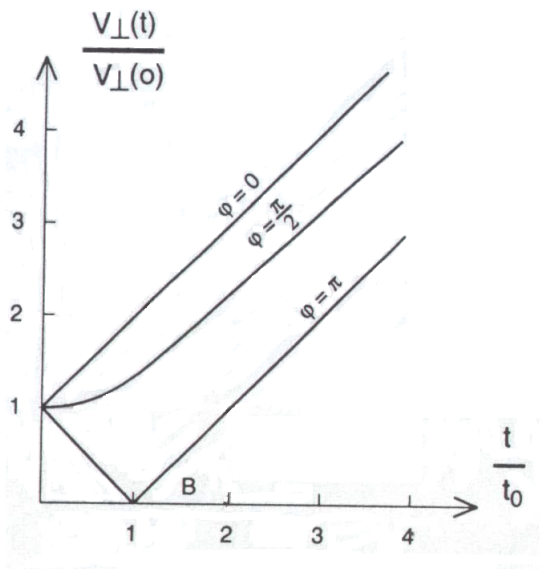

Figure 2.10: Trend of electron's velocity as a function of the time spent at the resonance for different initial phases with respect to the electromagnetic field.

Figure 2.10 shows the trend of $v_\perp(t)$ versus the time: it is clear that for $\phi = \pi$, the electron is decelerated first and then accelerated when $t > t_0$; at this time all the electrons are accelerated proportionally to the time and regardless of ϕ. After

some time one has $v_\perp \gg v_{\parallel 0}$ and can write:

$$\mathbf{v}_\perp = \frac{q_e}{m}\mathbf{E}t = \mathbf{g}\, c\, \omega\, t \rightarrow g = \frac{q_e E}{m\, c\, \omega}$$

From figure 2.10 it is possible to deduce that if $\frac{t}{t_0} > 1$, all electrons will be accelerated, regardless of the value of the initial phase. In this case $v_\perp = (\frac{q}{m})E\,t = g\, c\, \omega\, t \gg v_{\perp 0}$. The energy becomes:

$$\frac{W_\perp}{mc^2} = \frac{1}{2} g^2\, \omega^2\, t^2 \tag{2.82}$$

When we neglect relativistic mass variations, it gets:

$$\frac{W_\perp}{m_0 c^2} = \frac{1}{2} g^2\, \omega^2\, t^2$$

where in this case $\omega = \frac{eB}{m_0 c} = \omega_g$.
A fundamental contribution to the understanding of the ECR resonance in presence of a magnetic field gradient was proposed by Canobbio in 60's [49]: he considered collisionless plasmas and defined some dimensionless quantities that are useful to simplify the treatment. Besides the already seen g, he introduced other two quantities:

- $\delta = \frac{1}{|B_0|}[\frac{d|B_0|}{dz}]$
- $Z = \frac{\omega_g}{\omega} = \frac{q_e B}{m\omega}$

When the magnetic field is not uniform, the electron takes a finite time to cross the resonance region from which it emerges with energy dependent on the gradient of the field. Canobbio's theory describes the phase shift between the electron and the wave in two extreme cases, namely with a weak magnetic field gradient and another with a strong gradient.

1. **Weak magnetic gradient**. In the first case it can be shown that an expression for energy is:

$$W_\perp^{MAX} \sim m\, c^2\, g^{2/3} => W_\perp^{MAX}(eV) \sim 1.5\, 10^9 (\frac{E[\frac{V}{cm}]}{\omega})^{\frac{2}{3}}$$

where we note the absence of a parameter dependent on the magnetic field.

2. **Strong magnetic gradient**. In the second case the energy can be expressed as:

$$W_{\perp} \sim 2.9\, m\, c^2 (\frac{g^3}{\delta^2})^{\frac{2}{5}}$$

in which a dependence on the magnetic field is contained in term δ.

If we consider the single transit through the ECR resonance, it is possible to distinguish different populations of electrons:

- **Electrons crossing only one time the ECR**
  This condition is verified for those electrons that, after transversing the ECR resonance one time, lose energy due, for example, to the emission of synchrotron radiation. As a consequence of the invariance of the magnetic moment $\mu = \frac{W_{\perp}}{B}$, if $W_{\perp}$ gradually decreases then the possible values of B at which the electrons reverse their motion become smaller. The electrons, therefore, oscillate back and forth in the magnetic trap with ever smaller amplitudes and will not be able to reach the ECR a second time.

- **Electrons passing through the ECR resonance proceeding towards increasing magnetic field values**
  These electrons undergo an increase of $W_{\perp}$ which leads to a decrease of $v_{\parallel}$. The transit time through the ECR increases causing a phase shift between the motion of the electron and that associated with the rotation of the electric field vector of the right-handed circularly polarized wave. When the longitudinal component of the velocity is cancelled, the electron stops and the magnetic force $\mathbf{F} = -\mu \nabla B$ brings them toward the centre of the trap.

- **Electrons which, following the crossing of the ECR resonance, are expelled within the loss cone**
  The particles within the loss cone are characterized by a small $\frac{v_{\perp}}{v_{\parallel}}$ ratio. The ECR resonance involves an increase in the perpendicular component of the velocity that increases this ratio and can lead the particle to be expelled by the loss cone.

If we consider the transit of multiple electrons in the ECR resonance, it leads to time-mediated heating, as the particles have a certain velocity distribution. When an electron crosses the resonance it gains an energy ΔW proportional to

the energy density and transit time Δt through the resonance: the **heating rate** will be $H = \frac{\Delta W}{\Delta t}$.

2.7 Techniques to improve the ECRIS performances

The scientific community requires higher and higher ion beams intensities. To produce these currents, continuous improvements in the performances of ECR ion sources are needed. For many years these improvements consisted principally in the use of higher power of RF wave heating, and a more intense magnetic field, based on the "scaling laws" [1]. More recently, this approach has become more difficult because of the technological limits. A deeper knowledge of plasma parameters (electron density, temperature and charge state distribution) is thus fundamental: characteristics of the extracted beam (in terms of intensity and production of high charge states) are directly connected with plasma parameters and structure. There are several techniques to improve the parameters of ECR sources, the most important being:

1. the Two Frequency Heating (TFH) [2] [3] [4];
2. the Two Close Frequency Heating (TCFH) [5] [6];
3. the Frequency Tuning (FT) [7] [8] [9].

All the above-mentioned techniques aim at optimizing the electromagnetic field set-up inside the plasma, thus improving the energy transfer to plasma electrons and in turn the extracted intensities. Being an alternative approach concerning the one adopted to obtain the results presented in this thesis, a brief description will be given in the following.

2.7.1 Frequency Tuning

The performance of an ECR source is quantified based on the intensity of the current of the extracted beam and the charge state. Ions are guided to the extraction by the magnetic field lines originating from specific parts of the resonant surface,

therefore it is essential to optimize the distribution of the electric field in that region. The Eq. 2.82 shows the dependence of energy on $|\mathbf{E}|^2$, so it is important to maximize this value in those locations. Anyway, there is a limit to the power that we can introduce into the source, beyond which a population of excessively energetic electrons (*hot electrons*) is created which are not effective in the ionization process. For this reason, the optimization of the electromagnetic field at the resonance pass through the research of the optimum value of the frequency to excite and sustain the plasma. Many experiments have shown that small variations in the excitation frequency can increase the ion output current from the source. The **Frequency Tuning** (**FT**) technique consists in modifying the microwave frequency in order to obtain more intense and better distributed electric fields on the resonance surface. Some studies have been carried out to prove the efficiency of the FT, as can be found in [7]. To have a clearer view of the FT effect, in the figure 2.11 we can see the electromagnetic field distribution on the resonance surfaces of the **SERSE ECR source** (installed at the LNS in Catania) generated by two different frequencies.

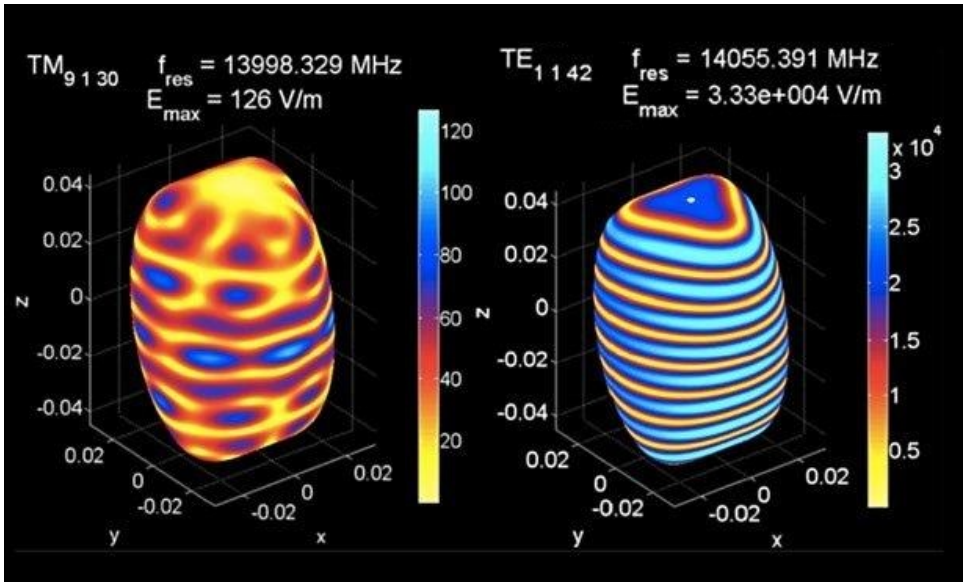

Figure 2.11: Electric field distribution on the resonance surface of the SERSE ECR source: on the left the frequency of 13.998 GHz; on the right the frequency of 14.055 GHz.

It is evident how a small variation of the frequency (50 MHz on about 14 GHz) can lead to a very different electromagnetic field distribution. The absolute value of the electric field is also affected, with two orders of magnitude of difference for the two cases.
In Figure 2.12, we can see an example of how the FT can affect the C^{4+} intensity extracted from a SUPERNANOGAN type ECRIS developed by Pantechnik [50] ed installed at CNAO facility [51]. It shows the intensity variation as a function of the frequency, varying in the range 14.44 GHz - 14.53 GHz at a step of 10 MHz. Variations up to a factor of two are observed for frequencies very close to each other.

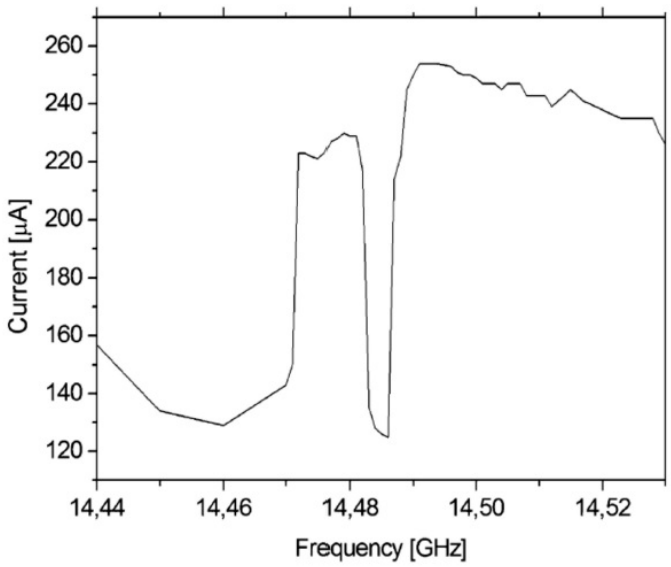

Figure 2.12: Frequency tuning effect on the C^{4+} intensity extracted from the ECR source installed at CNAO facility.

2.7.2 Two Frequency Heating and Two Close Frequency Heating

To create and sustain a plasma with highly charged ions, a single microwave frequency is typically used. By employing two different frequencies it is possible to produce two concentric ECR surfaces, whose separation depends on the difference in frequency and on the magnetic field gradient. If such a difference is significant,

the two surfaces are separated and heating leads to a higher population of energetic electrons with a consequent increase in the efficiency of the source. So, the amplitude of the resonance zone is substantially increased, allowing electrons that did not gain energy in the first crossing to do so in the second. Therefore, with the same power of the microwaves, the two frequency heating produces, in some cases, better results than the single frequency.
The first tests regarding the mechanism of TFH were performed with the Lawrence Berkeley Laboratory's AECR (advanced ECR) source, using frequencies of 10 GHz and 14 GHz [52]. With a difference of 4 GHz, the two resonance surfaces are well separated, as shown in figure 2.13.

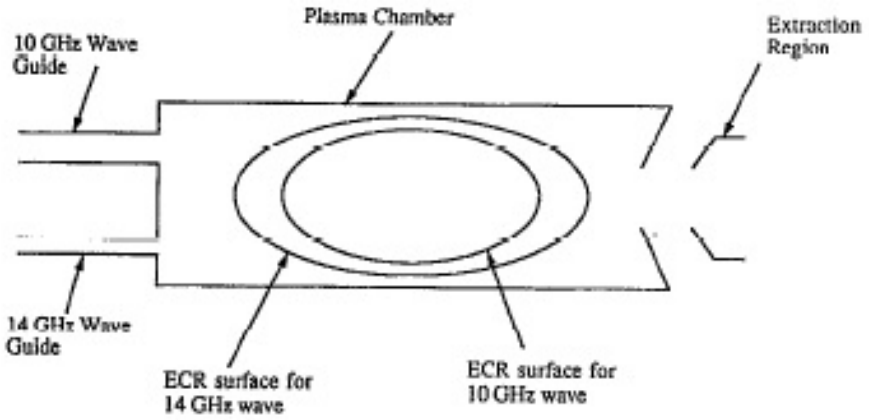

Figure 2.13: Schematic of the ECR resonance surfaces in the plasma chamber of the AECR source installed at LBNL.

The experiments revealed an improved stability of the plasma. Comparing the performance of the source with the two frequency heating and with the single frequency heating, it has been observed the first technique provides a marked improvement in the case of ion beams with a high charge state, as shown in figure 2.14.

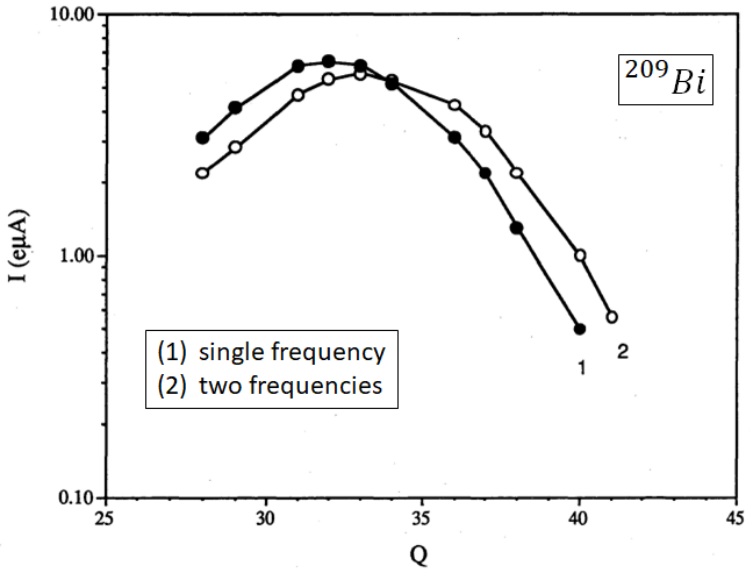

Figure 2.14: Charge distributions for ^{209}Bi produced in single and two frequency heating for the same microwave power: curve (1) 14 GHz at 1150 W; curve (2) 14 GHz at 880 W and 10 GHz at 300 W.

It shows the extracted currents of different charge states for ^{209}Bi, using the Single Frequency (14 GHz with a power of 1150 W) and Two Frequency Heating (14 GHz with a power of 880 W and 10 GHz at 300 W). It can be seen that the peak shifts from 32^+ to 33+ and the intensity of the beam current increase up to a factor of two for charge states from 36^+ to 40^+.
In the TFH the two frequencies must be separated, while in the Two Close Frequency Heating technique (TCFH) the two waves introduced into the plasma chamber have very similar frequencies. In this case, the resonance surfaces will be very close, creating the **electron surfing** phenomenon. Consequently, the electrons leaving the first ECR resonance undergo a further acceleration by the second, which depends on the phase difference between the two waves. To make this happen, the resonant surface corresponding to the frequency of the second wave must be located where the first ends. Canobbio [49] was the first who studied this phenomenon, estimating that the frequency difference between the two waves should allow two contiguous resonance zones, being approximately 100 MHz for typical source parameters.

Chapter 3

Electromagnetism in ECR ion sources

This chapter describes the electromagnetic theory underlying the microwave components used in the ECR sources. In particular, it will show the equations of the electromagnetic fields set up in cylindrical waveguides and the cylindrical resonant cavities. Before doing this and for the sake of completeness, the typical microwave injection system will be described. Figure 3.1 shows an example of the main RF components employed to run the LEGIS (LEGnaro ecrIS [53]) ECR source installed at INFN-LNL.

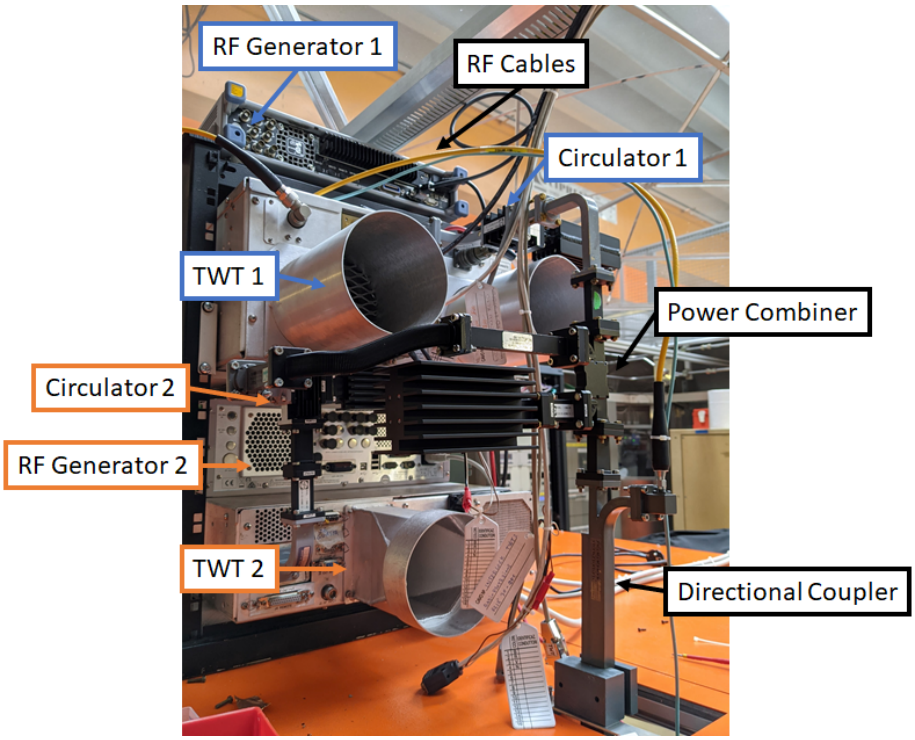

Figure 3.1: Microwave system setup for the LEGIS ECR source installed at INFN-LNL.

One or two travelling wave tube amplifiers (TWT) increase the amplitude of the signals coming from RF generators. In order to avoid possible failures due to the power reflected from the source, circulators are usually employed: basically they deliver the reflected power on dummy loads instead of the amplifiers. The power combiner is useful when a single injection port is available, because it can combine two different frequencies in a single waveguide. To measure the power reflected and transmitted from/to the ion source a directional coupler with suitable probes is normally used.

3.1 Waveguides

The frequencies used in ECR sources are in the order of tens GHz and are guided inside standard metallic WR rectangular waveguides. The code WR is usually followed by a number that indicates the internal width of the waveguide in hun-

dredths of an inch, thus the allowed frequency range. As an example, ECR sources operating at about 14 GHz employ WR75 (allowed frequency range 10 GHz - 15 GHz) and WR62 waveguides (12 GHz - 18 GHz). The electromagnetic study of the cylindrical resonant cavities can be derived from the theory of circular waveguides, so it is useful to study them first. Considering a reference system of cylindrical coordinates, the equations of electric and magnetic fields for the wave propagations in a metallic cylindrical waveguide of radius a (schematically shown in figure 3.2) are [45]:

$$\begin{aligned} E_r &= -\frac{1}{\gamma^2 - k^2}\left(j\frac{\omega\mu}{r}\frac{\partial H_z}{\partial \phi} + \gamma\frac{\partial E_z}{\partial r}\right) \\ E_\phi &= -\frac{1}{\gamma^2 - k^2}\left(-j\omega\mu\frac{\partial H_z}{\partial r} + \frac{\gamma}{r}\frac{\partial E_z}{\partial \phi}\right) \\ H_r &= -\frac{1}{\gamma^2 - k^2}\left(-j\frac{\omega\epsilon}{r}\frac{\partial E_z}{\partial \phi} + \gamma\frac{\partial H_z}{\partial r}\right) \\ H_\phi &= -\frac{1}{\gamma^2 - k^2}\left(j\omega\epsilon\frac{\partial E_z}{\partial r} + \frac{\gamma}{r}\frac{\partial H_z}{\partial \phi}\right) \end{aligned} \tag{3.1}$$

where ω is the angular frequency, γ is the propagation constant, $k = \frac{2\pi}{\lambda}$ is the wavenumber

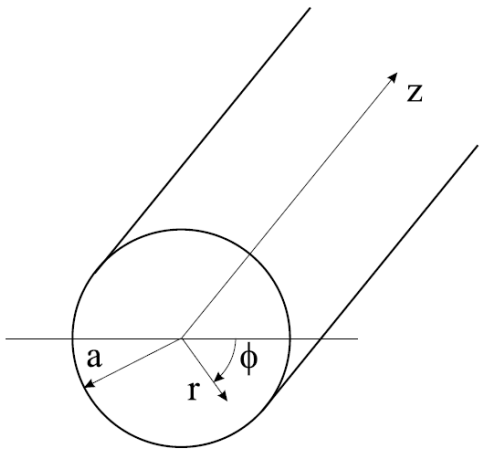

Figure 3.2: Schematic rappresentation of a cylindrical wave guide.

The tangential component of the electric field to the electric conductor surface is null, so the normal component of the magnetic field must also be zero on the

contour. This translates in $E_z = 0$, $\frac{\partial H_z}{\partial r} = 0$, from which can rewrite the Eq. 3.1:

$$\begin{aligned} \frac{1}{r}\frac{\partial}{\partial r}\big(r\frac{\partial E_z}{\partial r}\big) + \frac{1}{r^2}\frac{\partial^2 E_z}{\partial \phi^2} &= -\chi^2 E_z \\ \frac{1}{r}\frac{\partial}{\partial r}\big(r\frac{\partial H_z}{\partial r}\big) + \frac{1}{r^2}\frac{\partial^2 H_z}{\partial \phi^2} &= -\chi^2 H_z \end{aligned} \tag{3.2}$$

where $\chi^2 = -k^2 + \gamma^2$.
It is possible to separate the variables, writing $E_z(r,\phi), H_z(r,\phi) = R(r) \cdot \Phi(\phi)$. Since the function $\Phi(\phi)$ is periodic with period of 2π, it can be expanded in Fourier series as $\Phi(\phi) = \sum_{-\inf}^{+\inf} \phi_n e^{jn\phi}$, obtaining for each n:

$$\ddot{R}(r) + \frac{1}{r}\dot{R}(r) + \big(\chi^2 - \frac{n^2}{r^2}\big)R(r) = 0 \tag{3.3}$$

Equation 3.3 is the **Bessel equation of integer order n**, whose general solution can be written as a linear combination of a Bessel function of the first kind of order n and a Bessel function of the second kind of order n:

$$R(r) = AJ_n(\chi r) \tag{3.4}$$

where J_n is the Bessel function of order n.
The boundary conditions must be imposed in r = a, the radius of the waveguide, so the domain of definition of the electromagnetic fields is $0 \leq r \leq a$. Two different modes of propagation are allowed inside the waveguide:

1. **TE Modes**. In this case $R(r)\Phi(\phi) = H_z(r,\phi)$ and the boundary condition is:

$$\big(\frac{dR(r)}{dr}\big)_{r=a} = \chi A\dot{J}_n(\chi a) = 0 \tag{3.5}$$

The equation 3.5 can be satisfied for several values of the argument of the Bessel function. If $\dot{p}_{n,m}$ is the m^{th} zero of the derivative of the Bessel function of the first kind of order n, these zeros will correspond to a mode $TE_{n,m}$ of the circular waveguide. Table 3.1 shows the values of some zeros of the first derivatives of the Bessel functions of the first type: from those values, it is possible to calculate the eigenvalues corresponding to each mode of propagation. The same table shows that the smallest value among the Bessel

functions of the first type is $\dot{J}_1(u)$, from which:

$$\chi_{1,1} = \frac{\dot{p}_{1,1}}{a} \simeq \frac{1.84118}{a}$$

The **critical frequency**, or also **cut-off frequency** ν_c is defined as the minimum propagation frequency in the waveguide:

$$\nu_c = \frac{2\pi a}{\dot{p}_{1,1}}$$

It follows that, among the TE modes, the mode with the lowest critical frequency is the $TE_{1,1}$ mode;

Table 3.1: Some zeros of the derivatives of some Bessel functions of the first type

	$\dot{J}_0(u)$	$\dot{J}_1(u)$	$\dot{J}_2(u)$	$\dot{J}_3(u)$	$\dot{J}_4(u)$	$\dot{J}_5(u)$
First zero	3.83171	1.84118	3.05424	4.20119	5.13755	6.41562
Second zero	7.01559	5.33144	6.70613	8.01524	9.28240	10.51986
Third zero	10.17347	8.53632	9.96947	11.34592	12.68191	13.98719
Fourth zero	13.32369	11.70600	13.17037	14.58585	15.96411	17.31284

2. **TM Modes**. In this case $R(r)\Phi(\phi) = E_z(r, \phi)$ and the boundary condition is:

$$R(r)_{r=a} = AJ_n(\chi a) = 0 \tag{3.6}$$

Indicating with $p_{n,m}$ the n^{th} zero of the Bessel function of the first kind of order n, this zero will correspond to the $TM_{n,m}$ mode of the circular waveguide. Table 3.2 shows the values of some zeros of first Bessel functions of the first type:

Table 3.2: Some zeros of some Bessel functions of the first type

	$J_0(u)$	$J_1(u)$	$J_2(u)$	$J_3(u)$	$J_4(u)$	$J_5(u)$
First zero	2.40512	3.83171	5.13562	6.38016	7.58834	8.77418
Second zero	5.52007	7.01559	8.41724	9.76102	11.06471	12.33860
Third zero	8.65372	10.17347	11.61984	13.01520	14.37254	15.70017
Fourth zero	11.79153	13.32369	14.79595	16.22347	17.61597	18.98013

The table shows that the smallest eigenvalue χ^2 corresponds to the mode $TM_{0,1}$ for which we have:

$$\chi_{0,1} = \frac{p_{0,1}}{a} \simeq \frac{2.405}{a}$$

Comparing the $TM_{0,1}$ and the $TE_{1,1}$ mode, we see that the latter has the lowest cut-off frequency and is therefore considered the **fundamental mode** of the circular waveguide.

3.2 Cilindrical cavities

The plasma chamber of an ECR source, working as a resonant cavity, has usually a cylindrical shape: for this reason, it is important to derive the equations for the modes allowed in a given structure. A **resonant cavity** is defined as a volume V enclosed by a metal surface and in which an electromagnetic field is excited. There are three different classes of cavities [54]:

1. **Ideal cavity**. A completely closed cavity filled with a lossless dielectric and limited by a perfect metal surface.

2. **Real cavity**. An ideal cavity where the limiting case of perfect conductor and lossless dielectric are not satisfied.

3. **Coupled cavity**. The real cavity with an aperture through which electromagnetic power can be coupled.

As we have seen for waveguides, even in resonators the electric and magnetic fields can exist only at certain frequencies called resonance frequencies (**TM** and **TE** modes). A cylindrical resonant cavity (see Fig. 3.3) can be obtained from a circular waveguide (see paragraph 3.1) of radius a, closed at both ends by metal plates normal to the waveguide axis and placed at a distance b from each other.

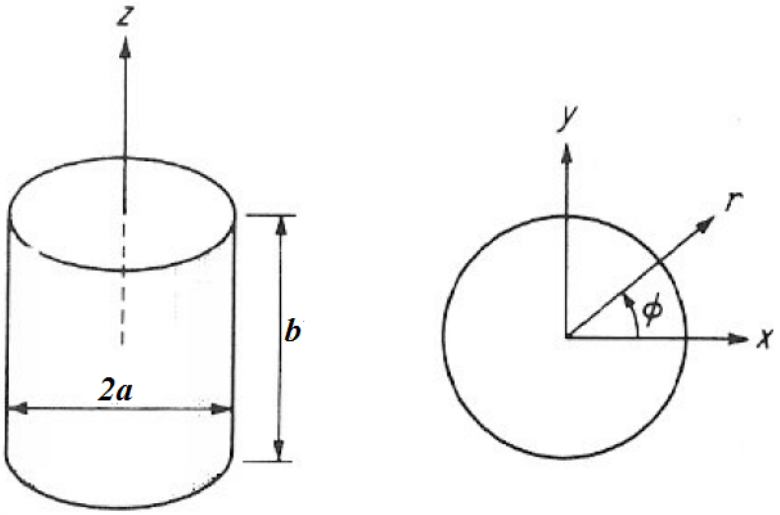

Figure 3.3: Cylindrical resonant cavity.

The resonant fields and frequencies can be derived from the solutions for the corresponding waveguides with appropriate boundary conditions. Considering cylindrical coordinates (ρ, ϕ, z), the transverse electric field $(E_{\rho,\phi})$ for the mode $TE_{n,m}$ $TM_{n,m}$ of a circular guide can be written as: [55]

$$E_t(\rho, \phi, z) = e(\rho, \phi)[A^+ e^{-jB_{n.m}z} + A^- e^{jB_{n,m}z}] \tag{3.7}$$

where $e(\rho, \phi)$ is the transversal variation of the way, while A^+ and A^- are arbitrary amplitudes of the forward and backward waves.

The propagation constant, for the two types of modes, are:

$$\begin{aligned} \beta_{n,m}^{TE} &= \sqrt{k^2 - (\frac{\dot{J}_{n,m}}{a})^2} \\ \beta_{n,m}^{TM} &= \sqrt{k^2 - (\frac{J_{n,m}}{a})^2} \end{aligned} \tag{3.8}$$

where $k = \sqrt{\mu\epsilon}$, $J_{n,m}$ and $\dot{J}_{n,m}$ are the zeros of the Bessel function of the first kind of order n and its derivative.
Due to the presence of the two metal plates, it is now necessary to impose the cancellation of the tangential electric field $E_t = 0$ for z = 0 and z = b, obtaining:

$$\begin{aligned} A^+ &= -A^- \\ A^+ \sin(\beta_{n,m})b &= 0 \end{aligned}$$

from which we get

$$\beta_{n,m} b = l\pi$$

with $l = 0, 1, 2, ...$ for the TM modes and $l = 1, 2, 3, ...$ for the TE modes.
The resonance frequencies for the cylindrical cavity are therefore given by:

$$\begin{aligned} f_{n,m,l}^{TE} &= \frac{c}{2\pi\sqrt{\mu_r\epsilon_r}}\sqrt{(\frac{\dot{J}_{n,m}}{a})^2 + (\frac{l\pi}{b})^2} \, (l \neq 0) \\ f_{n,m,l}^{TM} &= \frac{c}{2\pi\sqrt{\mu_r\epsilon_r}}\sqrt{(\frac{J_{n,m}}{a})^2 + (\frac{l\pi}{b})^2} \end{aligned} \tag{3.9}$$

These equations don't have a superior limit, so the number of modes is infinite but discrete and as the resonant frequency increases the superposition of the frequencies increases. Complete information on the relationship between the geometry and the allowed frequencies can be deduced from the so-called **mode chart**, shown in figure 3.4.

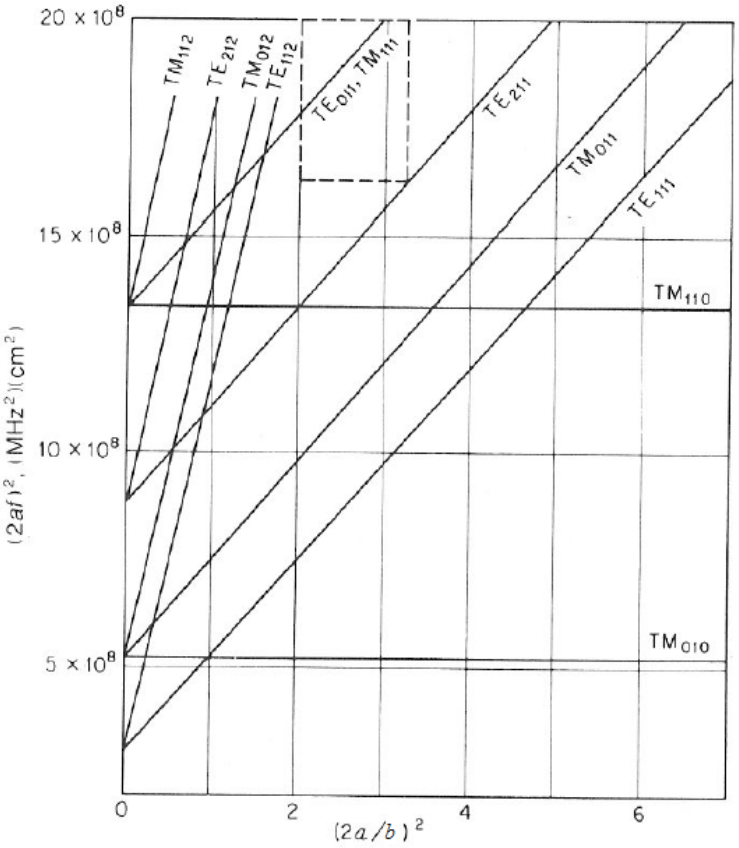

Figure 3.4: Modes chart for the cylindrical cavities.

It expresses the following quantity, obtained by multiplying equation 3.9 by $2a$ and squaring, as a function of the cavity's geometry:

$$(2\,a\,f_{n,m,l})^2 = (\frac{c}{2\,\pi})^2 \frac{1}{\mu_r \epsilon_r}[(\frac{\chi_{n,m}}{a})^2 + (\frac{l\,\pi}{b})^2] \tag{3.10}$$

where $\chi_{n,m} = \dot{J}_{n,m}$ for the TE modes; while $\chi_{n,m} = J_{n,m}$ for the TM modes. For low values of the ratio $\frac{2a}{b}$, the fundamental mode is the $TE_{1,1,1}$, while for $\frac{2a}{b}$ higher than 1, the fundamental mode is the $TM_{0,1,0}$ [56].

Chapter 4

CAESAR and IRIS Simulations

4.1 Introduction

The performance of an ECR source depends, basically, on the ability to couple the electromagnetic power to plasma electrons, through the resonant process. As described in chapter 2, the ECR resonance occurs at those points where the electron's cyclotron frequency is equal to the microwave frequency: considering the particular magnetic configuration applied, this condition is verified on specific points of the plasma chamber, forming typically an egg-shaped surface. More, the theory tells us that this resonant process takes place between the electrons' Larmor motion and a right-handed circularly polarized wave propagating parallel to the confining magnetic field: for this reason, the points of the resonant surface where the energy transfer could be maximum are those around the plasma chamber axis. This means that an optimum energy transfer to plasma electrons pass not only through a good coupling between the microwave injection line and the plasma chamber but also the creation of an electromagnetic field with a specific distribution, in particular optimized on the resonant surface. The cylindrical symmetry makes it often difficult to optimize the field on this surface and the fields could show asymmetries, or eventually minima on the plasma chamber axis. This is

reflected in the spatial and energy distribution of the electrons, possibly leading to low performances and poor beam quality (for example the formation of hollow beams). The approach proposed in this thesis concerns the optimization of the electromagnetic field acting on the plasma chamber geometry: in particular, the aim is to break the cylindrical symmetry by implementing an innovative design. The physic case used to verify the effectiveness of the proposed new design is the ECR source CAESAR, installed at the INFN-LNS [11] [12]: the idea is to give the plasma chamber a shape resembling the one given to the plasma by the confining magnetic field, shown in figure 4.1 for the CAESAR source as obtained from electrons' dynamics simulations.

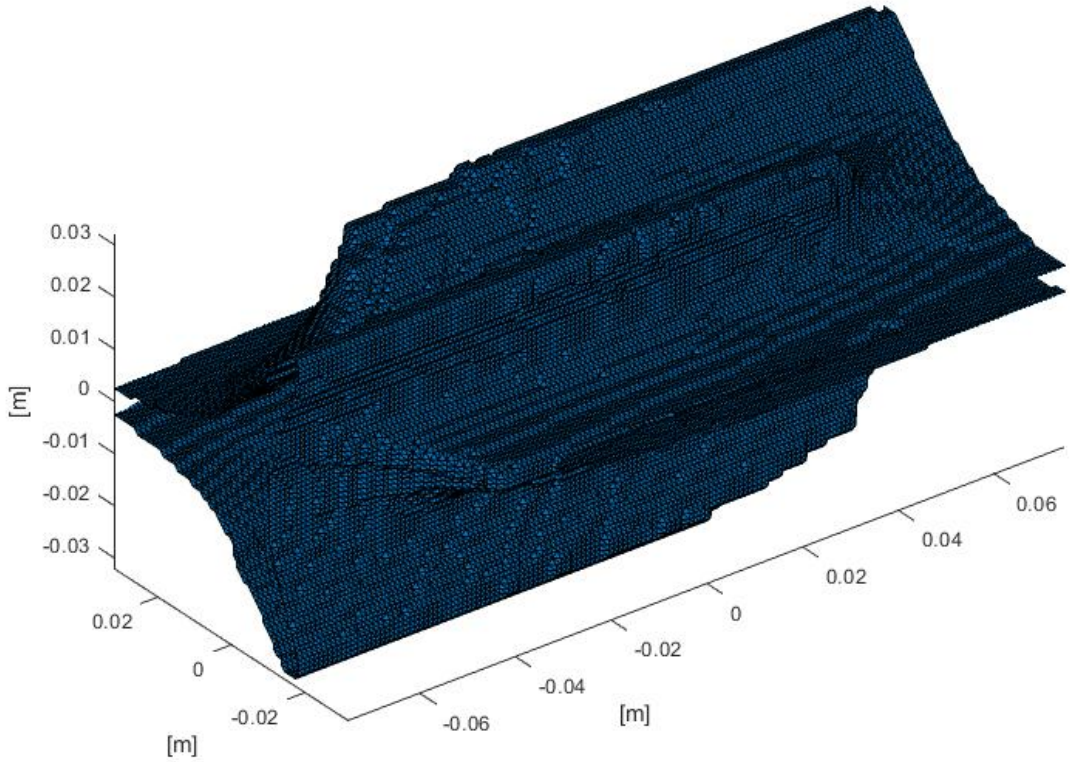

Figure 4.1: The shape impressed by the magnetic field to the plasma in the CAESAR source.

Based on the shape of the previous figure, a first version of the new design has been produced and studied, called IRIS-OLD (the reason for this name will be clarified later in this section), whose geometry is shown in figure 4.2.

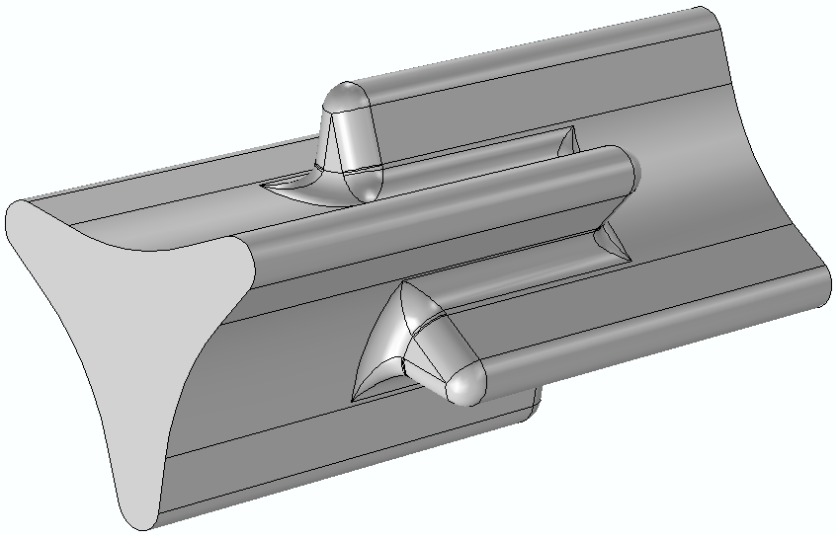

Figure 4.2: Model of the IRIS-OLD geometry.

To explore different possibilities for the microwaves' injection, the electromagnetic field produced was initially verified by varying the angle between the input waveguide and the plasma chamber axis from 0° (usual position) to 90° (as in the case of the ECR-based charge breeder of the SPES project [26]). At the end of this verification, an angle of 45° was found as the one giving the most promising results and is the only one considered for the simulations described in the following. To obtain a plasma chamber that could have been machined in a real piece, the initial design IRIS-OLD evolved in a new one, called IRIS-NEW. The microwave injection system was initially kept the same, but later an innovative system based on a slotted and twisted waveguide was proposed, to further optimize the generated electromagnetic field.
This chapter describes the electromagnetic study, performed through numerical simulations, of the abovementioned geometries. All the simulations have been carried out by applying the procedure described below:

1. Calculation of the resonant modes of ideal vacuum-filled cavities in a narrow frequency range around the CAESAR operating frequency, using the CST eigenmode solver [57];

2. Calculation of the resonant modes of real vacuum-filled cavities for 200 frequencies in a wider range (14-16 GHz), evaluating for each one the Scattering

coefficients. All the calculations have been carried out with COMSOL MultiPhysics in the frequency-domain [58].

3. The same simulations described above but including the presence of a plasma through its 3D dielectric tensor and evaluating the power absorbed.

The approach will be applied, in sequence, to the conventional CAESAR geometry, IRIS-OLD and IRIS-NEW (with both regular and slotted waveguides); then a comparison will follow.

4.2 CAESAR cylindrical plasma chamber

The ion source CAESAR used to benchmark the improvements brought by the proposed new geometry is a second-generation ECR source usually operating at 14.5 GHz. Its plasma chamber has a conventional cylindrical shape, with length and diameter 150 mm and 63.5 mm respectively. Microwaves are injected through a rectangular WR62 waveguide, parallel to the plasma chamber axis (see sketch 4.3).

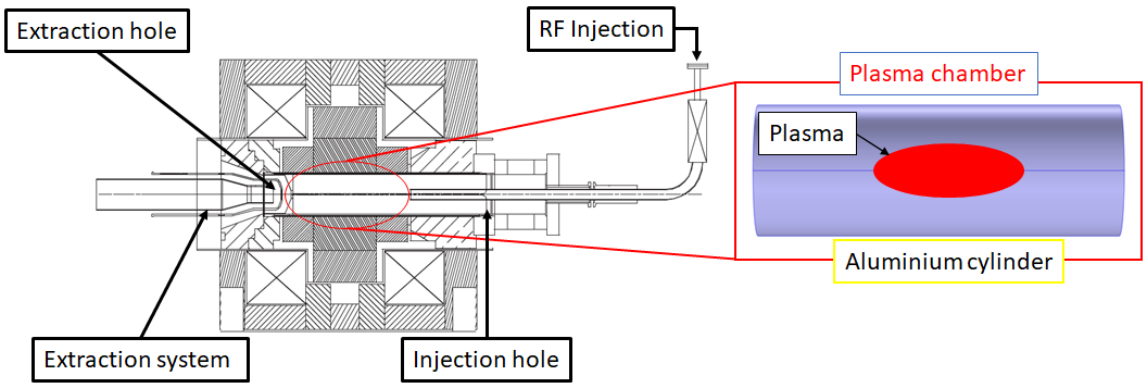

Figure 4.3: Sketch of the CAESAR ECR Ion Source.

This section will describe the results of the calculations, using the procedure described in the introduction, applied to the CAESAR cylindrical plasma chamber.

4.2.1 Eigenmode solver

As the first step of an electromagnetic analysis of a resonant cavity, it is required to calculate its resonant modes, by using the eigenmode solver of the CST Microwave Studio (MWS): it calculates a finite number of modal field distributions in a closed structure. The eigenmode analysis does not require the definition of excitation port: the solver imposes field amplitudes to the modes such that each mode contains a total energy of 1 Joule. This kind of evaluation is a good starting point to have an idea of the frequencies and the kind of modes (if TE or TM) allowed in the cavity. By using eq. 3.9 it is also possible to calculate them analytically using the Bessel functions and their first derivative: the results will be used for comparison with those provided by CST, which is not only much faster but give also an immediate picture of the electromagnetic field distribution. A crucial parameter that had to be determined for all the simulations described in this chapter has been the mesh spacing. A useful approach usually consists in starting with a rough value and then reducing it until the simulated frequencies approximate those calculated analytically. A limit to this approach could be the computational time, which should be kept at a reasonable level. The analysis was focused on a narrow frequency range (14.45 GHz - 14.55 GHz) around the CAESAR operating frequency of 14.5 GHz, where analytical formulas predict 8 resonant modes, illustrated in figure 4.4.

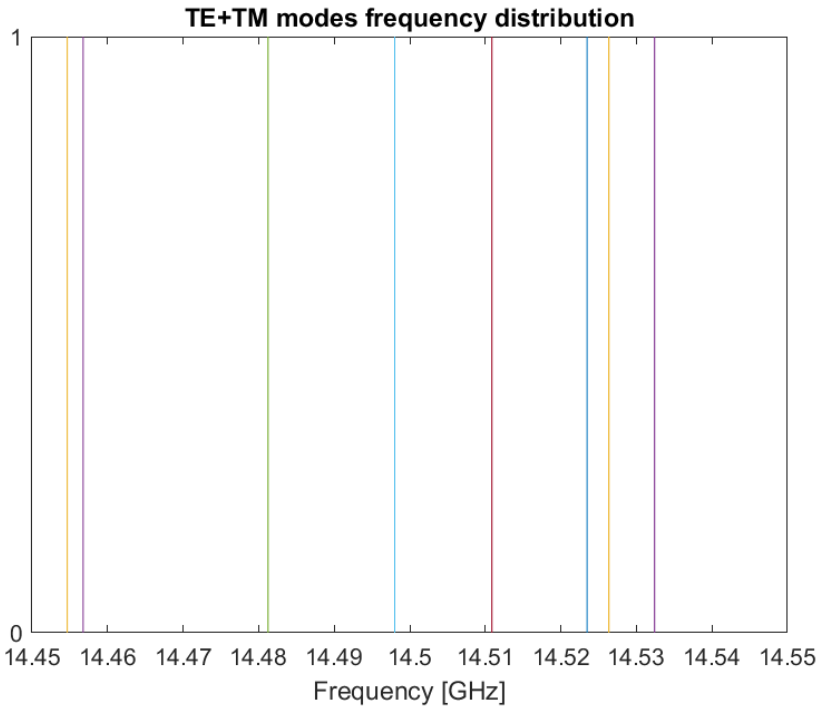

Figure 4.4: Resonant modes of the CAESAR cylindrical plasma chamber in the range 14.45 GHz - 14.55 GHz.

Simulations then started and the mesh size was reduced until the difference between simulated and calculated frequencies was less than 0.002%: it happened for a mesh spacing equal to $\frac{1}{6}$ of the wavelength in vacuum (figure 4.5).

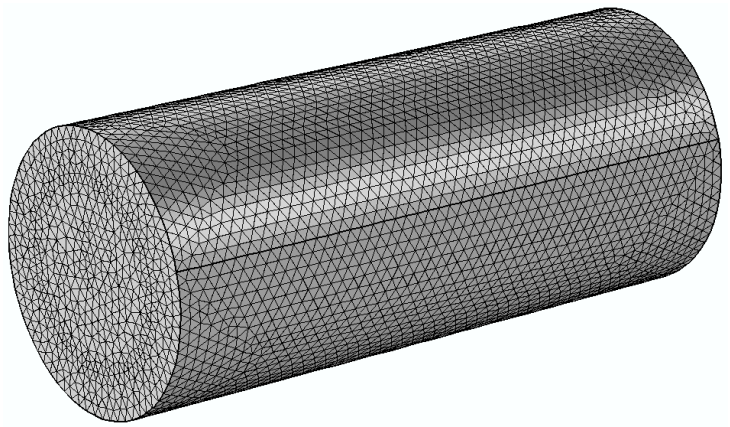

Figure 4.5: Mesh discretization of CAESAR geometry.

Table 4.1 shows the comparison between calculated and simulated frequencies for this mesh spacing: it comes out that the closest mode to the operating frequency of the CAESAR source is the $TE_{8,1,0}$, with a frequency of 14.498 GHz.

Table 4.1: Comparison between simulation and analytics values for the modes in the range 14.45 - 14.55 GHz

	Mode	Analytic Frequency [GHz]	Simulation Frequency [GHz]
1	$TM_{2,2,7}$	14.454662	14.454842
2	$TE_{3,1,8}$	14.456765	14.456576
3	$TM_{5,1,6}$	14.481238	14.481390
4	$TE_{8,1,0}$	14.498006	14.497935
5	$TE_{4,2,4}$	14.510868	14.511032
6	$TM_{4,1,9}$	14.523471	14.523704
7	$TM_{1,2,10}$	14.526357	14.526567
8	$TM_{8,1,1}$	14.532405	14.532255

For the sake of completeness, figure 4.6 shows the electric field distribution of this mode in the yz plane at x = 0 mm (z is the plasma chamber axis).

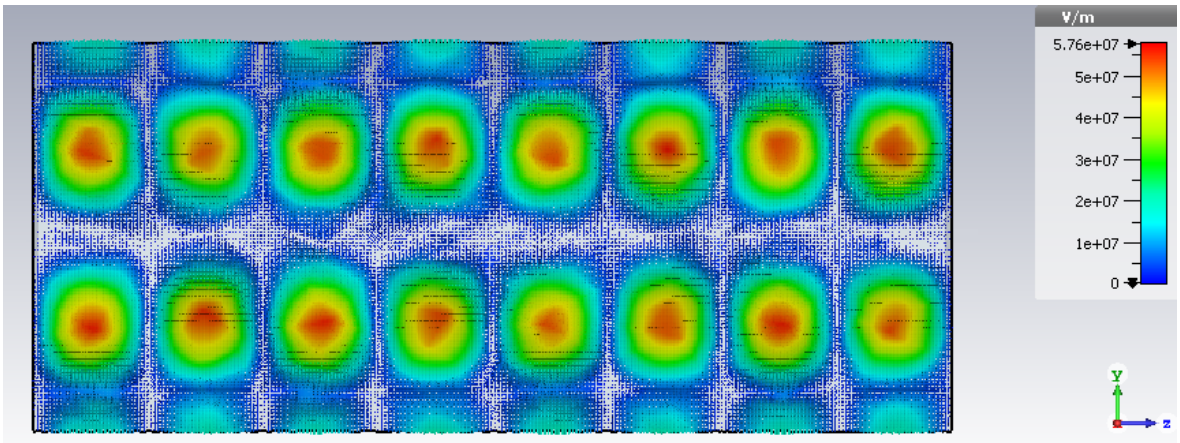

Figure 4.6: Electric field distribution at 14.498 GHz of the $TE_{8,1,0}$ mode for the CAESAR resonant cavity.

4.2.2 Frequency domain solver

The following step consisted in the implementation of the real plasma chamber, by employing COMSOL Multiphysics and its so-called frequency-domain analysis including waveguide ports. The mesh size was kept the same as in the eigenmode simulations: figure 4.7 shows the COMSOL Multiphysics workspace with the simulated structure. The frequency-domain solver takes into account the materials constituting the resonant cavity, as well as eventual holes present in the geometry. While the eigenmode solver searches for resonant modes, the frequency domain solver simulates specific frequencies.

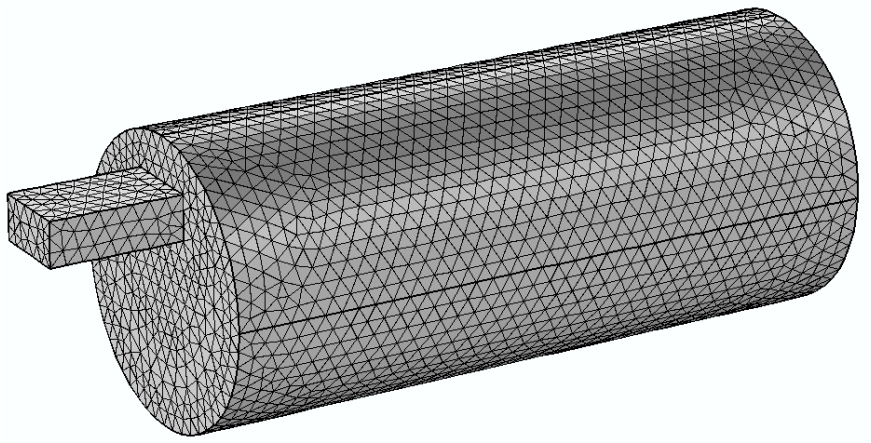

Figure 4.7: Mesh discretization of CAESAR with the longitudinal waveguide injection system.

The excitation signal to the cavity is supplied through the input WR62 waveguide using the fundamental mode $TE_{1,0}$. The plasma chamber is made in aluminium ($\sigma = 3.77 * 10^7$ $[S/m]$). The program provides the Scattering parameters in the frequency domain, defined as the ratio between the signal output and input. To expand the range of frequencies possibly of interest for the implementation of the new geometry, the calculations were made in the range 14 GHz and 16 GHz, simulating 200 frequencies separated by a $\delta_f = 10MHz$ and with an input power P = 100 W. As an example, the figure 4.8 shows the distribution of the E-field calculated at 14.50 GHz in 10 logarithmic scales: it can be observed that the maxima of the electric field are mainly located in the off-axis region, far from the points where the ECR resonance produces the maximum energy transfer.

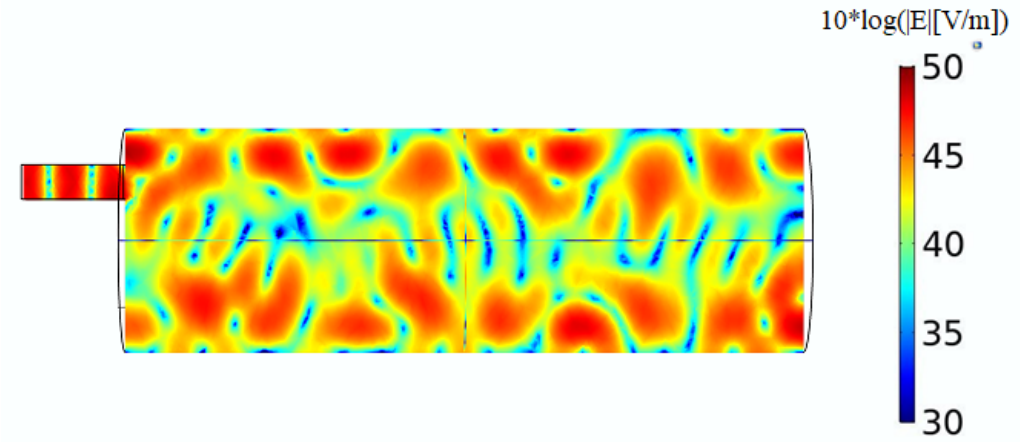

Figure 4.8: Electric field distribution, in 10 logarithmic scales, calculated at 14.50 GHz for the CAESAR plasma chamber with the longitudinal waveguide injection system.

Generally, a perfect coupling between the waveguide and a cavity takes place when the first element of the coupler scattering matrix (S11) is equal to zero on the linear scale, while it approaches minus infinity on the decibel scale. Figure 4.9 shows the coefficient S11 as a function of the frequency in the simulated range.

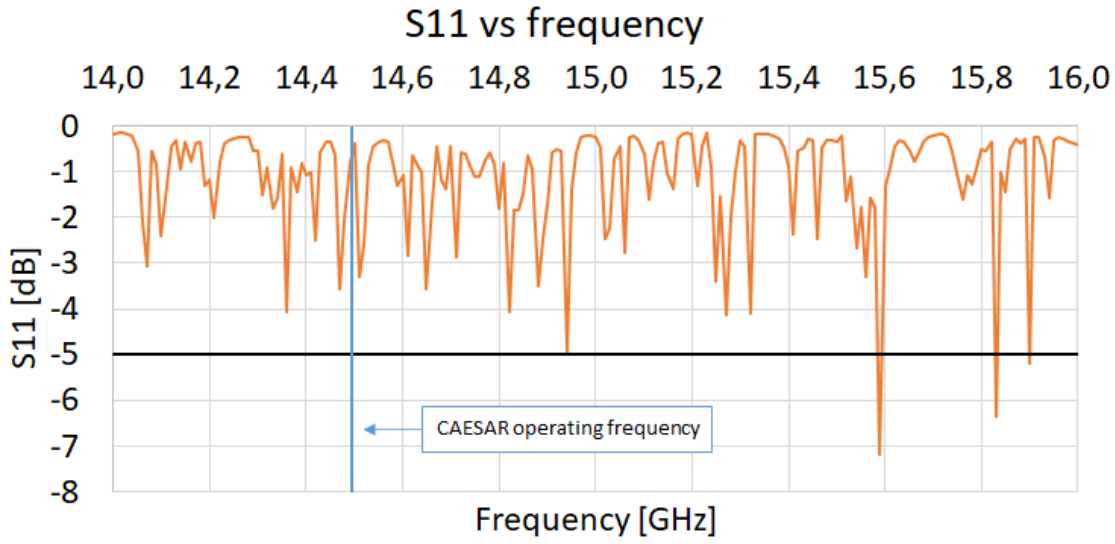

Figure 4.9: Coefficient of reflection S11, calculated in the range 14 GHz - 16 GHz, for the CAESAR resonant cavity with the longitudinal waveguide injection system.

By considering -5 dB as the upper limit to have a reasonably good matching (about 30% of the power is reflected), figure 4.9 shows that only three frequencies have a lower value and the CAESAR operative frequency is not among them. Clearly, the simulations showed up to now cannot be considered realistic, because the presence of a magnetized plasma that undergoes the ECR resonance dramatically change the electric field distribution and amplitude compared to the vacuum-filled case. So, a plasma was implemented through its fully-3D dielectric tensor, computed by MatLab [59] for each mesh point given by COMSOM and having a structure following the plasmoid/halo scheme, that is a dense plasma enclosed inside the resonance surface (the plasmoid), with a density $n_{plasmoid} = 2.5*10^{17}\ m^{-3}$, and a rarified halo outside with $n_{halo} = \frac{n_{plasmoid}}{100}$. Due to the shortening of the wavelength approaching the ECR resonance, the mesh size used was not uniform, reaching $\frac{\lambda_0}{10}$ around the resonance surface and $\frac{\lambda_0}{6}$ outside, where λ_0 is the wavelength in vacuum. Figure 4.10 shows the calculated electric field distribution, in 10 logarithmic scales, at 14.50 GHz:

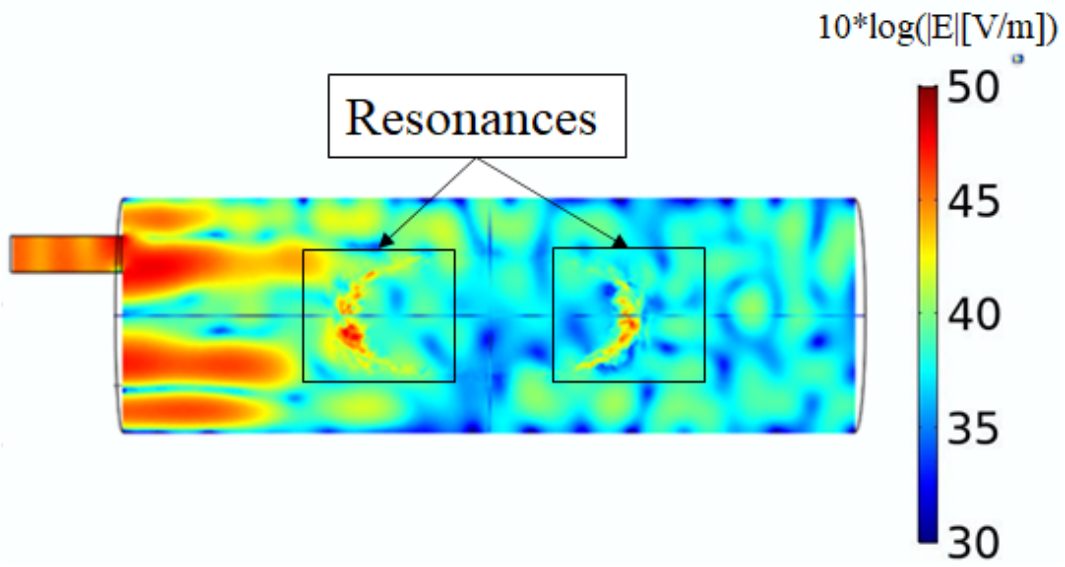

Figure 4.10: Electric field distribution, in 10 logarithmic scales, calculated at 14.50 GHz for the CAESAR with the longitudinal waveguide injection system, including a magnetized plasma.

the effect due to the presence of the plasma is clearly visible, with two zones

of intensification of the electric field due to the ECR resonance.
To understand the changes in the coupling between the waveguide and the cavity due to the presence of a magnetized plasma, it is necessary to analyse again the reflection coefficient S11 for all the resonant frequencies, shown in figure 4.11.

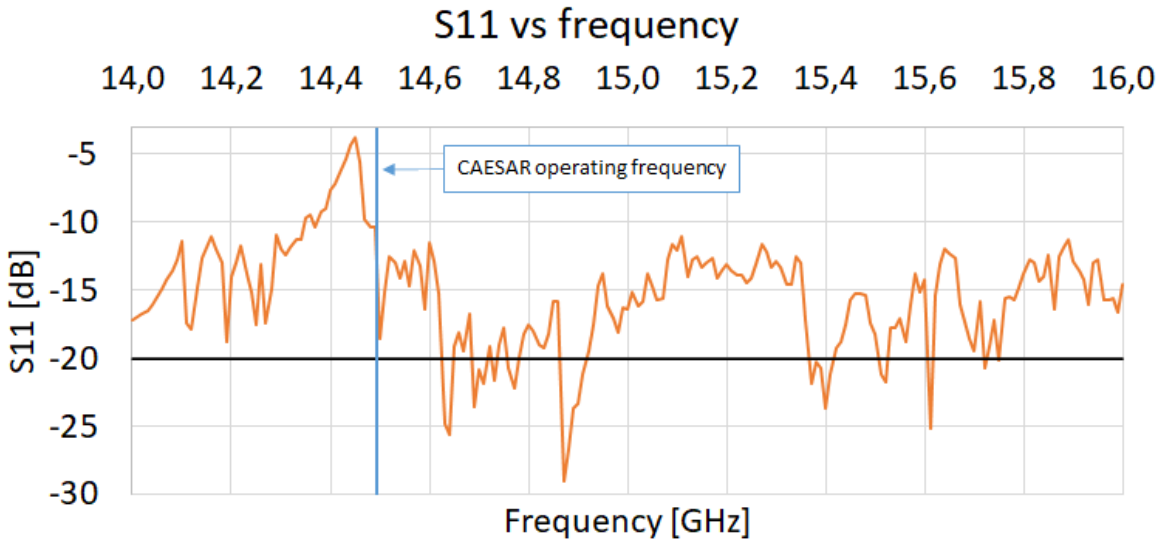

Figure 4.11: Coefficient of reflection S11, calculated in the range 14 GHz - 16 GHz, for the CAESAR resonant cavity with a longitudinal waveguide injection system, including a magnetized plasma.

In comparison with the results obtained with the vacuum-filled cavity, the presence of the plasma is such that all the frequencies show now a coupling better than $-5dB$: in particular, there are entire sub-ranges ($14.6GHz - 14.9GHz$ for example) where the coupling is better than $-20dB$, that is only 1% of the power is reflected.
To complete the analysis it is interesting to look at a complementary parameter, the overall power absorption: it has been calculated through the volume integral of the total dissipated power inside the chamber. The results are shown in figure 4.12: it can be seen that the CAESAR geometry shows a good power absorption, except for a region exactly around its operating frequency, meaning that the performances could take benefit of a geometry's optimization.

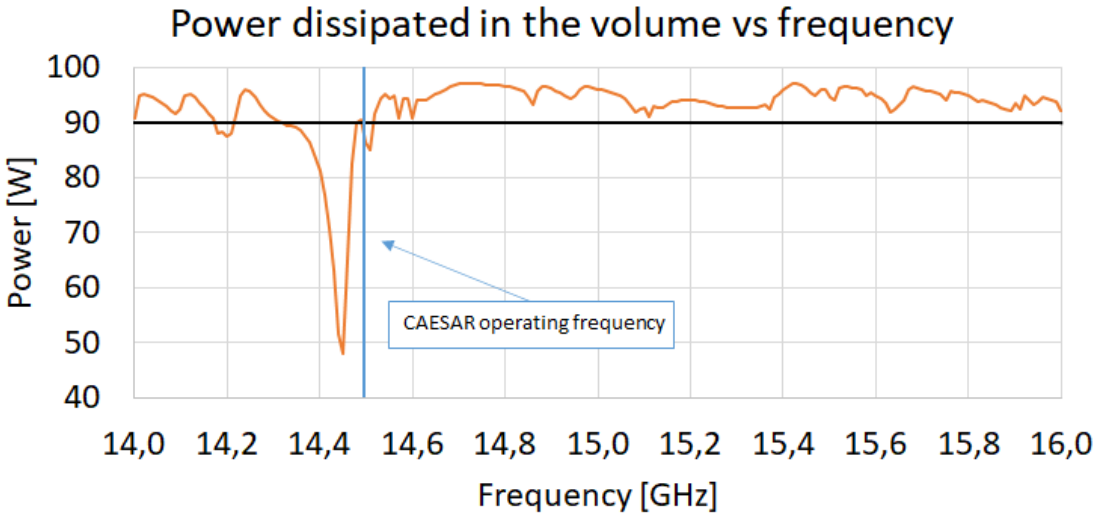

Figure 4.12: Power absorbed by the plasma in the CAESAR plasma chamber with the longitudinal waveguide injection system.

4.3 IRIS-OLD plasma chamber

The IRIS-OLD geometry consists of two "three-branches" stars rotated of 60° one with respect to the other, that start from the extremities of the plasma chamber and overlap in the centre (see figure 4.2). It has the same length as the conventional CAESAR, as well as the maximum transversal dimension. This section will describe the results of the calculations carried out on this first version of the new geometry, by applying the same procedure described previously.

4.3.1 Eigenmode solver

Due to the peculiar IRIS-OLD' geometry, it has not been possible to distribute the mesh as in the case of CAESAR, because it has been necessary to follow its irregular surface (visible in figure 4.13). In this case, the mesh has been defined with a tetrahedral shape, whose parameters are: maximum size $\frac{\lambda_0}{6}$, minimum size $2 * 10^{-5}\, m$, maximum growth ratio for elements (to determine the maximum rate at which the element size can grow from a region with small elements to a region with larger elements.) 1.3 and a factor of curvature 0.2.

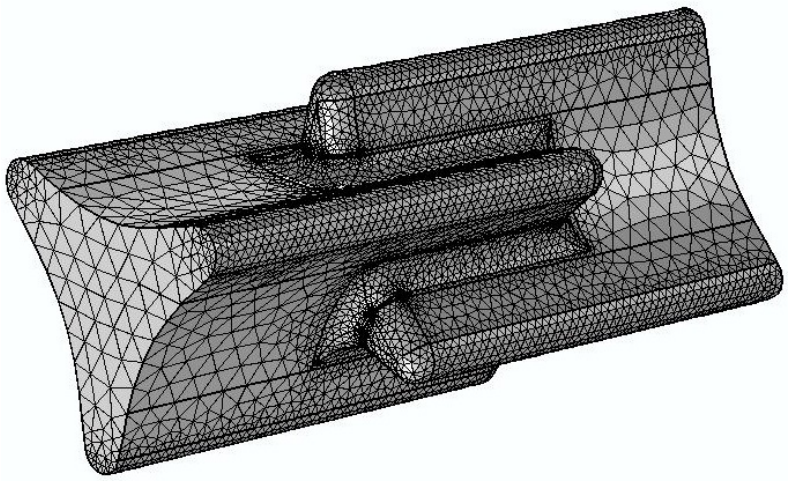

Figure 4.13: Mesh discretization of IRIS-OLD geometry.

For this kind of geometry, it is not possible to evaluate TE or TM modes: the only possibility is a comparison of the electromagnetic field distribution for two frequencies very close to each other. As it has been done previously, the analysis started in the small range 14.45 GHz - 14.55 GHz: the solver found only 3 frequencies, 14.459 GHz, 14.460 GHz and 14.497 GHz. Figure 4.14 shows the one most similar to the $TE_{8,1,0}$ that shifts of 38 MHz respect to the CAESAR cavity.

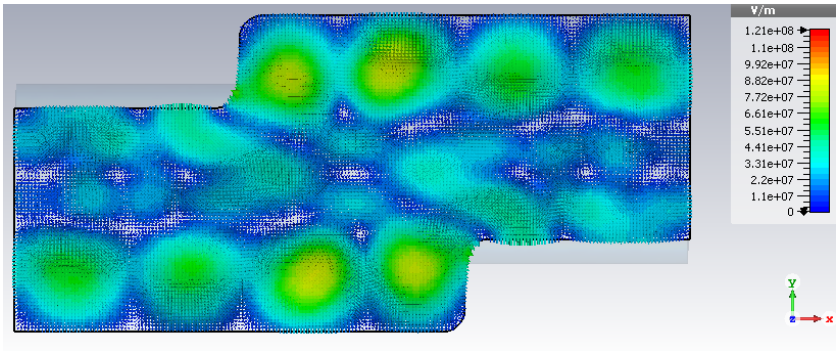

Figure 4.14: Electric field distribution at 14.460 GHz of a mode similar to the $TE_{8,1,0}$ for the IRIS-OLD resonant cavity.

The electromagnetic field distribution of the frequency closest to the CAESAR operating frequency is shown in figure 4.15: here again, the electric field maxima are located in the off-axis region.

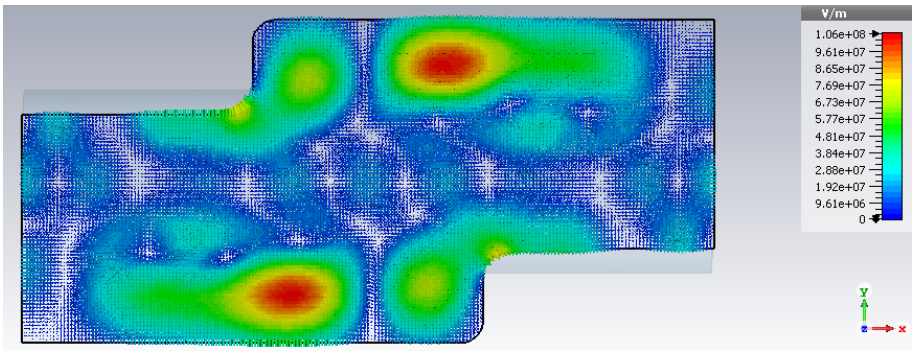

Figure 4.15: Electric field distribution at 14.497 GHz for the IRIS-OLD resonant cavity.

4.3.2 Frequency domain solver

As we did for CAESAR, we proceeded to analyse the cavity in the frequency domain, considering the waveguide input tilted of 45°: the geometry is shown in figure 4.16.

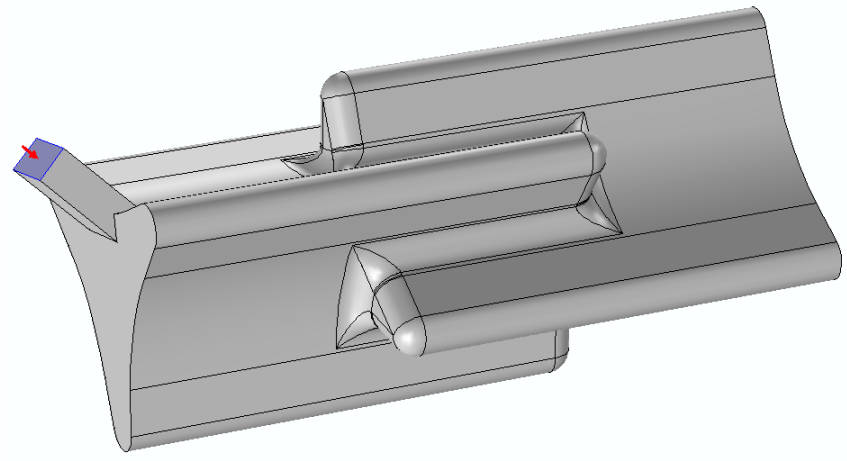

Figure 4.16: Model of the IRIS-OLD geometry with the microwave injection tilted 45° with respect to the longitudinal axis.

As a first step, the electromagnetic field was calculated at the CAESAR operative frequency (14.5 GHz): figure 4.17 shows the results. Compared to the eigenmode solver, the zones with the most intense field are wider, but still located off-axis.

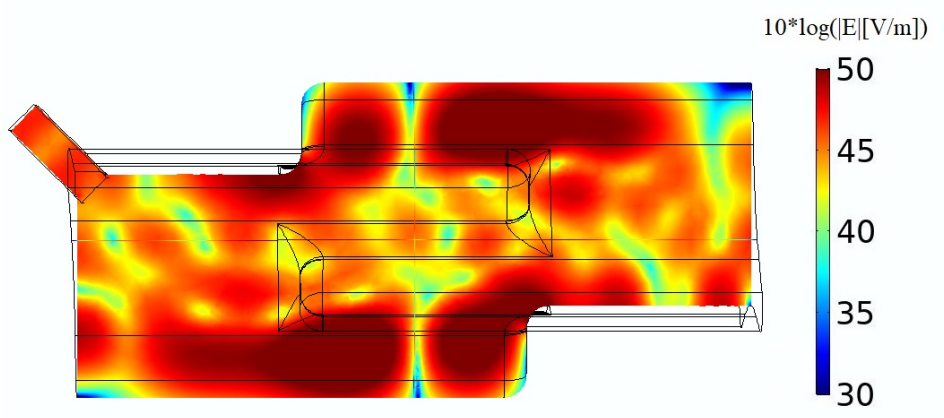

Figure 4.17: Electric field distribution, in 10 logarithmic scales, calculated at 14.50 GHz for the IRIS-OLD plasma chamber with the microwave injection tilted 45° with respect to the longitudinal axis.

The simulations continued with the analysis of the range 14 GHz - 16 GHz, keeping the same parameter as in the case of the CAESAR geometry. Figure 4.18 shows the coefficient S11 as a function of the frequency: it can be seen that now the frequencies showing a matching better than -5dB increased from three to thirteen, including the CAESAR operating frequency.

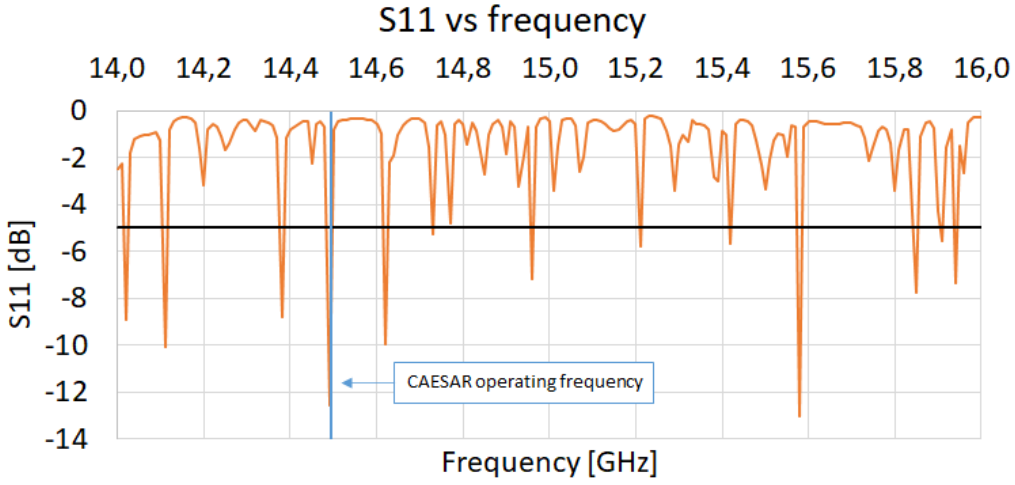

Figure 4.18: Coefficient of reflection S11, calculated in the range 14 GHz - 16 GHz, for the IRIS-OLD plasma chamber with the microwave injection tilted 45° with respect to the longitudinal axis.

Finally, the plasma was implemented with the same structure and approach described previously: figure 4.19 shows the calculated electric field distribution, in 10 logarithmic scales, at 14.50 GHz.

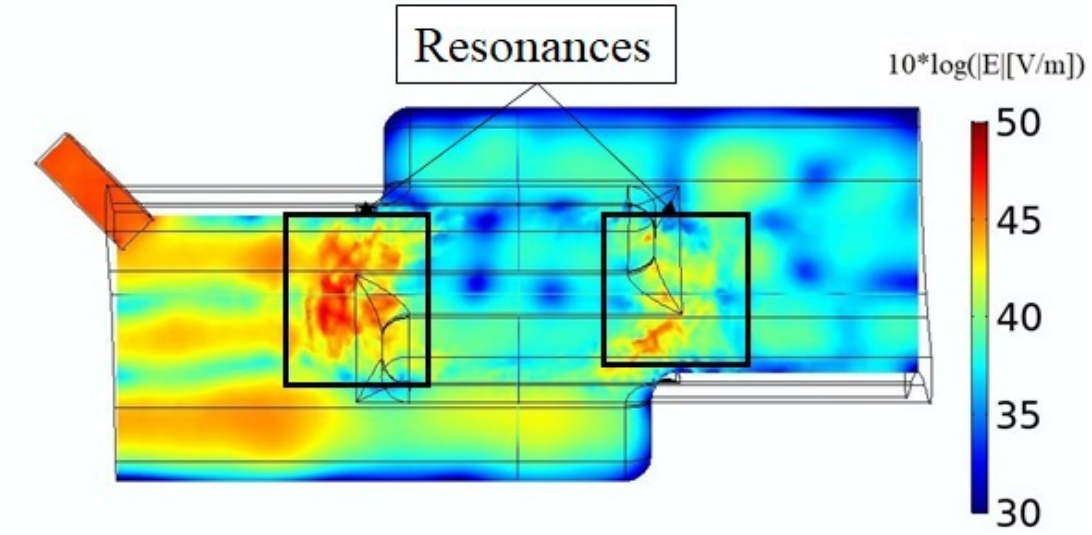

Figure 4.19: Electric field distribution, in 10 logarithmic scales, calculated at 14.50 GHz for the IRIS-OLD with the microwave injection tilted 45° with respect to the longitudinal axis, including a magnetized plasma.

Again, the power absorption at the resonances around the plasma chamber axis is visible, but now with a much wider area.
As it has been done previously, let us now see how the coupling between the waveguide and the resonant cavity changed due to the plasma.

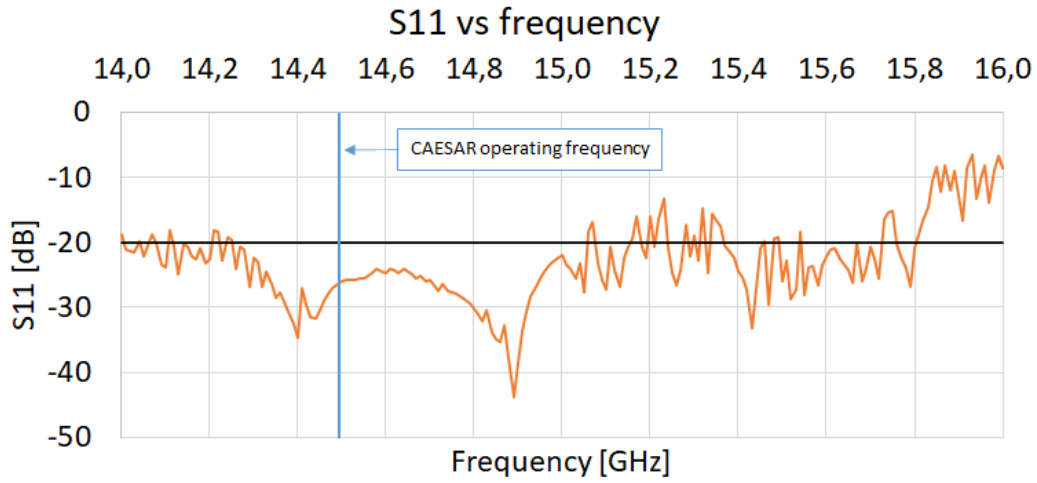

Figure 4.20: Coefficient of reflection S11, calculated in the range 14 GHz - 16 GHz, for the IRIS-OLD plasma chamber with the microwave injection tilted 45° with respect to the longitudinal axis, including a magnetized plasma.

Figure 4.20 shows that almost the entire frequency range has the S11 coefficient under -20 dB, except for the highest frequencies where it basically never exceeds -10 dB. In particular, at 14.50 GHz it is equal to -28.05 dB.
Figure 4.21 shows the power absorption by the plasma in the same frequency range, with values higher than 90 W between 14.2 GHz and 15.5 GHz.

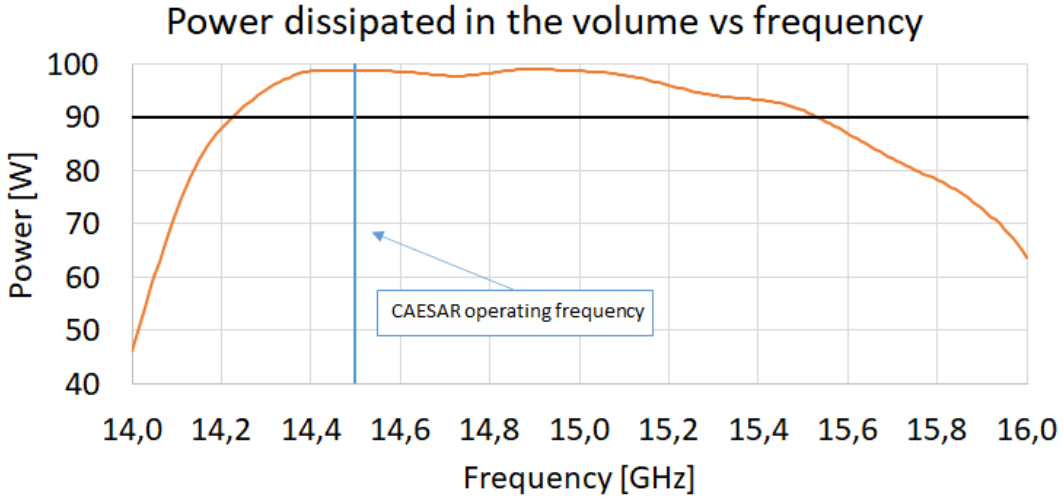

Figure 4.21: Power absorbed by the plasma in the IRIS-OLD plasma chamber with the microwave injection tilted 45° with respect to the longitudinal axis.

4.4 IRIS-NEW plasma chamber

The IRIS-OLD plasma chamber already shows improvements compared to the classic CAESAR one. Unfortunately, this cavity revealed difficult to be machined, due to the numerous surface irregularities. The design was then refined through a sequence of mechanical tapering and smoothing steps, as shown in figure 4.22. At each step, the cavity was checked by numerical simulations of the allowed modes.

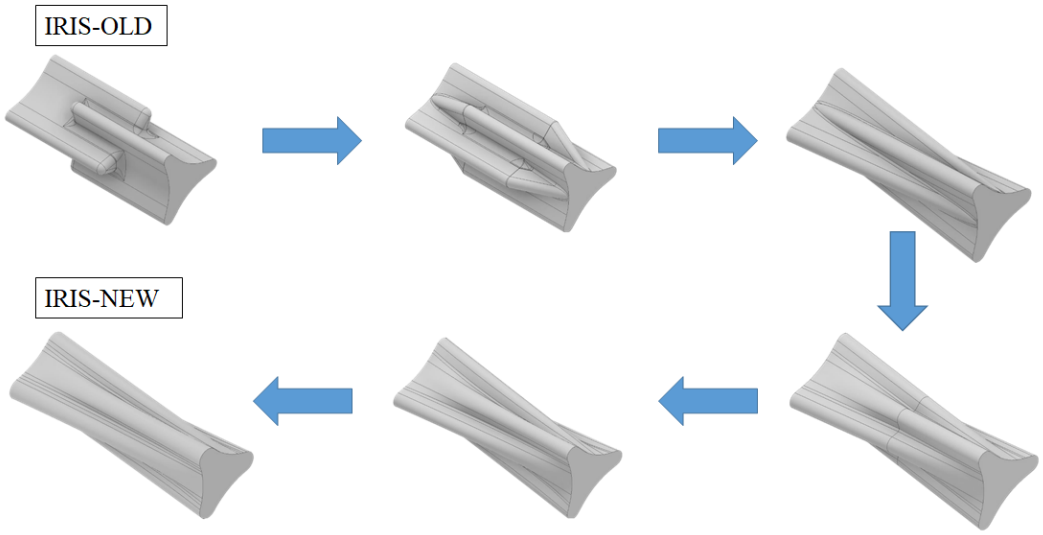

Figure 4.22: The sequence of mechanical tapering and smoothing steps of the IRIS chamber design.

The final geometry was called IRIS-NEW and differs from the previous version for the fact that the three branches of both stars extend all along the plasma chamber (see figure 4.23).

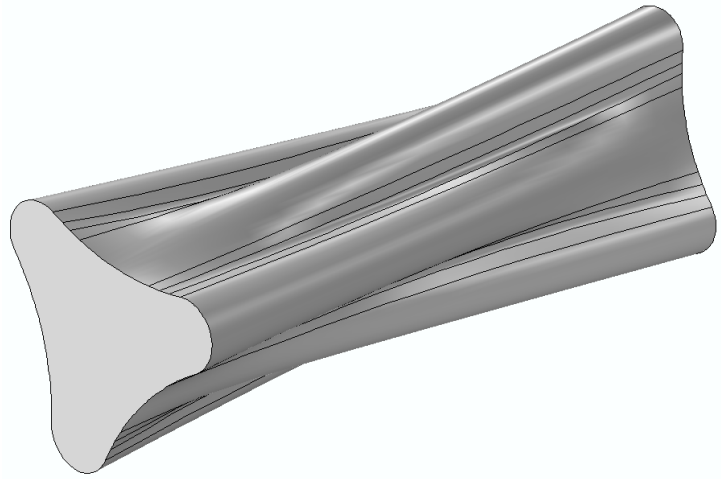

Figure 4.23: Model of the IRIS-NEW goemetry.

The microwave injection system was initially kept the same as IRIS-OLD, but later an innovative system based on a slotted and twisted waveguide was proposed, in order to further optimize the generated electromagnetic field. This section will describe the results of the calculations carried out on the final version of the new IRIS geometry.
Here again we began with the calculation of the resonant modes of the cavity using CST's eigenmode solver. The mesh size shown in figure 4.24, was the same as for the IRIS-OLD case.

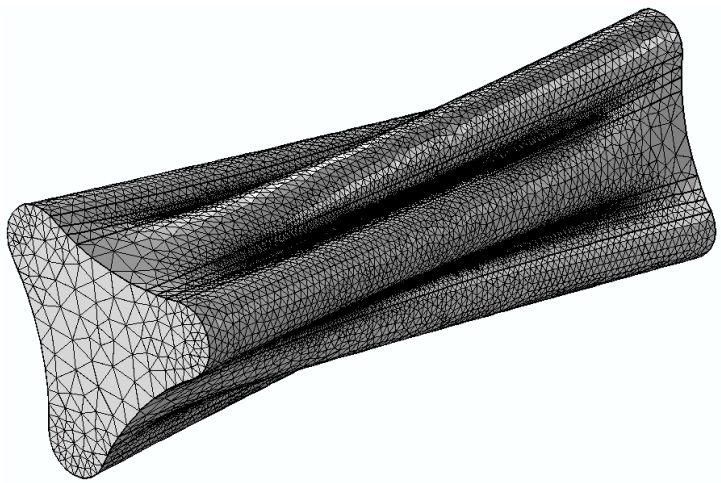

Figure 4.24: Mesh discretization of IRIS-NEW geometry.

The analysis started in the range 14.45 GHz - 14.55 GHz, where only three frequencies have been found: 14.483 GHz, 14.526 GHz and 14.546 GHz. Among them, the resonant mode at 14.483 GHz (see figure 4.25) is the most similar to the mode $TE_{8,1,0}$ of CAESAR but it shifted of 15 MHz.

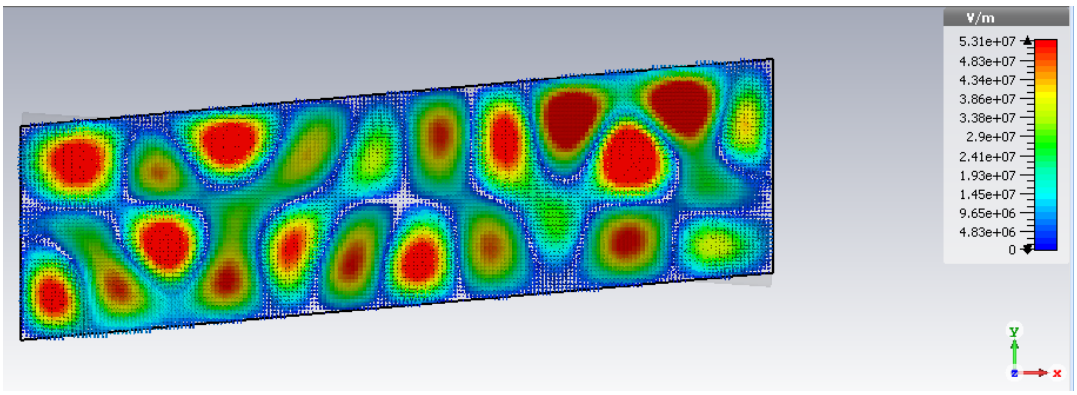

Figure 4.25: Electric field distribution of a mode similar to the $TE_{8,1,0}$ for the IRIS-NEW resonant cavity.

4.4.1 Frequency domain solver with inclined rectangular waveguide

Figure 4.26 shows the same microwave injection system of the IRIS-OLD simulations applied to IRIS-NEW:

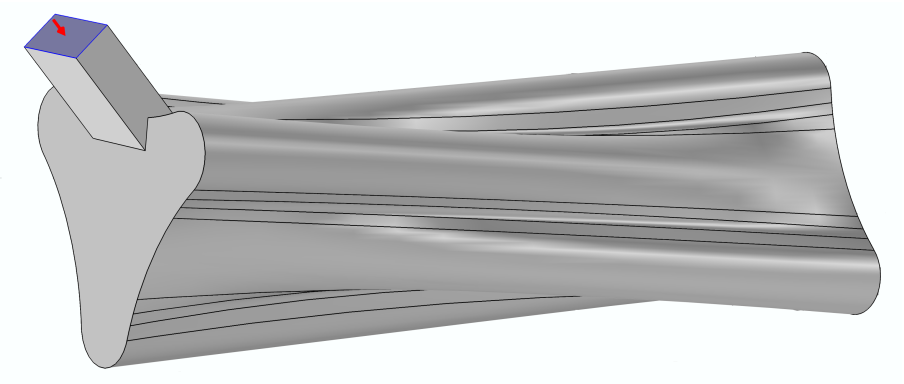

Figure 4.26: Model of the IRIS-NEW geometry with the microwave injection tilted 45° with respect to the longitudinal axis.

the elettromagnetic field calculated at 14.5 GHz is shown in figure 4.27.

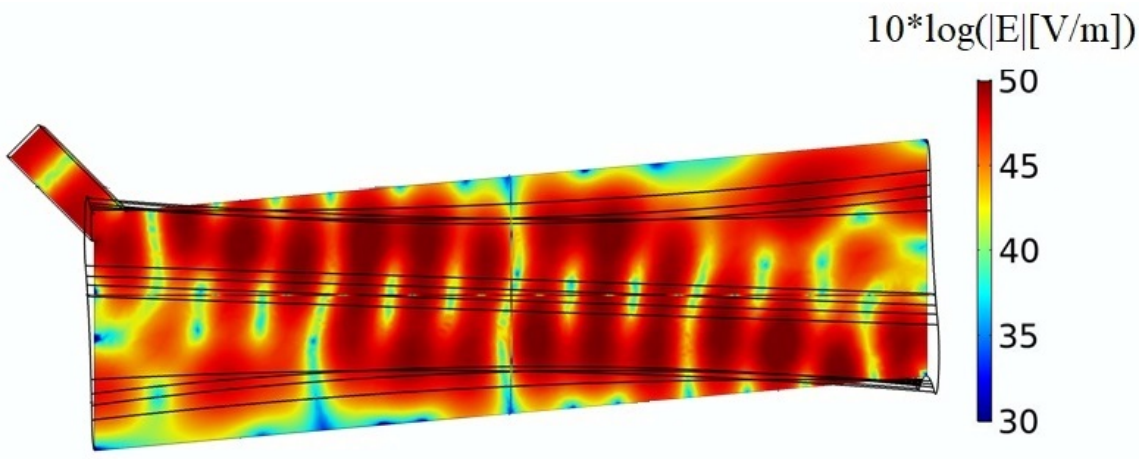

Figure 4.27: Electric field distribution, in 10 logarithmic scales, calculated at 14.50 GHz for the IRIS-NEW chamber with the microwave injection tilted 45° with respect to the longitudinal axis.

The figure shows that the electric field is now more distributed in the centre of the cavity: this is a good indication of the further improvement of the new plasma chamber. Looking at the S11 parameter, we see that it is under -5 dB for 7 resonant modes (see plot 4.28).

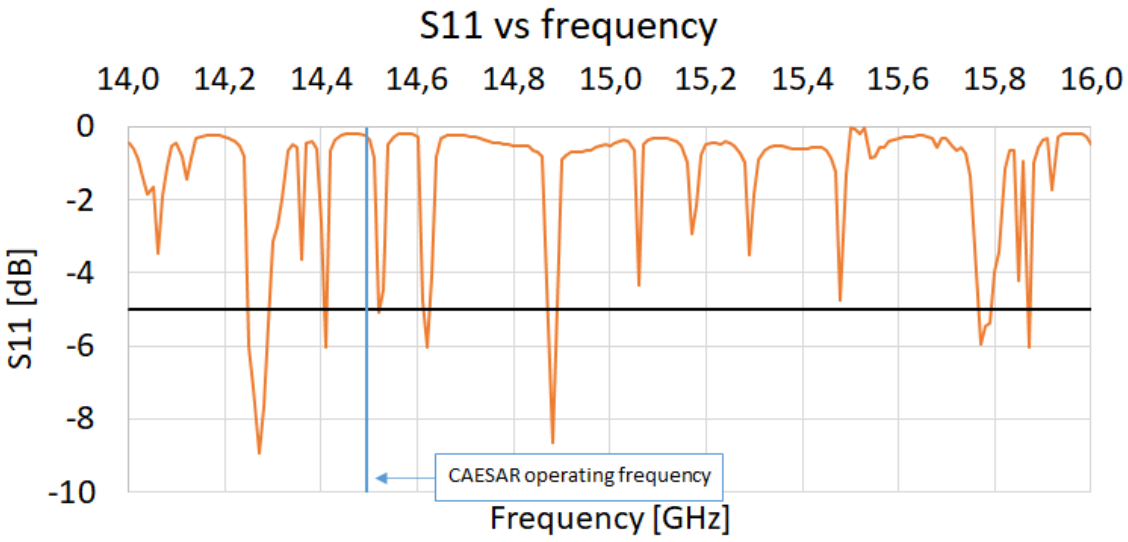

Figure 4.28: Coefficient of reflection S11, calculated in the range 14 GHz - 16 GHz, for the IRIS-NEW plasma chamber with the microwave injection tilted 45° with respect to the longitudinal axis.

As has been done for the CAESAR and IRIS-OLD cavities the same plasma model was included in the simulations. Figure 4.29 shows the electric field distribution at 14.5 GHz: it can be seen that an intense E-field is present at the resonance points around the axis. For IRIS-NEW, all the frequencies in the range 14 GHz - 16 GHz have the S11 coefficient under -20 dB and come down at about -30 dB in the range 14.0 GHz - 14.8 GHz (see plot 4.30). Finally, for what concerns the power absorption, a value around 95% is observed between 14 GHz - 15 GHz, decreasing down to less than 50% at higher frequencies (see plot 4.31).

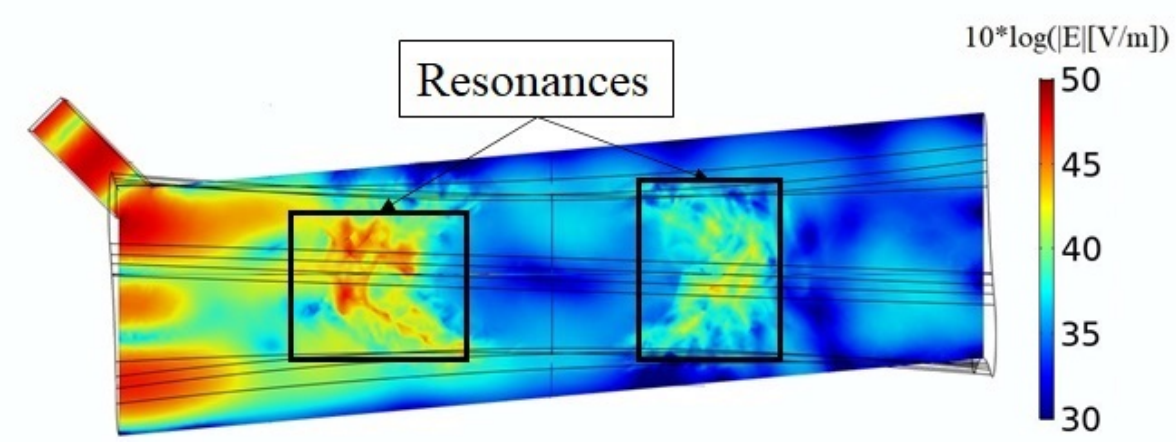

Figure 4.29: Electric field distribution, in 10 logarithmic scales, calculated at 14.50 GHz for the IRIS-NEW with the microwave injection tilted 45° with respect to the longitudinal axis, including a magnetized plasma.

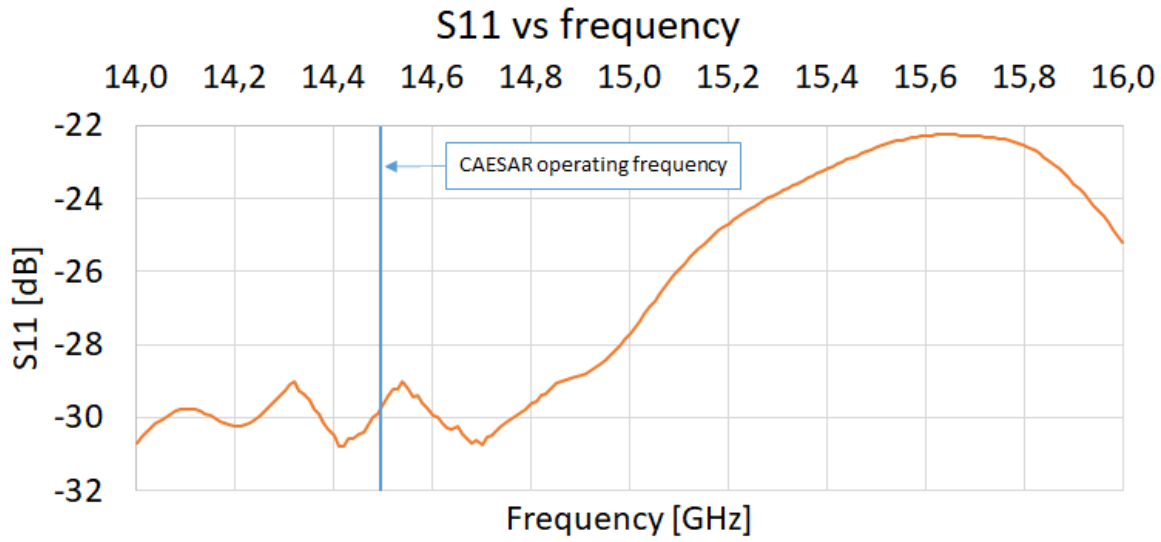

Figure 4.30: Coefficient of reflection S11, calculated in the range 14 GHz - 16 GHz, for the IRIS-NEW plasma chamber with the microwave injection tilted 45° with respect to the longitudinal axis, including a magnetized plasma.

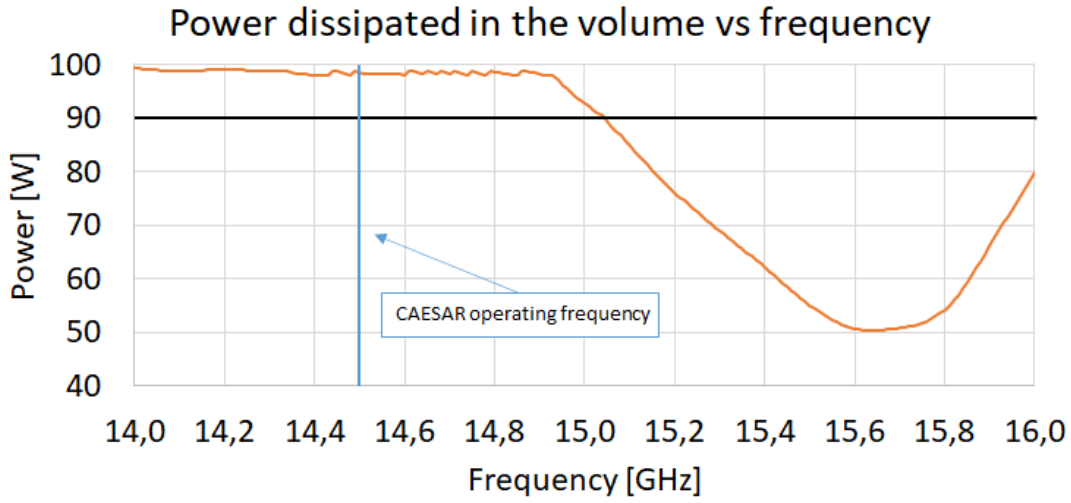

Figure 4.31: Power absorbed by the plasma in the IRIS-NEW plasma chamber with the microwave injection tilted 45° with respect to the longitudinal axis.

4.4.2 Frequency domain solver with slotted/twisted waveguide

The previous sections described the new geometry with an injection system through the classic rectangular waveguide but used in an unconventional way (tilted of 45° respect the longitudinal axis). In this section, the results of the application of an innovative microwave launching system will be presented. The new launching configuration consists of side-coupled slotted waveguides (see figure 4.32) with diffractive apertures smoothly matching the overall structure of the chamber walls.

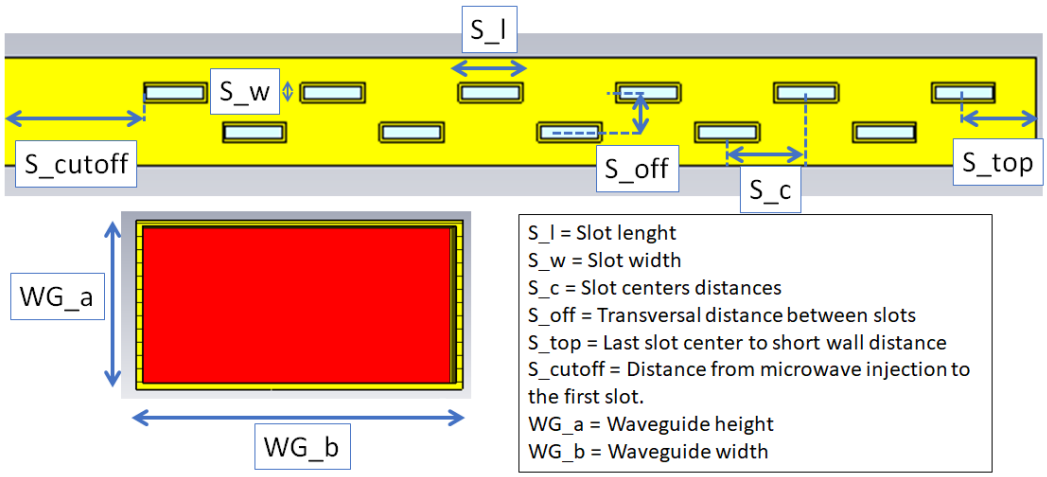

Figure 4.32: The slotted waveguide antenna with its parameters.

When designing a slotted waveguide antenna, particular attention needs to be given to its parameters (see figure 4.32), and in particular: the distance between the centre of the last slot from the closing metallic wall (S_top), the width of the slots (S_w), the length of the slots (S_l), the longitudinal distance between the centre of the slots (S_c), the transversal distance between the centre of the slots (S_off), the distance from the microwave injection to the first slot (S_cutoff) and the height and the width of the waveguide (respectively WG_a and WG_b). Another important parameter is the number of slots (n_slots) [60]: in fact, the impedance bandwidth is inversely proportional to the slot number. However, the usage of a low number of slots decreases the efficiency, so a trade-off for these parameters needs to be chosen depending on the required performances. Although

it is possible to create geometries with the programs CST MWS or COMSOL, it is difficult to use them for complex geometries: consequently, **Autodesk Inventor** was used to optimize the design of the slots, through the parametric modelling in CAD (Computer Aided Design) [61], while the CST program was still used to simulate electromagnetic fields. The optimization study started considering the antenna in free space and excited using the fundamental mode (the TE_{10} mode) of the rectangular waveguide. The operational bandwidth was considered in the range 14 GHz - 16 GHz with a central frequency about of 14.5 GHz. The study took also into account the fact that the antenna could not be straight but had to follow the geometry of the cavity. Consequently, a slotted and twisted waveguide was simulated and analyzed: figure 4.33 shows the results of the optimization of all the abovementioned parameters listed in table 4.2.

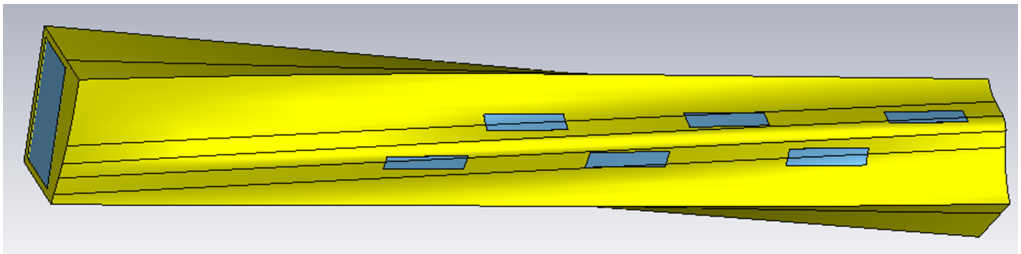

Figure 4.33: The slotted and twisted waveguide antenna at the end of the parameters optimization.

Table 4.2: The best parameters simulated of the slotted waveguide antenna

Parameters	
n_slots	6
WG_a	15.8 mm
WG_b	7.9 mm
S_l	10.2 mm
S_w	3.0 mm
S_c	11.7 mm
S_off	4.5 mm
S_top	8.8 mm
S_cutoff	40.6

Figure 4.34 shows the S11 coefficients in a wide range of frequencies: the slotted and twisted waveguide is well coupled (under -5 dB) between 14.0 GHz - 14.9 GHz.

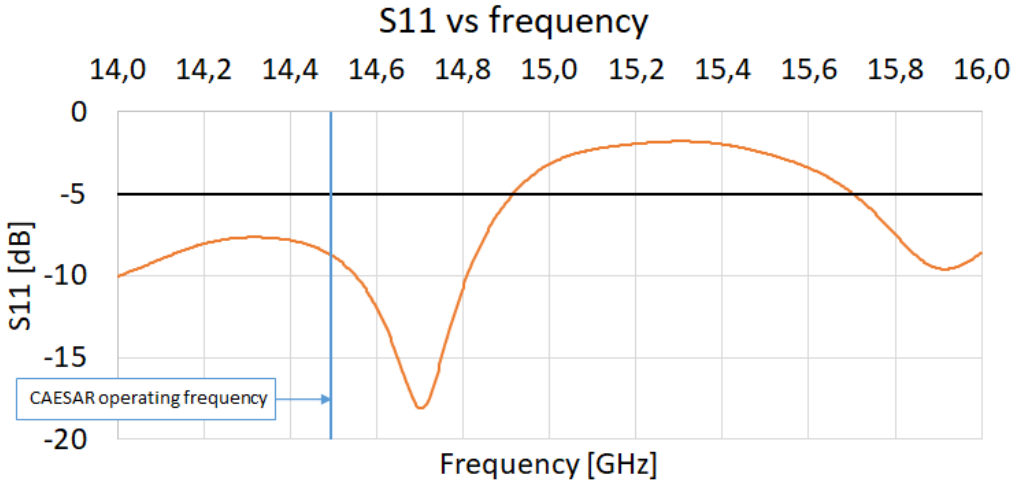

Figure 4.34: Coefficient of reflection S11, calculated in the range 14 GHz - 16 GHz, for the slotted and twisted waveguide in free space.

A parameter that determines the reliability of an antenna is the **farfield**: it describes the electromagnetic radiation distribution of an antenna. The antenna gain (G) expressed in dBi units indicates the value in decibels by which the antenna gain is greater than a hypothetical isotropic antenna (G=0 dBi), assuming that both antennas are supplied with identical power. To calculate the power gain of an isotropic antenna the following formula is used:

$$G = 10^{\frac{G(dBi)}{10}} \tag{4.1}$$

Figure 4.35 shows the farfield directivity of the antenna: the maximun value is 11.6 dBi,

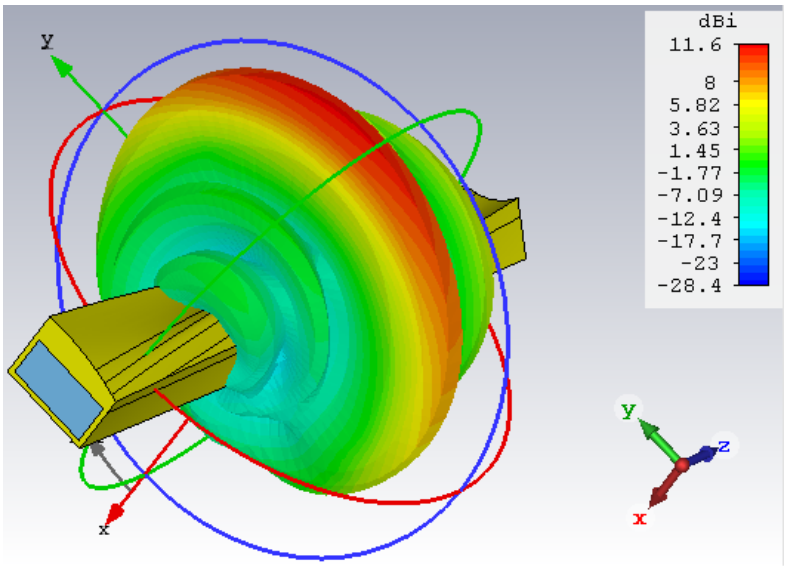

Figure 4.35: Farfield directivity in 3D form at 14.5 GHz.

thus an antenna with a gain of 14.4 times higher than an isotropic antenna. After having found the best slotted/twisted antenna characteristics, the study continued connecting it to the resonant cavity, as can be seen in figure 4.36.

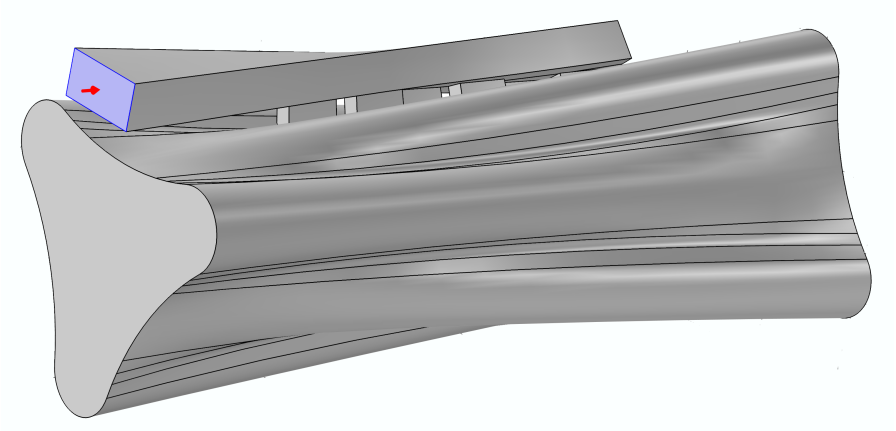

Figure 4.36: Model of the IRIS-NEW geometry with the slotted and twisted waveguide injection system.

Figure 4.37 shows the calculation of the electromagnetic fiel at 14.5 GHz: it can be seen that the electric field presents now maxima around the cavity axis.

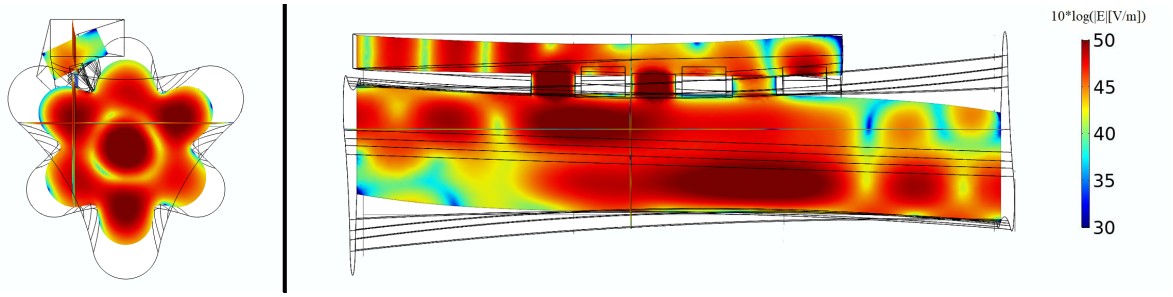

Figure 4.37: Electric field distribution (front and side views), in 10 logarithmic scales, calculated at 14.50 GHz for the IRIS-NEW chamber with the slotted and twisted waveguide injection system.

Figure 4.38 shows the S11 in the frequency range considered: we can see that there are 12 resonant modes showing a good waveguide-to-cavity coupling (S11 < -5 dB).

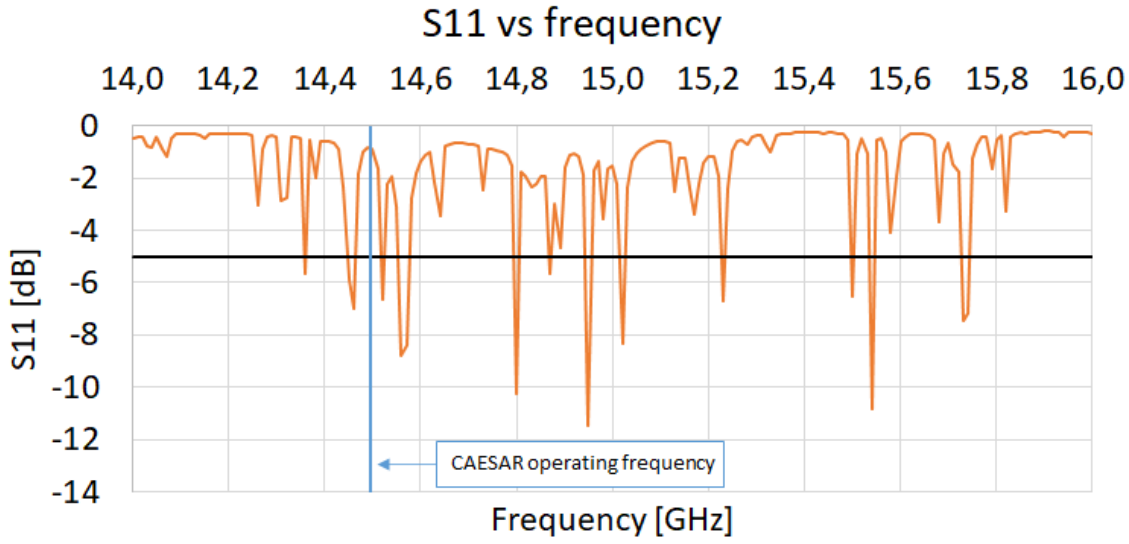

Figure 4.38: Coefficient of reflection S11, calculated in the range 14 GHz - 16 GHz, for the IRIS-NEW chamber with the slotted and twisted waveguide injection system.

The simulations continue considering the magnetized plasma and analyzing

the distribution of the electric field at 14.5 GHz. Again the simulation shows in figure 4.39 an intense E-field at the resonance points around the axis, but it is worth noticing that the values are the highest of the entire plasma chamber. By analyzing the scattering coefficient S11 a very relevant result was found: in fact, it is under -20 dB in the entire frequency range, with a minimum close to 14.5 GHz. This means that with IRIS-NEW and its unconventional microwave launching system all the frequencies are perfectly matched to the cavity. (see plot 4.40). Finally, figure 4.41 shows that the power absorbed by the plasma is at least 90 W in the 14.1 GHz - 15.0 GHz range, decreasing to 65 W at higher frequencies.

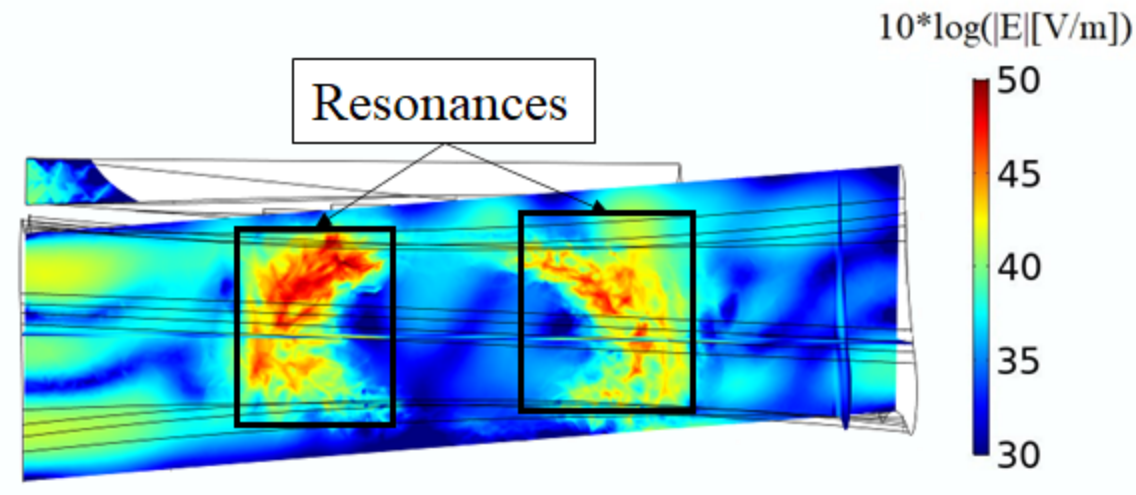

Figure 4.39: Electric field distribution, in 10 logarithmic scales, calculated at 14.50 GHz for the IRIS-NEW with the slotted and twisted waveguide injection system, including a magnetized plasma.

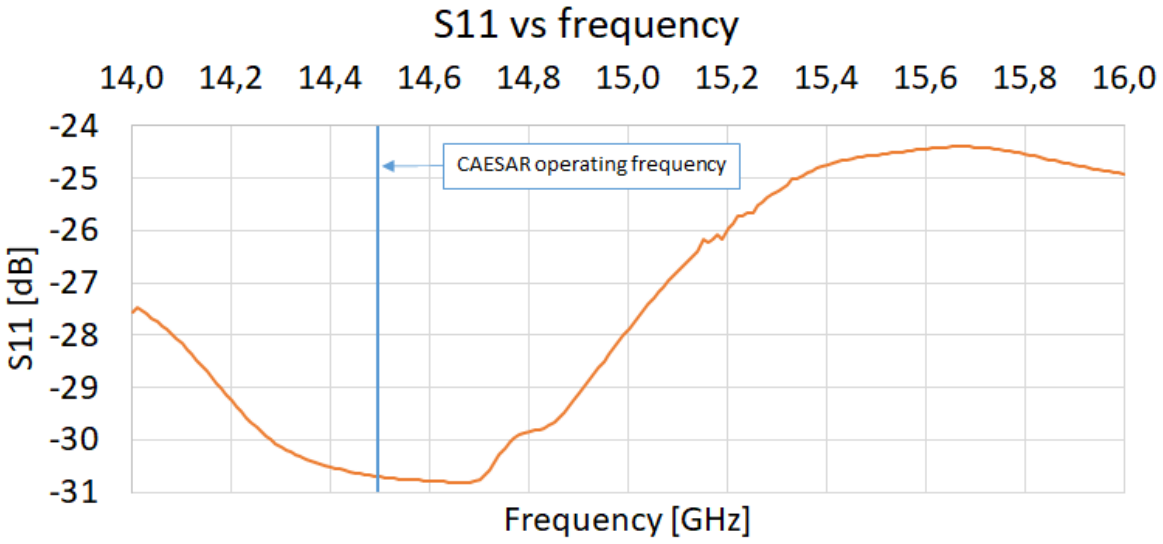

Figure 4.40: Coefficient of reflection S11, calculated in the range 14 GHz - 16 GHz, for the IRIS-NEW chamber with the slotted and twisted waveguide injection system, including a magnetized plasma.

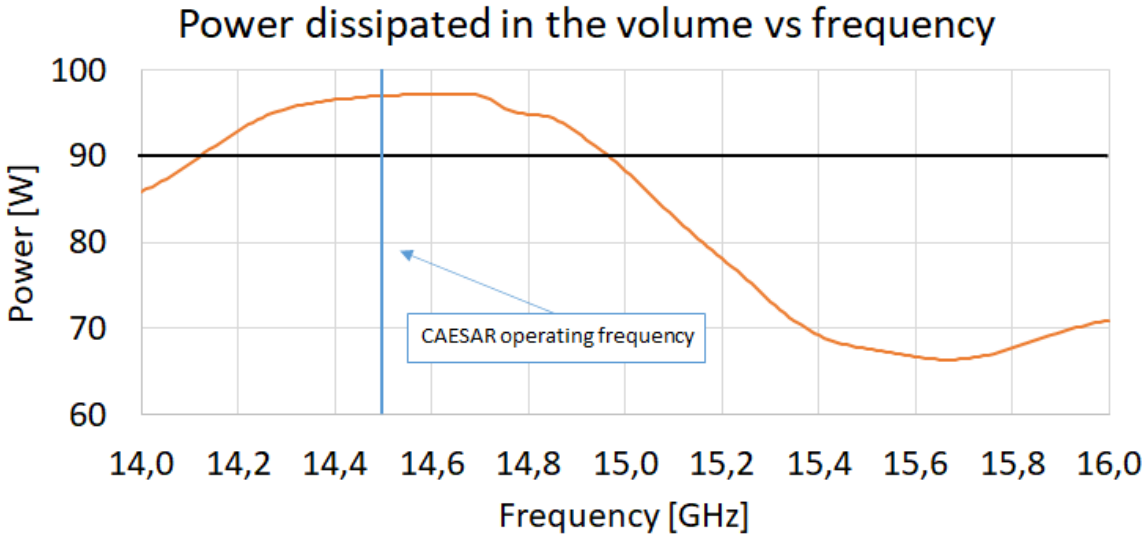

Figure 4.41: Power absorbed by the plasma in the IRIS-NEW plasma chamber with the slotted and twisted waveguide injection system.

4.5 Comparisons between the different geometries

The previous sections showed the results of the electromagnetic simulations, including a magnetized plasma, for the following configuration:

- CAESAR with axial microwave injection;
- IRIS-OLD with microwave injection tilted of 45° with respect to the longitudinal axis;
- IRIS-NEW with microwave injection tilted of 45° with respect to the longitudinal axis;
- IRIS-NEW with microwave injection with a slotted and twisted waveguide.

Those configurations will be now compared in terms of the E-field distribution at 14.5 GHz, the Scattering coefficient S11, and the power absorbed by the plasma in the range 14 GHz - 16 GHz.
The first comparison regards the electric field distribution, shown in figure 4.42, in 10 logarithmic scales at 14.5 GHz.

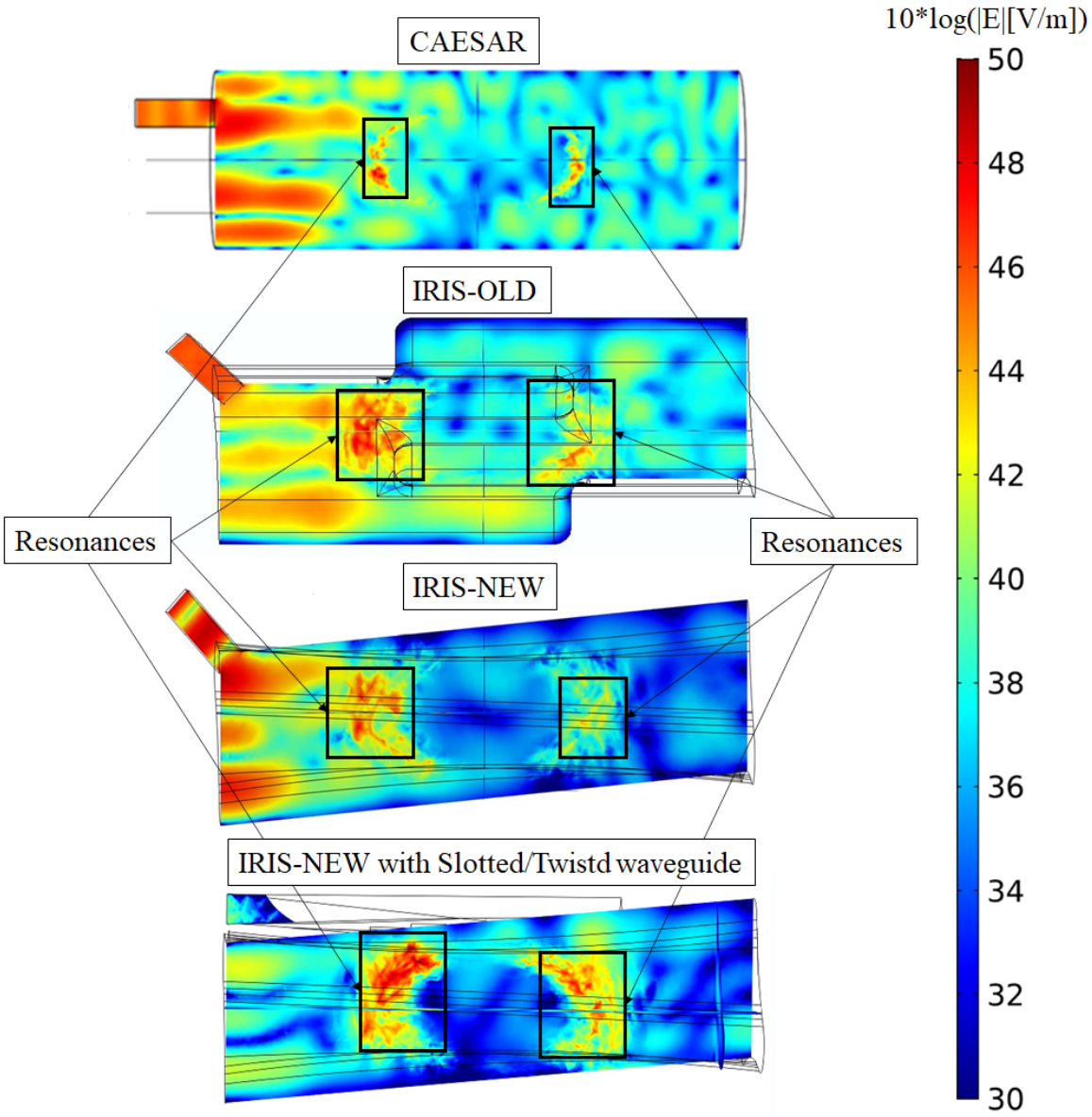

Figure 4.42: Electric field distribution, in 10 logarithmic scales, calculated through the COMSOL frequency-domain solver including a magnetized plasma. In order from top to bottom: CAESAR with the longitudinal waveguide, IRIS-OLD with the waveguide at 45° with respect to the plasma chamber axis, IRIS-NEW with the same waveguide input and IRIS-NEW with a slotted and twisted waveguide.

The regions of intensification of the electric field at the resonance are visible in all four cases, but it is evident how implementing the IRIS geometry, they become much wider, especially for IRIS-OLD and IRIS-NEW with slotted waveguides. In particular, this last configuration shows a very large absorption area at the extraction side of the plasma chamber (right), that is a higher power transfer to the plasma. If we consider that the ions extracted from an ECR come mostly from the ionization happening in this region, this is a clear indication that the implementation of IRIS-NEW with slotted waveguides could lead to a relevant improvement of the performances.
Let us now see the comparison of the reflection coefficients S11 between the waveguides and the resonant cavities, shown in figure 4.43.

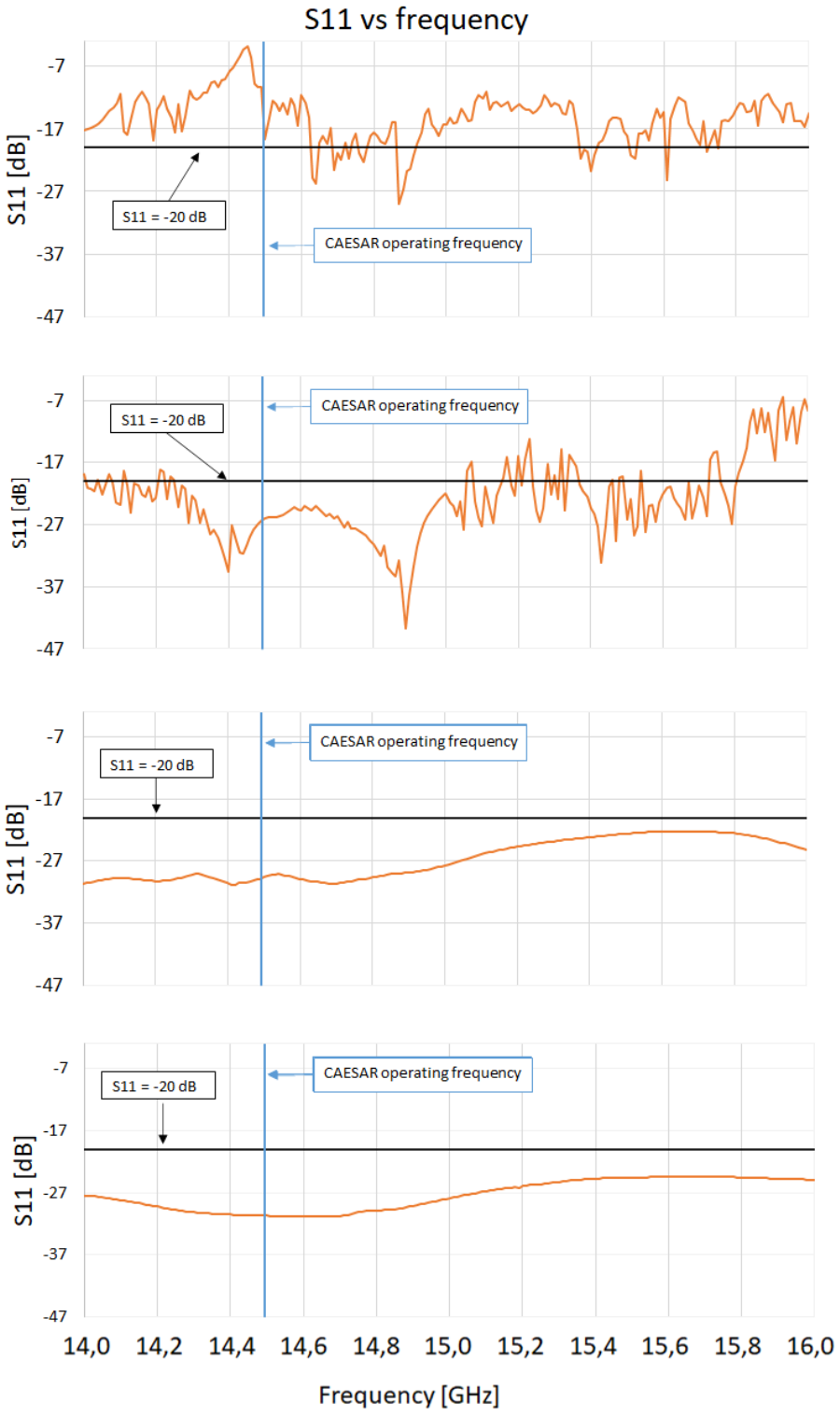

Figure 4.43: Coefficient of reflection S11 of all the four systems, in the range 14 GHz - 16 GHz, including a magnetized plasma. In order from top to bottom: CAESAR with the longitudinal waveguide, IRIS-OLD with the waveguide at 45° with respect to the plasma chamber axis, IRIS-NEW with the same waveguide input and IRIS-NEW with a slotted and twisted waveguide.

We can observe that the three versions of the new geometry improve the coupling in the entire frequency range. It is worth noticing anyway that the two versions of IRIS-NEW always show a coupling much better than -20 dB: this is a very important aspect in connection with the application of the frequency tuning because there wouldn't be any influence of the specific frequency used on the power effectively coupled to the plasma. Considering the CAESAR operating frequency, it is important to underline that at this frequency the coupling improves from -18 dB to -26 dB for IRIS-OLD and to -30 dB for the two versions of IRIS-NEW.
The last parameter to be compared is the power absorbed by the plasma, directly related to its energetic content and shown in figure 4.44. Before doing this, it is important to point out that, due to its present magnetic structure, CAESAR could not work at a frequency higher than 15 GHz, so the range considered relevant for the comparison will be 14 GHz - 15 GHz.

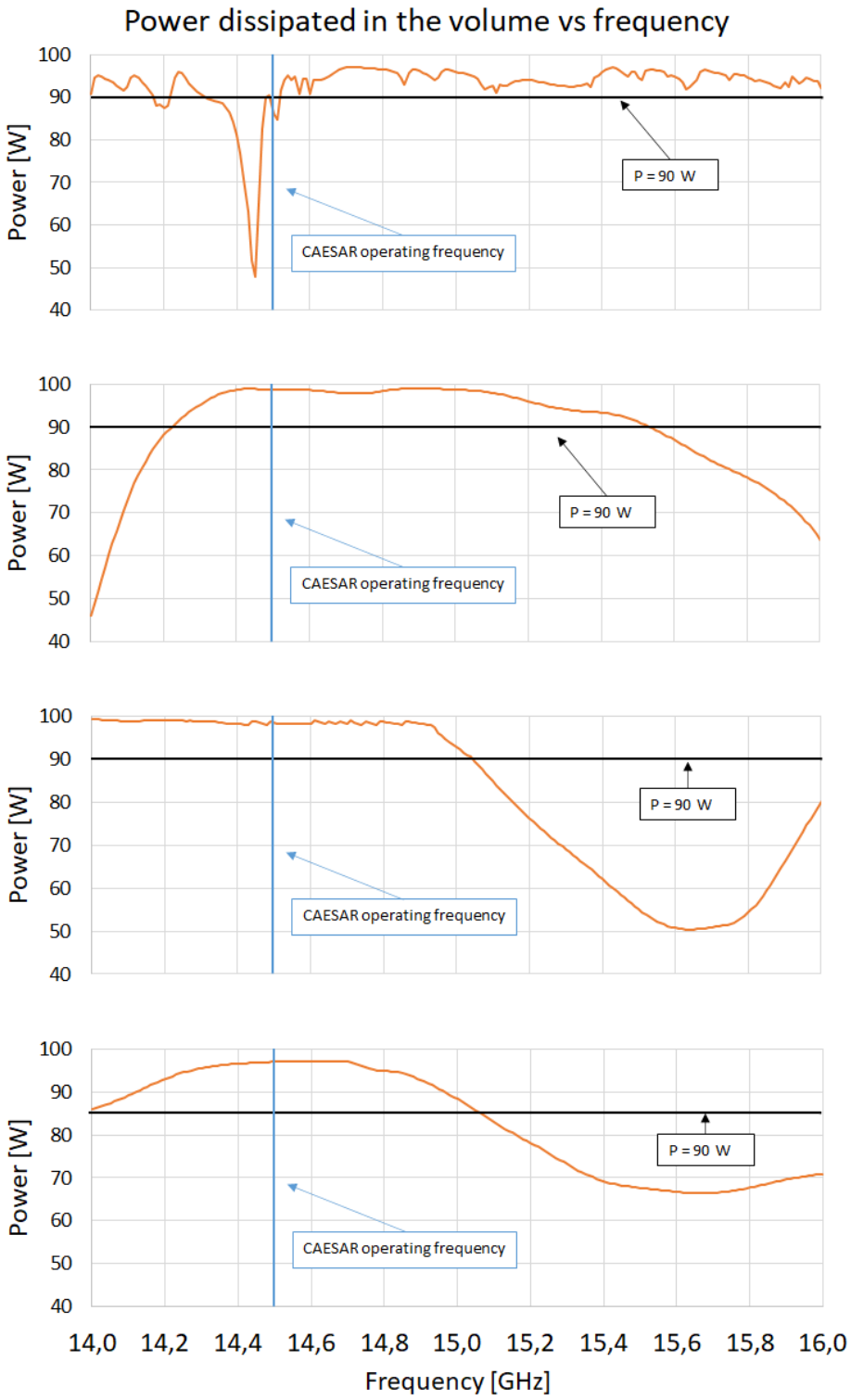

Figure 4.44: Power absorbed by the plasma in all the four systems in the range 14 GHz - 16 GHz. In order from top to bottom: CAESAR with the longitudinal waveguide, IRIS-OLD with the waveguide at 45° with respect to the plasma chamber axis, IRIS-NEW with the same waveguide input and IRIS-NEW with a slotted and twisted waveguide.

We can observe from the picture that both versions of IRIS-NEW show a higher power absorbed, compared to the classical CAESAR plasma chamber, except at the extremes of the range for the case with the slotted waveguides. More, all the proposed versions show a much higher power absorption at the typical operating frequency, indicating that their implementation will surely lead to an improvement of the performances.

Conclusions and future perspectives

This thesis described the optimization of the performances of an ECR source, brought by a possible implementation of an innovative plasma chamber geometry with an unconventional microwave launching system. Different versions of the new structure were compared with the classical cylindrical resonant cavity, with an axial microwave injection, of the CAESAR ECR ion source, carrying out electromagnetic simulations including a magnetized plasma. The structure, called IRIS, presents some key advantages concerning the classic cylindrical resonant cavity, in particular:

- the creation of electromagnetic field distributions with a predominant electric field on the axis of the chamber;
- the presence of much wider zones where the resonant absorption takes place. In particular, the one at the extraction obtained with IRIS-NEW with the slotted/twisted waveguide, that could lead to a higher ions' production, thus increasing the intensity of the extracted beam;
- the power absorbed by the plasma is higher than 90 W in the range 14.4 GHz - 15 GHz, including the operating frequency of the CAESAR source.

Furthermore, passing from the IRIS-OLD structure to the IRIS-NEW we obtain:

- a plasma chamber of easier mechanical construction;

- more space available for the surrounding magnetic system

The use of the slotted and twisted waveguide involves:

- smoother distribution of the S11 coefficient in the analysed energy range, that translates in a higher flexibility in the operation of the ion source;

- a more symmetric field and power distribution from the multiple radiating waveguide slots;

- the possibility to have more space available on the injection flange.

The importance of the results has been also demonstrated by carrying out simulations of electrons' dynamics (not object of this thesis), using the electromagnetic fields calculated for this work of the thesis. In particular, the plasma resulting from the interaction of electrons with the electromagnetic field set-up inside the conventional CAESAR plasma chamber has been compared to the one obtained with IRIS-NEW, using a numerical approach developed by the INFN ion source group [62] [63]. To underline the difference given only by the new geometry, the calculation has been done considering IRIS-NEW with an axial microwave injection. Figure 4.45 shows the comparison between the electrons' occupation maps (resembling a density distribution) obtained for CAESAR (left) and IRIS-NEW (right): it can be clearly seen how IRIS-NEW creates a much denser plasma in a smaller region around the plasma chamber axis, with the possibility to eventually increase the intensity and average charge state of the extracted beam.

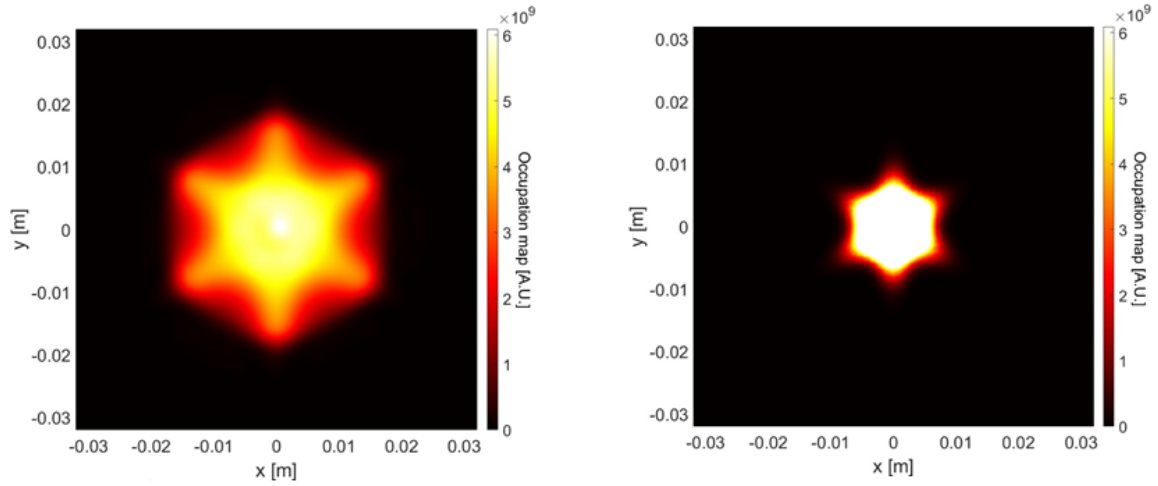

Figure 4.45: Occupation maps, resembling a density of distribution, resulting from electrons dynamics calculations carried out for the CAESAR (left) and IRIS-NEW (right) plasma chambers.

In the light of the results described above, the study can be considered concluded and the manufacturing phase has been started. Before the prototype was made, we used the mechanical cad "refinement" sequence (by Inventor) in order to obtain a sufficiently "smooth" structure to be created in Additive Manufacturing technology (3D printing in metal). The first prototype (see figure 4.46) was plastic made to verify that the printer was actually capable of drawing the geometry.

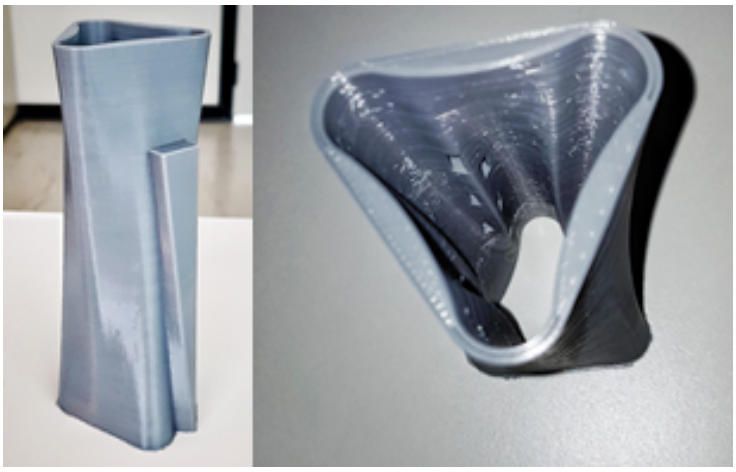

Figure 4.46: 3D print in plastic material of the resonant chamber with the slotted and twisted waveguide.

Subsequently, with the same process but with steel-base metal powders material, a classical cylinder was made (see figure 4.47), to verify that this material is effectively vacuum tight.

Figure 4.47: Vacuum test of a classical cylinder made in steel-base metal powders material by 3D print.

The last prototype that was made is a slotted and twisted waveguide (shown in figure 4.48): its characterization is presently on-going.

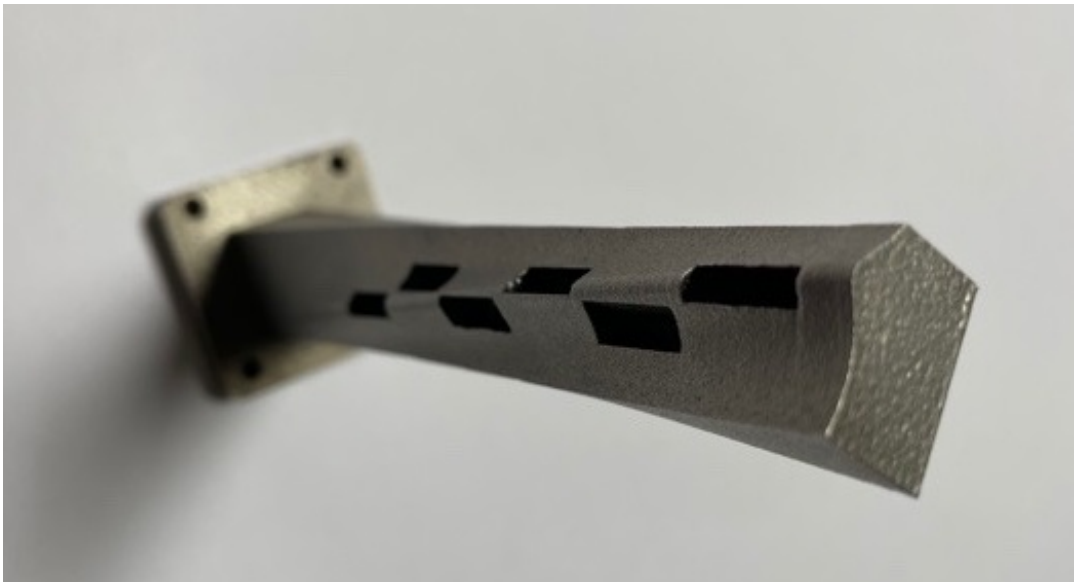

Figure 4.48: Slotted and twisted waveguide in steel-base metal powders material.

At the end of the antenna characterization tests, the first prototype of the IRIS-NEW cavity system will be built with the incorporated slotted and twisted antenna. To validate the changes proposed in this thesis, we will proceed as follows:

1. **Bench tests**
   The prototype will be connected to a network analyzer to measure the coefficient of reflection S11, in the range 14 GHz - 16 GHz, to compare it with the one measured with the classic cylindrical cavity. This should confirm the improvement of the coupling between the waveguide and the cavity brought in by the new geometry, as foreseen by the simulations;

2. **Online tests**
   Considering that the aim of the work described in this thesis is to propose a new geometry to improve the ion source performances, the first step will be the acquisition of reference values on high charge states production of both light (O^{7+}) and heavy (Xe^{28+}) ions with the CAESAR source employing the classical cylindrical cavity. The same tests will be then repeated using the new plasma chamber. In order to perform an accurate comparison of the results, the microwave circuit used will include a double directional coupler with two power probes, to measure both the forward and reflected power and keep the net power delivered to the plasma constant for both the experimental run. This will allow us to identify the direct influence of the new geometry on any possible variation of the ion source performances.

Bibliography

[1] R. Geller, *Electron cyclotron resonance ion sources and ECR plasmas*, Bristol: IOP, 1996.

[2] Z. Q. Xie and C. M. Lyneis, *Two-frequency plasma heating in a high charge state electron cyclotron resonance ion source*, Rev. Sci. Instrum., 66, 4218, 1995.

[3] A. Kitagawa, T. Fujita, M. Muramatsu, S. Biri, R.Racz, Y. Kato, K. Yano, N. Sasaki, and W. Takasugi, *TWO-FREQUENCY HEATING TECHNIQUE FOR STABLE ECR PLASMA*, Proc. 20th Int. Workshop on ECR Ion Sources (ECRIS'12), Sydney, Australia, 2012.

[4] S Biri, A Kitagawa, M Muramatsu, A G Drentje, R Rácz, K Yano, Y Kato, N Sasaki, and W Takasugi, *Two-frequency heating technique at the 18 GHz electron cyclotron resonance ion source of the National Institute of Radiological Sciences*, Rev. Sci. Instrum., 2014.

[5] R. Racz et al., *Effect of the two-close-frequency heating to the extracted ion beam and to the X-ray flux emitted by the ECR plasma*, JINST, 13, C12012, 2018.

[6] E Naselli, D Mascali, M Mazzaglia, S Biri, R Rácz, J Pálinkás, Z Perduk, A Galatá, G Castro, L Celona, S Gammino, and G Torrisi *Impact of two-close-*

frequency heating on ECR ion source plasma radio emission and stability, Plasma Sources Science and Technology, Volume 28, Number 8, 2019.

[7] L. Celona et al., *Observations of the frequency tuning effect in the 14 GHz CAPRICE ion source*, Rev. Sci. Instrum., 79, 023305, 2008.

[8] D. Mascali, S. Gammino, L. Celona, G. Ciavola, L. Neri, R. Miracoli, N. Gambino, G. Castro, and F. Maimone *SOME CONSIDERATIONS ABOUT FREQUENCY TUNING EFFECT IN ECRIS PLASMAS*, ECRIS Workshop 2010, Grenoble, 2010.

[9] G. Rodrigues, Kedar Mal, Narender Kumar, R. Baskaran, P. S. Lakshmy, Y. Mathur, P. Kumar, D. Kanjilal, and A. Roy, *Effect of frequency tuning on bremsstrahlung spectra, beam intensity, and shape in the 10 GHz NANOGAN electron cyclotron resonance ion sourcea*, REVIEW OF SCIENTIFIC INSTRUMENTS, 2014

[10] S. Gammino and G. Ciavola, *The role of microwave frequency on the high charge states build-up in the ECR ion sources*, Plasma Source Sci. Technol., 1996.

[11] L. Celona, G. Castro, S. Gammino, D. Mascali, L. Neri, G. Torrisi, G. Ciavola, A. Galatà, *ECR ion source developments at INFN-LNS*, 21st International 110 Workshop on ECR Ion Sources, Niznhy Novgorod, Russia, 2014.

[12] S. Gammino and G. Ciavola, *The contribution of the INFN-LNS to the development of electron cyclotron resonance ion sources*, Rev. Sci. Instrum. 71, 631, 2000.

[13] D. Mascali, M. Busso, A. Mengoni, S. Amaducci, G. Castro, L. Celona, G. Cosentino, S. Cristallo, P. Finocchiaro, A. Galatà, S. Gammino, C. Massimi, M. Maggiore, G.S. Mauro, M. Mazzaglia, E. Naselli, F. Odorici, S. Palmerini, D. Santonocito and G. Torrisi, *The PANDORA project: an experimental setup for measuring in-plasma β-decays of astrophysical interest*, EPJ Web of Conferences, 2020.

[14] T. Marchi, G. Prete, F. Gramegna, A. Andrighetto, P. Antonini, M. Ballan, M. Bellato, L. Bellan, D. Benini, G. Bisoffi, J. Bermudez, G. Benzoni, D. Bortolato, F. Borgna, A. Calore, S. Canella, S. Carturan, N. Ciatara, M. Cinausero, D. Zafiropoulos, *The SPES facility at Legnaro National Laboratories*, Journal of Physics: Conference Series, 2020.

[15] D.D. Clayton, *Principles of Stellar Evolution and Nucleosynthesis*, University of Chicago Press, 1984

[16] Bosch, F. et al., Phys. Rev. Lett. 77, 5190, 1996.

[17] Jung, M. et al., Phys. Rev. Lett. 69 2164, 1992.

[18] G. Prete, A. Andrighetto, M. Manzolaro, S. Corradetti, D. Scarpa, M. Rossignoli, A. Monetti, M. Lollo, M. Calderolla, J. Vasquez, D. Zafiropoulos, L. Sarchiapone, D. Benini, P. Favaron, M. Rigato, R. Pegoraro, D. Maniero, L. Calabretta, M. Comunian, M. Maggiore, A. Lombardi, L. Piazza, A.M. Porcellato, C. Roncolato, G. Bisoffi, A. Pisent, A. Galatà, M. Giacchini, G. Bassato, S. Canella, F. Gramegna, J. Valiente, J. Bermudez, P.F. Mastinu, J.Esposito, J. Wyss, S. Zanella, *The SPES project at the INFN Laboratori Nazionali di Legnaro*, EPJ Web Conferences 66, 11030, 2014.

[19] M. Manzolaro, F. D'Agostini, A. Monetti, and A. Andrighetto, *The SPES surface ionization source*, Review of Scientific Instruments 88, 093302, 2017.

[20] M. Manzolaro, G. Meneghetti, A. Andrighetto, and G. Vivian, *Electrical-thermal-structural finite element simulation and experimental study of a plasma ion source for the production of radioactive ion beams*, Review of Scientific Instruments 87, 033303, 2016.

[21] A. Pisent, L. Bellan, M. Comunian, B. Chalykh, A. Russo, and L. Calabretta, *SPES BEAM DYNAMICS*, Proceedings of HB2014, East-Lansing, MI, USA, 2014.

[22] G. Fortuna et al., *THE ALPI PROJECT AT THE LABORATORYNAZIONALI DI LEGNARO*, Nucl. Instr. and Meth., A287, pp.253-256, 1990.

[23] A. Galatà, G. Patti, C. Roncolato, J. Angot, and T. Lamy, *The new ECR charge breeder for the Selective Production of Exotic Species project at INFN—Laboratori Nazionali di Legnaro*, Review of Scientific Instruments 87, 02B503, 2016.

[24] A. Galatà, C. Roncolato, P. Francescon, G. Bisoffi, L. Bellan, M. Bellato, J. Bermudez, D. Bortolato, M. Comunian, A. Conte, M. De Lazzari, F. Gelain, D. Marcato, M. Miglioranza, M.F. Moisio, E. Munaron, S. Pavinato, D. Pedretti, A. Pisent, M. Rossignoli, M. Roetta, G. Savarese and V. Andreev, *Progresses in the installation of the SPES-Charge Breeder beam line*, JINST 13 C12009, 2018.

[25] A. Galatà, C. Roncolato, G. Bisoffi, P. Francescon, L. Bellan, J. Bermudez, D. Bortolato, M. Comunian, A. Conte, M. De Lazzari, F. Gelain, D. Marcato, M. Miglioranza, M. F. Moisio, E. Munaron, S. Pavinato, D. Pedretti, A. Pisent, M. Rossignoli, M. Roetta, G. Savarese, M. Bellato, J. Angot, D. Bondoux, T. Thuillier, and V. Andreev, *Towards the first beams from the ADIGE injector for the SPES Project*, J. Phys.: Conf. Ser. 1350 012090, 2019.

[26] A. Galatà *Physics and Technology of the SPES Charge Breeder*, Ferrara University, 2015.

[27] J. Angot, T. Lamy, M. M. Jeanne, P. Sortais, and T. Thuillier, in *Proceedings of the 20th International Workshop on Electron Cyclotron Resonance Ion Sources (ECRIS-2012)*, Sydney, Australia, 2012.

[28] M. Maggiore, D. Campo, P. Antonini, A. Lombardi, M. Manzolaro, A. Andrighetto, A. Monetti, D. Scarpa, J. Esposito, and L. Silvestrin, *SPES: A new cyclotron-based facility for research and applications with high-intensity beams*, Modern Physics Letters A, Vol. 32, No. 17, 1740010, 2017.

[29] http://www.bestcyclotron.com/about.html

[30] G. Prete, A. Andrighetto, M. Manzolaro, S. Corradetti, D. Scarpa, M. Rossignoli, A. Monetti, M. Lollo, M. Calderolla, J. Vasquez, D. Zafiropoulos1, L. Sarchiapone, D. Benini, P. Favaron, M. Rigato, R. Pegoraro,

D. Maniero, L. Calabretta, M. Comunian, M. Maggiore, A. Lombardi, L. Piazza, A.M. Porcellato, C. Roncolato, G. Bisoffi, A. Pisent, A. Galatà, M. Giacchini, G. Bassato, S. Canella, F. Gramegna, J. Valiente, J. Bermudez, P.F. Mastinu, J. Esposito, J. Wyss, A. Russo, and S. Zanella, *The SPES radioactive ion beam project of INFN*, Journal of Physics Conference Series, 2014.

[31] G. Pupillo, P. Antonini, M. Calderolla, A. Calore, D. Bettoni, A. Boschi, S. Cisternino, A. Duatti, F. Evangelisti, P. Favaron, G. Fiorentini, F. Gramegna, G. Keppel, M. Maggiore, P. Martini, L. Mou, M. Pasquali, L. Pranovi, C. R. Alvarez, L. Sarchiapone, G. Sciacca, H. Skliarova, and J. Esposito, *The Laramed project at LNL:* ^{67}Cu *and* ^{47}Sc *production for theranostic applications*, AIP Conference Proceedings 2295, 020001, 2020.

[32] J. Esposito, D. Bettoni, A. Boschi, M. Calderolla, S. Cisternino, G. Fiorentini, G. Keppel, P. Martini, M. Maggiore, L. Mou, M. Pasquali, L. Pranovi, G. Pupillo, C. R. Alvarez, L. Sarchiapone, G. Sciacca, H. Skliarova, . Favaron, A. Lombardi, P. Antonini, and A. Duatti, *LARAMED: A Laboratory for Radioisotopes of Medical Interest*, Molecules, 24(1), 20, 2019.

[33] A. Andrighetto, M. Tosato, M. Ballan, S. Corradetti, F. Borgna, V. Di Marco, G. Marzaro, and N. Realdon *Journal of Radioanalytical and Nuclear Chemistry* volume 322, pages 73–77, 2019.

[34] M. Ballan, M. Tosato, M. Verona, M. Caeran, F. Borgna, E. Vettorato, S. Corradetti, L. Zangrando, M. Sgaravatto, M. Verlato, M. Asti, G. Marzaro, F. Mastrotto, V. Di Marco, D. Maniglio, A. Bisio, A. Motta, A. Quaranta, A. Z. P. Pastore, N. Realdon, and A. Andrighetto, *Preliminary evaluation of the production of non-carrier added* ^{111}Ag *as core of a therapeutic radiopharmaceutical in the framework of ISOLPHARM Ag experiment*, Applied Radiation and Isotopes, Volume 164, 109258, 2020.

[35] D. Leitner, C. M. Lyneis, *High intensity high charge states ECR ion sources*, Proc of PAC, Knoxville, Tennessee, 2005.

[36] J. L. Shohet *Plasma Science and Engineering*, Encyclopedia of Physical Science and Technology Reference Work, Third Edition, 2001.

[37] P. Gibbon *Introduction to Plasma Physics*, CERN, Proceedings of the 2014 CAS-CERN Accelerator School: Plasma Wake Acceleration, 2016.

[38] F. F. Chen. *Introduction to plasma physics and controlled fusion*, Vol. 1. Springer, 1984.

[39] M. S. Ioffe, *Mirror Traps*, Plasma Physics, 1965.

[40] L. Spitzer, R. Harm, *Transport Phenomena in a Completely Ionized Gas*, Phys. Rev. 89, 977-81, 1953.

[41] W. Lotz, *Electron-Impact Ionization Cross-Sections and Ionization Rate Coefficients for Atoms and Ions*, Astrophysical Journal Supplement, vol. 14, p.207, 1967.

[42] *An empirical formula for the electron-impact ionization cross-section*, Zeitschrift fùr Physik, Volume 206, Issue 2, pp.205-211, 1967.

[43] K. S. Golovanivsky, *Instruments and experimental techniques*, vol. 28, no. 5, part 1, pag 989, New York: Plenum, 1986.

[44] A. Muller, and E. Salzborn, *Scaling of cross sections for multiple electron transfer to highly charged ions colliding with atoms and molecules*, Phys. Lett. 62 A 391, 1977.

[45] S. Barbarino. *Appunti di campi elettromagnetici*, 2006.

[46] F. Jeager, A. J. Lichtenberg, and M. A. Lieberman, *Theory of electron cyclotron resonance heating I: Short time and adiabatic effects*, Plasma Phys., vol. 14, no. 12, pp. 1073-1100, 1971.

[47] F. Jeager, A. J. Lichtenberg, and M. A. Lieberman, *Theory of electron cyclotron resonance heating II: Long time and stochastic effects*, Plasma Phys., vol. 15, no. 2, pp. 125-150, 1973.

[48] J. L. Delcroix, *Introduction to the Theory of Ionized Gases*, Interscience, 1960.

[49] E. Canobbio, *Gyroresonant particle acceleration in a non-uniform magnetostatic field*, Nucl. Fusion, 1969.

[50] https://www.pantechnik.com/ecr-ion-sources/

[51] G. Ciavola, S. Gammino, L. Celona, F. Maimone, A. Galatà, M. Pullia, R. Monferrato, C. Bieth, W. Bougy, G. Gaubert, O. Tasset, A.C.C. Villari, *Commissioning of the ECR ion sources at CNAO facility*, Proceedings of EPAC08, Genoa, Italy.

[52] Z.Q. Xie and C.M. Lyneis, *Two-Frequency Plasma Heating in a High Charge State ECR Ion Source*, Review of Scientific Instruments, 1994.

[53] A. Galatà, T. Kulevoy, M. Sattin, F. Scarpa, and A. Facco, *First beams from the new electron cyclotron resonance source LEGIS (LEGnaro ecrIS) at INFN-LNL*, Rev. Sci. Instrum 81, 02A315, 2010.

[54] G. Franceschetti, *Campi elettromagnetici*, Bollati Boringhieri, 1983

[55] D. M. Pozar, *Microwave Engineering*, J. Wiley and sons, Canada, 1998.

[56] P. Bernardi, *Lezioni di microonde*, 2006

[57] https://www.3ds.com/it/prodotti-e-servizi/simulia/prodotti/cst-studio-suiter/

[58] https://www.comsol.it/

[59] https://www.mathworks.com/products/matlab.html

[60] S. S. Sekretarov and D. M. Vavriv, *A wideband slotted waveguide antenna array for sar systems*,In Electromagnetics Research M, vol. 11, pp. 165–176, 2010.

[61] https://www.autodesk.eu/products/inventor

[62] A. Galatà, D. Mascali, C.S. Gallo and G. Torrisi, *Self-consistent modeling of beam-plasma interaction in the charge breeding optimization process*, Review of Scientific Instruments 91, 013506, 2020.

[63] B. Mishra, A. Pidatella, S. Biri, A. Galatà, E. Naselli, R. Ràcz, G. Torrisi, and D. Mascali *A novel numerical tool to study electron energy distribution functions of spatially anisotropic and non-homogeneous ECR plasmas*, Physics of Plasmas 28, 102509, 2021.